國立臺灣大學工學院材料科學及工程學系

博士論文

Department of Materials Science and Engineering
College of Engineering
National Taiwan University
Doctoral Dissertation

以固相法製備介電 $Ba_5Nb_4O_{15}$ 及其燒結行為與微波電性

Sintering Behavior and Microwave Property of $Ba_5Nb_4O_{15}$ Dielectric Material and its Preparation

曹 中 亞

Chung-Ya Tsao

指導教授：段維新 博士

Advisor: Wei-Hsing Tuan, Ph.D.

中華民國 106 年 7 月

July, 2017

doi:10.6342/NTU201702760

國立臺灣大學博士學位論文
口試委員會審定書

論文中文題目：以固相法製備介電 $Ba_5Nb_4O_{15}$ 及其燒結行為與微波電性

論文英文題目：Sintering Behavior and Microwave Property of $Ba_5Nb_4O_{15}$ Dielectric Material and its Preparation

本論文係**曹中亞**君（D97527009）在國立臺灣大學材料科學與工程學系、所完成之博士學位論文，於民國 106 年 07 月 27 日承下列考試委員審查通過及口試及格，特此證明

口試委員：段維新（指導教授）

黃坤祥

周振嘉

謝宗霖

郭錦龍

馮奎智

系主任、所長林 新 智（簽名）

doi:10.6342/NTU201702760

誌 謝

走進二號館階梯教室準備論文口試的那一刻，腦海中喚起曾經遊藝在這熟悉校園的回憶，在即將畢業準備下一個人生起點時，心情是複雜不定的。然而一路走來經過時間淬煉，27 年後再次踏出校園，我才深刻體會到格物窮理的意義，要達到求知若渴 虛心若愚境界，必須鞭策自己真正做到堅持不懈和永不放棄。

首先要感謝 段維新教授給我明確的指引方向，指導我如何對實驗中所觀察的現象進行有系統的分析與闡述，最終將這些紮實的學術訓練由完成論文寫作來呈現。同時要感謝謝宗霖教授與郭錦龍教授在初次提交論文時提出相當多寶貴意見，使論文內容更加完備。感謝黃坤祥教授與周振嘉教授專業的指正對未來持續的研究方向有更多發揮空間。同樣地要感謝鼓勵我不要放棄的老長官 程凌天總經理，因為在職場工作與求學往往是兩條平行線，沒有獲得支持與鼓勵通常是無法兼顧的。

當然最要感謝在實驗工作上一直協助我的老同事黃曲陵、葉郁蓁女士以及事業部夥伴們，有他們的幫忙論文內容才能充實完整，也讓努力的痕跡成為論文裡共同記憶。還要感謝馮奎智博士在共同執行主導性產品開發計劃的卓越貢獻，使論文研究方向得以充分展現。謝謝系辦林由莉女士不時的叮嚀與課務協助。另外也要感謝明志科大江美貞小姐多次協助 TEM 分析，讓論文中探討晶體結構時有清楚的佐證數據。台大陶瓷複合材料實驗室的學弟妹們，因為你們的安排使我能在 XPS/FIB/EBSD/XRD 極圖分析等重要實驗順利完成，也謝謝所有協助樣品分析的工作者。

最後要感謝我摯愛的家人，在漫長又間斷的研修過程，許多煩瑣阻礙了學習動力，茉里無怨的付出全心照顧家庭，在徬徨時陪伴我一起渡過低潮，在面臨抉擇時支持我去勇敢承擔。看著致蓁與原輔走入大學生活，已經是知天命之年的我內心只有感恩，我擁有的皆是主所賜，也將一切榮耀歸於主。 謹以此論文獻給天上的 父母。

doi:10.6342/NTU201702760

摘 要

固相反應製程技術是目前製造介電陶瓷材料的生產方法之一。在眾多微波介電質材料中,$Ba_5Nb_4O_{15}$ 具有高電介質以及低損失特性,可用於低溫共燒陶瓷技術(Low Temperature Cofiring Ceramic Technology)的選擇材料之一。本研究將分三種方向探討 $Ba_5Nb_4O_{15}$ 材料與固相反應製程之關聯及影響。

第一階段是探討陽離子空缺型 $Ba_5Nb_4O_{15}$ 材料的高溫燒結行為,在無施加壓力的條件下,最高燒結密度僅能達到理論值的 93%,當燒結溫度高於 1250°C,密度將隨燒結溫度提升而逐漸下降,此去燒結現象來自於燒結溫度高於 1250°C 晶粒開始異常成長以及溫度高於 1350°C 後,鈮離子還原反應所造成。雖然微波特性的介質常數下降,但是品質因子卻可以提高到 40,000 以上,其原因與鈣鈦礦結構中陽離子晶格有序化程度有強烈的關聯性。

第二階段是探討 $Ba_5Nb_4O_{15}$ 粉末在研磨過程中的機械化學行為。在無球磨粉碎條件下,品質因子可以提高至 40,000 以上,但是研磨後鋇離子溶出晶格體,產生的 $BaCO_3$ 結晶物質析出於水系漿料中,燒結後密度以及品質因子明顯下降。由於微觀結構的燒結晶粒成長具有優選方向,利用 X-ray 繞射極圖分析以及 EBSD 方法確認(0 0 5)為優選結晶面,與前次實驗相同,米勒指數(0 1 13)平面的有序化程度與品質因子有強烈的關聯性。

最後階段則是研究少量添加物質 CuO 以及 B_2O_3 的低溫助燒結行為,大幅度地降低燒結溫度達 400°C 以上,可以將此組成用於與銀共燒結的積層陶瓷結構中,並且無銀擴散反應的現象,由微觀結構分析確認經過研磨製程也會產生 $BaCO_3$ 析出物質。

關鍵詞: 微波 ; $Ba_5Nb_4O_{15}$; 層狀鈣鈦礦相 ; 異方性晶粒成長 ; 晶體結構 ; 化學機械性 ; 優選方向 ; 液相燒結

doi:10.6342/NTU201702760

Abstract

Solid state reaction technique is one of the methods to prepare dielectric ceramic materials. A potential microwave ceramic, $Ba_5Nb_4O_{15}$, is the potential candidate of LTCC material. Its microwave dielectric exhibits high permittivity and low loss characteristics. The present study investigates three aspects of this microwave ceramic.

The sintering behavior of the cation-deficient perovskite, $Ba_5Nb_4O_{15}$, is investigated in the first part. The highest density can be achieved through pressureless sintering is only 93%. The low sintered density is related to a density decrease, de-sintering, at a sintering temperature above 1250°C. Such de-sintering is contributed by the formation of abnormal grains (>1250°C) and the reduction of niobium ions (>1350°C). Though the permittivity of sintered $Ba_5Nb_4O_{15}$ is lower after sintering at a temperature higher than 1400°C, its quality factor is higher than 40,000. The increase in quality factor shows a strong dependence on the cation ordering in the perovskite structure.

The mechanochemical behavior during the milling of $Ba_5Nb_4O_{15}$ powder is investigated in the second part. Maximum quality factor >40,000 can be achieved without ball milling. After milling, the precipitated $BaCO_3$ from water base slurry reduces the sintered density, degrades the quality factor. Such precipitate is formed due to the leaching of barium ion from lattice structure. Through the pole figure analysis, the $Ba_5Nb_4O_{15}$ (0 0 5) plane is the preferred oriented growth plane. The ordering of plane (0 1 13) shows a strong influence on the quality factor of $Ba_5Nb_4O_{15}$ after mechanical treatment.

The last part focus on the effect of a small amount of additives CuO and B_2O_3 on the sintering behavior. The sintering temperature is reduced by almost 400°C. The cofiring with silver metal to form multilayered structure is then possible. No silver migration is observed when cofire with silver metal. The microstructure analysis confirms the $BaCO_3$ is also formed as resulted from the use of milling process.

Keywords: microwave; $Ba_5Nb_4O_{15}$; layered perovskite; anisotropic grain growth; structure; mechanochemical; preferred orientation; liquid phase sintering

doi:10.6342/NTU201702760

Content

口試委員審定書 ……i

誌謝…….…….... ii

中文摘要……iii

Abstract……iv

List of Figures……viii

List of Tables……xiii

Chapter 1: Introduction…… 1

Chapter 2: Literary survey……2

2.1 $Ba_5Nb_4O_{15}$ crystal structure……..3

2.2 Homogenization of chemical composition with synthesis technology……6

2.3 Densification by liquid phase sintering……9

2.4 Polarization of $Ba_5Nb_4O_{15}$ dielectric properties under microwave frequency…….14

2.4.1 Hakki-Coleman method……18

2.4.2 Cavity resonate method……20

2.4.3 Mathematical calculation of permittivity and quality factor…….....23

2.5 Ordering Structure of high quality factor…….26

Chapter 3: Sintering Behavior and Microwave Properties of $Ba_5Nb_4O_{15}$.....27

3.1 Introduction……27

3.2 Experimental method……..30

3.2.1 Raw material preparation……31

3.2.2 Experimental flow chart and procedure……..… 32

3.3 Result……..… 35

3.3.1 Weight loss characteristic…….……35

3.3.2 Sintering density degradation……..… 39

doi:10.6342/NTU201702760

3.3.3 Microstructure and X-ray diffraction…… 41

3.3.4 XPS analysis……52

3.3.5 Microwave characteristic: permittivity and quality factor……55

3.4 Discussion……57

3.4.1 De-sintering phenomena……57

3.4.2 Reduction of $Ba_5Nb_4O_{15}$……59

3.4.3 Sintering density vs. microwave characteristic……..62

3.4.4 Ordering of cation and quality factor……63

3.5 Conclusion……67

Chapter 4: Mechanochemical Property of $Ba_5Nb_4O_{15}$……68

4.1 Introduction……68

4.2 Experimental method……69

4.2.1 Raw material preparation……...69

4.2.2 Experimental flow chart and procedure…… …70

4.3 Result……..73

4.3.1 Milling ability of $Ba_5Nb_4O_{15}$ powder……73

4.3.2 Leaching phenomena……77

4.3.3 Interaction with water of milled $Ba_5Nb_4O_{15}$ ……79

4.3.4 Anisotropic grain growth……..…82

4.3.5 Weight loss of sintered $Ba_5Nb_4O_{14}$……..86

4.3.6 Microwave characteristic……87

4.4 Discussion……..91

4.4.1 Barium dissociation from lattice site……91

doi:10.6342/NTU201702760

4.4.2 Microstructure vs. Composition……..93

4.4.3 Preferred orientation plane by XRD pole figure identification……96

4.4.4 TEM lattice plane identification……..99

4.4.5 Preferred orientation plane by EBSD identification……..106

4.4.6 Microwave characteristic of milled $Ba_5Nb_4O_{15}$……108

4.5 Conclusion……..110

Chapter 5: Liquid Phase Sintering of $Ba_5Nb_4O_{15}$……111

5.1 Introduction……..111

5.2 Experimental method……113

5.2.1 Raw material preparation……113

5.2.2 Experimental flow chart and procedure……...113

5.3 Result and Discussion……...116

5.3.1 CuO and B_2O_3 sintering additives……..116

5.3.2 Influence of milling process…….....……...118

5.3.3 Co-firing with silver metal and microstructure……..122

5.3.4 Electrical properties of low firing $Ba_5Nb_4O_{15}$……129

5.4 Conclusion……131

Chapter 6: Conclusion……132

Chapter 7: Future Work……134

Appendix……..135

Reference……..136

doi:10.6342/NTU201702760

List of Figures

Fig. 2-1 Crystal Structure of $Ba_5Nb_4O_{15}$ ……...5

Fig. 2-2 Phase Diagram of BaO-Nb_2O_5……..8

Fig. 2-3 Illustration of various types of sintering routes…….10

Fig. 2-4 (a) variation of particle growth rate for diffusion-controlled growth……....12

Fig. 2-4 (b) variation of particle growth rate for reaction-controlled growth…….12

Fig. 2-5 Models of polarization……..15

Fig. 2-6 Microwave characteristics measurement methods……17

Fig. 2-7 (a) Hakki-Coleman resonance technique……..19

Fig. 2-7 (b) Cylindrical samples for permittivity and quality factor measurement ……..19

Fig. 2-8 (a) Cylindrical cavity $TE_{01\delta}$ resonance technique……...21

Fig. 2-8 (b) TE_{011} mode Cavity resonance technique……21

Fig. 2-9 Resonated mode of cylindrical dielectric sample under microwave test……..25

Fig. 3-1 (a) 99.9% $BaCO_3$……..31

Fig. 3-1 (b) 99.9% Nb_2O_5……...31

Fig. 3-2 Experimental flow chart……34

Fig. 3-3 TGA curve for the powder mixture of $BaCO_3$ and Nb_2O_5 as a function of temperature.
The heating rate was 5 °C/min…….36

Fig. 3-4 (a) Morphology of the $Ba_5Nb_4O_{15}$ powder prepared by calcination at 1000°C……37

Fig. 3-4 (b) Particle size distribution of pulverized $Ba_5Nb_4O_{15}$ powders……37

Fig. 3-5 Weight loss of $Ba_5Nb_4O_{15}$ specimens as a function of sintering temperature.
The weight loss of Nb_2O_5 specimens is also shown for comparison……....38

Fig. 3-6 (a) Relative density of $Ba_5Nb_4O_{15}$ specimens as a function of sintering temperature
The density of Nb_2O_5 specimens is also shown for comparison……38

doi:10.6342/NTU201702760

Fig. 3-6 (b) The shrinkage rate of $Ba_5Nb_4O_{15}$ specimens as a function of sintering temperature…40

Fig. 3-7 Typical free surface micrographs of $Ba_5Nb_4O_{15}$ specimens sintered at (a)1250°C (b)1300°C (c)1435°C……43

Fig. 3-8 Typical polished sections micrographs of $Ba_5Nb_4O_{15}$ specimens sintered at (a)1250°C (b)1300°C……44

Fig. 3-9 Typical polished sections micrographs of $Ba_5Nb_4O_{15}$ specimens sintered at (a)1350°C (b)1435°C……..44

Fig. 3-10 Typical fracture surfaces micrographs of $Ba_5Nb_4O_{15}$ specimens sintered at (a) 1250°C (b) 1300°C……...45

Fig. 3-11 Typical fracture surfaces micrographs of $Ba_5Nb_4O_{15}$ specimens sintered at (a) 1350°C (b) 1435°C……45

Fig. 3-12 (a) TEM micrograph of $Ba_5Nb_4O_{15}$ sintered at 1350 °C. The bright field image of grain (area 2,3) and grain boundary (area 1)……..46

Fig. 3-12 (b) TEM micrograph of $Ba_5Nb_4O_{15}$ sintered at 1350 °C. The diffraction patterns for grain (area 1) and grain boundary (area 2) are shown in the inset…….47

Fig. 3-12 (c) TEM micrograph of $Ba_5Nb_4O_{15}$ sintered at 1350 °C. Trapped pores are observed in the grain. (white arrow)……..48

Fig. 3-12 (d) TEM micrograph of $Ba_5Nb_4O_{15}$ sintered at 1435°C. Trapped pores are observed in the grain. (white arrow)……..48

Fig. 3-12 (e) TEM micrograph of $Ba_5Nb_4O_{15}$ sintered at 1435°C. Trapped pores are observed in the grain. (white arrow)……..49

Fig. 3-13 XRD patterns for 2θ from 25° to 70° of the $Ba_5Nb_4O_{15}$ powder and sintered specimens. SiO_2 was added as the external standard……..…….50

Fig. 3-14 XRD patterns for 2θ from 115° to 125° of the $Ba_5Nb_4O_{15}$…….51

Fig. 3-15 (a) XPS Nb 3d binding energy spectra for sintered $Ba_5Nb_4O_{15}$ specimens.....53

doi:10.6342/NTU201702760

Fig. 3-15 (b) XPS O 1s binding energy spectra for sintered $Ba_5Nb_4O_{15}$ specimens.....53

Fig. 3-16 (a) Dielectric constant and quality factor for $Ba_5Nb_4O_{15}$ specimen as a function of relative density……56

Fig. 3-16 (b) Dielectric constant and quality factor for $Ba_5Nb_4O_{15}$ specimen as a function of sintering temperature……...56

Fig. 3-17 (a) The quality factor vs. soaking time of sintering $Ba_5Nb_4O_{15}$ at 1300°C……65

Fig. 3-17 (b) XRD intensity of ordering lattice plane vs. soaking time at 1300°C…….66

Fig. 4-1 Experimental flow chart……72

Fig. 4-2.1 Particle size distribution for milled $Ba_5Nb_4O_{15}$ powders vs. milling time……..74

Fig. 4-3 Weight loss of $Ba_5Nb_4O_{15}$ specimen as a function of milled particle size……..75

Fig. 4-4 Milling media influence on quality factor of $Ba_5Nb_4O_{15}$……..76

Fig. 4-5 XRD patterns of the milled $Ba_5Nb_4O_{15}$ powder: (111) $BaCO_3$ (a) 0 min (b) 10min (c) 30min (d) 60min (e) 120min ◆:$Ba_5Nb_4O_{15}$ ×: $BaCO_3$…….78

Fig. 4-6 Sintered samples of milled $Ba_5Nb_4O_{15}$ with different milling time……78

Fig. 4-7 Barium ion concentration after milling…….80

Fig. 4-8 Morphology of $BaCO_3$ precipitated from filtering water of milled slurry…….80

Fig. 4-9 Mechanochemical reaction mechanism of barium ion dissolving in water……81

Fig. 4-10 (a) Free surface of unmill $Ba_5Nb_4O_{15}$……83

Fig. 4-10 (b) Free surface of mill 30min $Ba_5Nb_4O_{15}$……..83

Fig. 4-10 (c) Free surface of mill 60min $Ba_5Nb_4O_{15}$……...84

Fig. 4-10 (d) Free surface of mill 120min $Ba_5Nb_4O_{15}$……...…….84

Fig. 4-11 (a) Fracture surface of milled 60min $Ba_5Nb_4O_{15}$…….85

Fig. 4-11 (b) Fracture surface of milled 120min $Ba_5Nb_4O_{15}$……...85

Fig. 4-12 Milling vs. weight loss and relative density…….86

Fig. 4-13 The relative density vs. permittivity of $Ba_5Nb_4O_{15}$……88

doi:10.6342/NTU201702760

Fig. 4-14 Permittivity (*K*) and quality factor (*Qxf*) for the sintered $Ba_5Nb_4O_{15}$ specimens prepared using the powders milled for various times……89

Fig. 4-15 High angle diffraction pattern of milled $Ba_5Nb_4O_{15}$……90

Fig. 4-16 Rittinger's Law correlation fitting curve of milled $Ba_5Nb_4O_{15}$ powders……92

Fig. 4-17 Simulated anisotropic growth by composition variation……94

Fig. 4-18 (a) SEM micrographs for the $Ba_5Nb_4O_{15}$ sintered at 1435 °C. The cross section from the top of sintered surface reveal specific growing plane without excess $BaCO_3$...…95

Fig. 4-18 (b) SEM micrographs for the $Ba_5Nb_4O_{15}$ sintered at 1435 °C. The cross section from the top of sintered surface reveal specific growing plane with excess $BaCO_3$……..95

Fig. 4-19 (a) Comparison of Laue's diffraction patterns of sintered specimen milled 120min…...97

Fig. 4-19 (b) Comparison of sintered specimen at 1435°C line scans at 2θ angle at 38.15º (red: un-milled black: milling 120min)……97

Fig. 4-19 (c) Pole figure of mill and unmill $Ba_5Nb_4O_{15}$ with sintering at 1435°C……98

Fig. 4-20 (a) Bright field image of un-milled specimen at 1350°C……..101

Fig. 4-20 (b) SAED pattern of un-milled specimen at 1350°C……101

Fig. 4-20 (c) HRTEM Bright field image of un-milled specimen at 1350°C……101

Fig. 4-21 (a) Bright field image of un-milled specimen at 1435°C……...102

Fig. 4-21 (b) SAED pattern of un-milled specimen at 1435°C……102

Fig. 4-21 (c) HRTEM Bright field image of un-milled specimen at 1435°C……102

Fig. 4-22 (a) Bright field image of ion milled specimen at 1435°C……..102

Fig. 4-22 (b) SAED pattern of ion milled specimen at 1435°C……103

Fig. 4-23 (a) FIB preparation for milled 120min specimen at 1435°C……104

Fig. 4-23 (b) FIB preparation for milled 120min specimen at 1435°C……104

Fig. 4-24 (a) Bright field image of specimen is milling for 2h and sintered at 1435°C……105

Fig. 4-24 (b) HRTEM Bright field image of specimen is milling for 2h and sintered at 1435°C...105

doi:10.6342/NTU201702760

Fig. 4-24 (c) SAED pattern of specimen is milling for 2h and sintered at 1435°C……105

Fig. 4-25 High tilt angle at 70^{o} for EBSD analysis……106

Fig. 4-26 Band contrast of selected area 300μmX200μm……106

Fig. 4-27 IPF mapping of milled specimen……107

Fig. 4-28 Euler Mapping of milled specimen……107

Fig. 5-1 Experimental Flow Chart……115

Fig. 5-2 Milling effect on the sintering density of low firing $Ba_5Nb_4O_{15}$……117

Fig. 5-3 (a) Milling 30min of Low firing $Ba_5Nb_4O_{15}$……119

Fig. 5-3 (b) Milling 60min of Low firing $Ba_5Nb_4O_{15}$……119

Fig. 5-3 (c) Milling 120min of Low firing $Ba_5Nb_4O_{15}$……120

Fig. 5-4 Milling effect on $BaCO_3$ leaching of low firing $Ba_5Nb_4O_{15}$……121

Fig. 5-5 Weight loss vs. milling time at 900^{o}C……121

Fig. 5-6 (a) 900^{o}C sintering of $Ba_5Nb_4O_{15}$ at D_{50}=0.95um (a) free surface (b) fracture surface…..124

Fig. 5-6 (b) 900^{o}C sintering of $Ba_5Nb_4O_{15}$ at D_{50}=0.59um (a) free surface (b) fracture surface…..124

Fig. 5-6 (c) 900^{o}C sintering of $Ba_5Nb_4O_{15}$ at D_{50}=0.47um (a) free surface (b) fracture surface…..125

Fig. 5-6 (d) 900^{o}C sintering of $Ba_5Nb_4O_{15}$ at D_{50}=0.40um (a) free surface (b) fracture surface…..125

Fig. 5-7 (a) TMA experiment compare to low firing and high firing of $Ba_5Nb_4O_{15}$……126

Fig. 5-7 (b) TGA experiment of milling 120 min powder……126

Fig. 5-8 $Ba_5Nb_4O_{15}$ and silver cofiring cross section……127

Fig. 5-9 EPMA of $Ba_5Nb_4O_{15}$ and silver cofiring cross section……128

Fig. 5-10 Permittivity vs. Sintering Density of low firing $Ba_5Nb_4O_{15}$……130

Fig. 6-1 Mechanochemical mechanism of barium ion dissolving in water and $BaCO_3$ precipitation ……133

doi:10.6342/NTU201702760

List of Figures

Table 2-1 Microwave dielectric measurement method accuracy comparison[37] ……..22

Table 3-1 The different researches on $Ba_5Nb_4O_{15}$ sintering properties……..29

Table 3-2 HRTEM-EDX for grain area 1 and grain boundary area 2……47

Table 4-1 Particle size and sintered density of milled $Ba_5Nb_4O_{15}$ powders vs. milling time……74

Table 4-2 Grinding media contamination through milling time……76

Table 4-3 Temperature coefficient of resonated frequency at different milling time……109

Table 5-1 List of LTCC high permittivity microwave dielectric materials for LTCC…...……112

Table 5-2 EDX Analysis of A & B Site……120

doi:10.6342/NTU201702760

Chapter 1: Introduction

1. Introduction

The microwave dielectric ceramic materials are introduced into wireless communication industry for many decades. It exhibits attractive performance on high permittivity and quality factor. It can be applied on oscillator, filter or antenna components designed in high frequency circuit[1-3]. Additional point of application on endurance issue, those kinds of ceramic material exhibit temperature stability at resonate frequency. It can be near zero variance in extreme climate environment. The microwave dielectric materials were derived from a bunch of oxide ceramics. They have an advantage of size reduction for microwave components. All of components size depend on the half or quarter-wavelength rule which shorten $1/K^{1/2}$ (K: permittivity) length compared in free space. A novel application in miniaturized components must choose a high permittivity dielectric material which conserve energy with less dissipating at microwave frequency. Many kinds of high permittivity oxide ceramics have been successfully commercialized. The microwave dielectric materials are usually observed in orthorhombic or complex perovskite structure such as $Mg_{1-x}Ca_xTiO_3$、$BaTi_4O_9$、$Ba_2(Ti_xSn_{1-x})_9O_{20}$、$Zr_xSn_{1-x}TiO_4$、$Ba(Zn_{1/3}Ta_{2/3})O_3$、$Ba_{6-3x}RE_{8+2x}Ti_{18}O_{54}$. A candidate material in the $A_5B_4O_{15}$ (A=Ba, Sr, Ca, Mg, Zn ; B=Nb, Ta) system is hexagonal perovskite structure. One kind of material such as $Ba_5Nb_4O_{15}$ ceramics has been investigated for its high permittivity and quality factor in microwave frequency[4]. The merit of $Ba_5Nb_4O_{15}$ ceramics is suitable good dielectric constant ε_r : 38~42 and high quality factor $Q\times f$ = 20,000~42,000.

Recently, many researchers approached on low firing $Ba_5Nb_4O_{15}$ materials system which introduce glass additives to reduce sintering temperature through liquid phase assistance[5]. The application of technology aims on firing with silver metal together, the LTCC (Low temperature

doi:10.6342/NTU201702760

Co-fired Ceramics), can put in use for passive component at high frequency circuit. Meanwhile studying on co-firing of the dielectric and conductive metal materials is needed. Such as shrinkage mismatch, silver migration and mechanical strength of ceramic body are always of interests for commercialized manufacturers. But the process effects on characteristics of $Ba_5Nb_4O_{15}$ material are less reported in the past years. In this sense, studying on high temperature sintering of $Ba_5Nb_4O_{15}$ ceramic is a rational solution. The abnormal grain growth and relative density contravene as a function of temperature saying de-sintering phenomena usually illustrated on reports[6]. There is little report on the de-sintering mechanism. However, an approach on measuring ceramic density as a function of temperature and microstructure observation is the basis route of study.

On the other hand, there are many routes to homogenize ingredients, milling process is the basic solid-state route to manufacture ceramic materials powders using intensive mechanical energy. Regardless minor chemical impurity of raw materials, $BaCO_3$ and Nb_2O_5 sources are recommended by high purity level. Several technique procedures for ceramic powder preparation, such as milling / drying and calcination process, have been investigated in the past few decades. Eventually, the characteristics of $Ba_5Nb_4O_{15}$ strongly relate to effect of process parameters. In our studies, the de-sintering phenomena of $Ba_5Nb_4O_{15}$ was observed and the mechanochemical characteristic along milling process. The investigated root cause of such properties can be analyzed quantitively and mechanism was proposed.

For the applications of LTCC technology, $Ba_5Nb_4O_5$ with sintering additives can be cofired with silver metal which has been commercialized to make RF components. In our studies, the de-sintering and precipitation of $BaCO_3$ after milling process can be verified by microstructure at low sintering temperature.

doi:10.6342/NTU201702760

Chapter 2: Literature Survey

2.1 $Ba_5Nb_4O_{15}$ crystal structure

Most of microwave dielectrics materials with electrophysical properties are oxide ceramic systems[7]. One of them was surveyed on $A_5B_4O_{15}$ (A=Ba,Sr,Mg,Ca ; B=Nb,Ta) oxide compounds were the cation deficient hexagonal perovskite structure which vacant existence on B ions lattice site. The formula can be reduced to $AB_{0.8}O_3$ by accommodated charge neutrality between A and B metal cations. In general, the ideal structures can be classified to cubic perovskite structure ABO_3 that octahedral corners were shared by BO_6[8-9]. Compared to ideal cubic perovskite structure, it can be stacked along principle axes like layer-orientation perovskite structure. The stacking sequence are 1B cation vacancies per 5A cation means 20% of B cation site is occupied by vacancy and 5 layers stacking to be ABO_3.

$Ba_5Nb_4O_{15}$ compounds is classified to space group P-3m1 that can be close packing in five-layer sequences with shift type arranging the oxygen and barium atoms. Fig. 2-1. $Ba_5Nb_4O_{15}$ belongs to cation deficient perovskite structure type that lattice size is a = 5.8065Å and c = 11.8227Å. It is the crystal data collection and refinement from X-ray analysis. These compounds are hexagonal symmetry and has been identified as a layered structure which stacking plane parallel to {111}c (c = cubic). On the corner of $Ba_5Nb_4O_{15}$ lattice were structurally shared by NbO_6 octahedral and with the barium atom in the center of the cube surrounded by the niobium atoms. According to Goldschmidt's tolerance factor rule as equation (1)[10], the stability of lattice structure strongly relates to the distance of cation-anion bond at equilibrium state.

$$t = d_{(Ba\text{-}O)} / [2^{1/2} \times d_{(Nb\text{-}O)}] \quad \ldots\ldots (1)$$

Corner sharing of NbO_6 octahedral can eliminate the repulsion force between cations, meanwhile, the cation-anion distances create stress in the lattice. The tolerance factor can be

doi:10.6342/NTU201702760

identified to lattice structure, relaxation of bond energy will result in twisting of NbO_6 octahedral. For $Ba_4Nb_5O_{15}$ the tolerance factor (γ_{Ba}≈149pm, γ_{Nb}≈78pm, γ_O≈120pm) is calculated to t >1, finally niobium ions are tilted out of the octahedral center of NbO_6 to form hexagonal type perovskites structure. There is a strong anharmonicity distort the lattice structure from empty octahedral site of NbO_6 sub-lattice. The reduction of symmetry can lower energy and distort geometrically by d-shell orbitals from Jahn-Teller theorem[42].

The cation-deficient perovskite structure is attractive dielectric material applied to the microwave properties. $A_5B_4O_{15}$ dielectric ceramics system[11] reveal high relative permittivity (εr) with good quality factor (Q) and low temperature coefficient at resonator frequency (τf). Sreemoolanathan et al.[12] studied hexagonal structure of $Ba_5Nb_4O_{15}$ microwave dielectric ceramic proved its εr = 39, Q×f = 24,000 and τf = 78 ppm/°C. The structure of crystal symmetry exhibits five layered close-packed planes with Ba, Nb and O atoms sequentially. There is one layer plane without Nb atom has hexagonal packing which belongs to cation deficient perovskite structure. The microwave permittivity of the $Ba_5Nb_4O_{15}$ ceramics can be determined by the polarized phonon anomalies and related to density of ceramic body. The permittivity and quality factor can be varied by substituted atoms such as Sr or Ca atoms in A site to modify the symmetry of crystal. Many researchers on cation partial substitution on $A_5B5_4O_{15}$ crystal can tailor the microwave dielectric properties and sintering characteristic[13-14]. As the composition of cations are strongly related to the stability of resonated frequency following temperature variation,

doi:10.6342/NTU201702760

Cation deficient perovskite 5 layers stacking

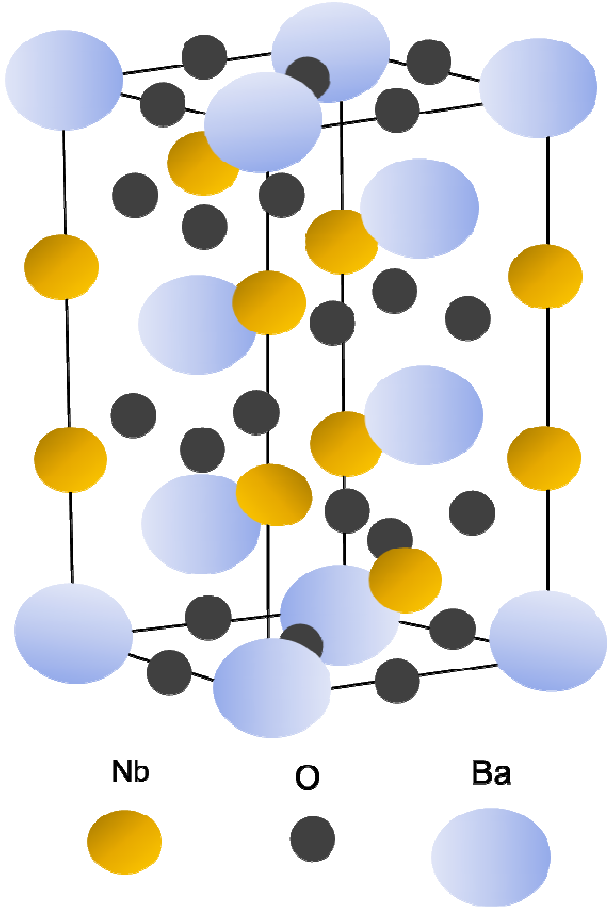

1: $Ba^{1}O^{1}_{3}$

2: $Ba^{2}Nb^{1}O^{2}_{3}$

3: $Ba^{3}Nb^{2}O^{3}_{3}$

4: $Ba^{3}Nb^{2}O^{2}_{3}$

5: $Ba^{2}Nb^{1}O^{3}_{3}$

1: $Ba^{1}O^{1}_{3}$

P-3m1 No.=164 Hexagonal Perovskite

a = 0.58065nm
c = 1.18227nm Density: 6.245 g/cm^3

Fig 2-1. Crystal Structure of $Ba_5Nb_4O_{15}$

doi:10.6342/NTU201702760

2.2 Homogenization of chemical composition with synthesis technology

Many synthetic processes can be applied on making ceramic products with different ingredients. The merit of process always relies on the product performance and economical benefit for end user. From the thermo-kinetics point of view, to shorten the synthesis time convert reactant to another substance, the driving force applied on homogenizing ingredients are physical length and temperature under atmosphere. Solid state process always is a simple and favorable technology to synthesis substance as following multistep process from mixing-drying-calcination-pulverization of powders in ceramic industry. Each process step derive from the principal of chemical physics theory will affect the final characteristics of substance. Such as the raw materials properties are chemical formula, particle size and impurity level, the mixing treatment for homogenizing compositions are physical energy of mechanical mixing technology and calcination technology of controlling temperature and atmosphere. The basic phase formation of $Ba_5Nb_4O_{15}$ has been published on the Fig. 2-2[15].

Simply statement of solid state process is so-call most of ingredients from powder forms and mixing by mechanical forces assisting with media. The mixed reactants will be homogenized by external force from temperature treatment. Their substances exhibit state of the art characteristics predictably. Most of interests for academic study do not focus on process research of synthesis technology. There are many troubles for industry application such as yield and degrading of characteristics withstanding severe environment. The $Ba_5Nb_4O_{15}$ is the candidate of microwave dielectric material but the performance and some physical properties is not the best choice one. Only low fired material system of such kind dielectric material has been commercialized[16].

No matter what kinds of ceramics material is existed, the product is prepared from solid state technology needs a mechanical energy to combine the solid ingredients with or without wet vehicle.

doi:10.6342/NTU201702760

There are aqueous or none aqueous conditions can play the role of lubricant and intermedia phase of ingredients engage reaction[17-18]. This kind of processing route has been applied for functional ceramics compounds. The reaction temperature can be reduced by activated mechanical energy through chemical reactivity of raw material. The mechanochemical phenomena happened in many oxide ceramics effected on microstructure and physical properties. The mechanical energy can be generated by speed of rotation, prolonging time and media in raw materials. It was clear that crystalline size or particle size would be reduced when increase the mechanical energy. The mechanical energy leads to form a new surface with high strain on particles can be released under the solid state chemical reaction. The solid-state synthesis technology can be improved by this novel mechanochemical treatment to form $Ba_5Nb_4O_{15}$ ceramic. The dielectric properties of sintered $Ba_5Nb_4O_{15}$ ceramic can be compared to those prepared by different milling time in this study. In this stage, the vehicle plays another role of chemical ingredient to contact new free surface as a reactant. There is more chemical gradient to enhance energy exchange during these processes contributed by mechanical activation. The purpose of the present study is to verify the mechanochemical effects of $Ba_5Nb_4O_{15}$ ceramic materials on microwave dielectric properties and sintering characteristic.

doi:10.6342/NTU201702760

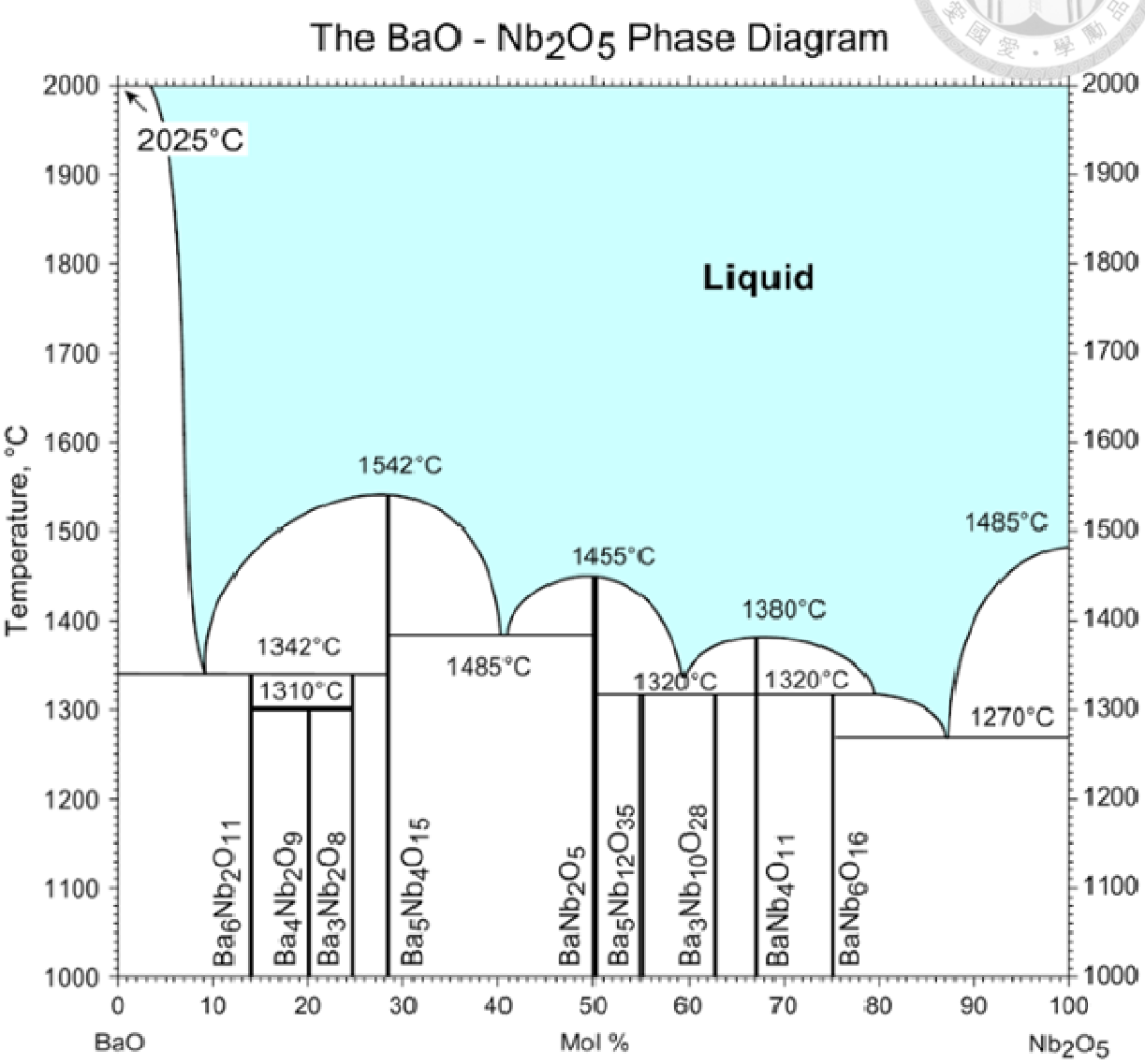

Fig 2-2. Phase Diagram of $BaO\text{-}Nb_2O_5$[15]

doi:10.6342/NTU201702760

2.3 Densification by liquid phase sintering

In general, the ceramic material sintering technique can be grouped two kinds process, solid state sintering and liquid phase sintering, used to control the powder densification. The purpose of sintering is microstructural control as to be dense body fitting material property or performance. Kang[19] illustrated the sintering route from phase diagram in Fig. 2-3. There are four kinds of sintering routes based on solid to liquid phase mass transportation. As a thermal dynamic equivalent diagram, the sintering temperature T_1-T_3 near to phase transformation line of different phases exhibits different sintering mechanism. Basically, the phase diagram of BaO-Nb_2O_5 oxide ceramic is proposed on attached Fig. 2-2[15] and melting point of $Ba_5Nb_4O_{15}$ is near to 1547°C. If sintering temperature of $Ba_5Nb_4O_{15}$ under 1342°C confirmed to be solid state sintering but it will occur probably liquid phase sintering near the solidification line of a stoichiometric composition.

doi:10.6342/NTU201702760

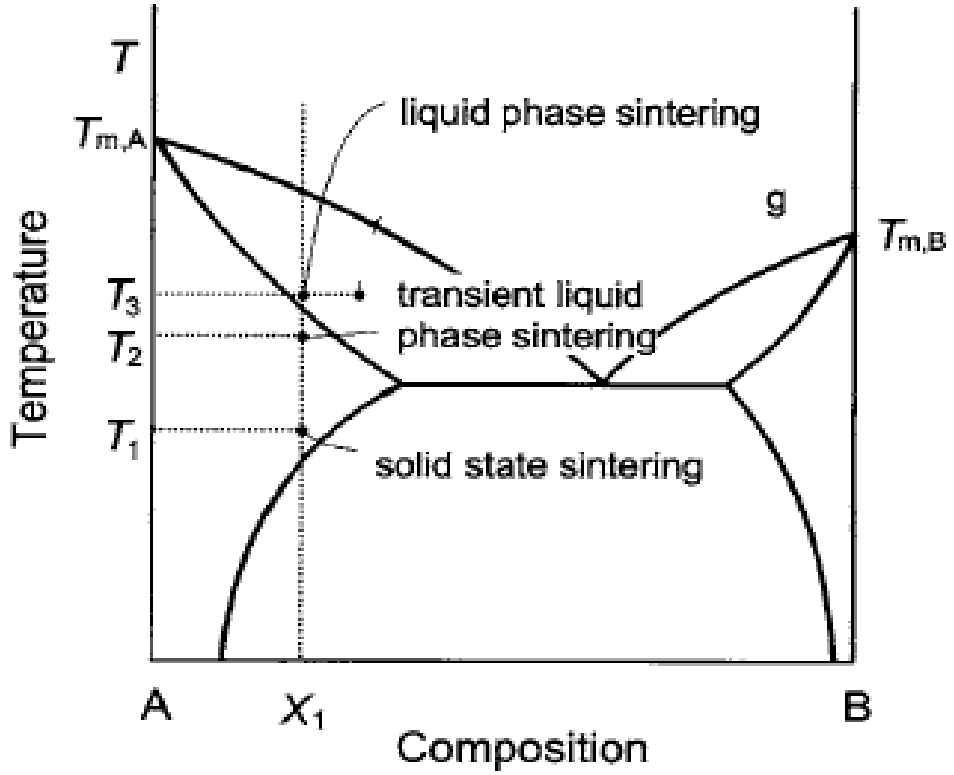

Fig 2-3. Illustration of various types of sintering routes[19]

doi:10.6342/NTU201702760

Liquid phase sintering (LPS) is a well esatablished method to reduce sintering temperature accomplish powder densification in the presence of a liquid. There are several theories of LPS describe the densification stages such as German and Kingery model[20-22]. Obviously microstructure development of sintered dense body gives an evidence of LPS process from identification of interfacial grains. To illustrate the abnormal grain growth phenomena at final stage of grain growth[23], it is controlled by diffusion of atoms and reaction of liquid/solid interface. The description proposed by Lifshitz, Slyozov and Wagner is named LSW theory[24-25]. The assumption of LSW theory can't explain the oriented grain growth. Faceted grains growth is governed by interface reaction that each crystallographic plane has certain diffusion coefficient varies with its orientation. The behaviors of grain growth can be simulated numerically if it is growing or dissolving at a critical size. The grains growth is simplified as equations derived from two kinds of mechanisms. Fig. 2-4 (a)~(b)

From the grain growth point of view, it is obviously diffusion or reaction controlled atoms dominate the grain. For grain growth rate on different crystallographic orientations based on the interfacial energy, the low interfacial energies appear slowly growing planes. Usually the simple polyhedral or anisotropic grain shape are belonged to reaction-controlled growth. On the other hand, a fast dissolving planes reveal a high interfacial energy for anisotropic grain growth.

doi:10.6342/NTU201702760

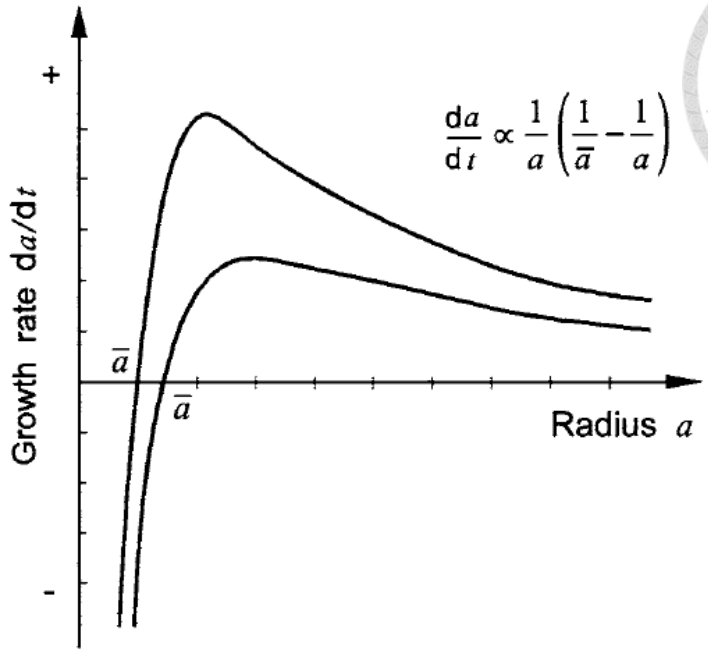

Fig. 2-4 (a) variation of particle growth rate for diffusion-controlled growth[19]

.

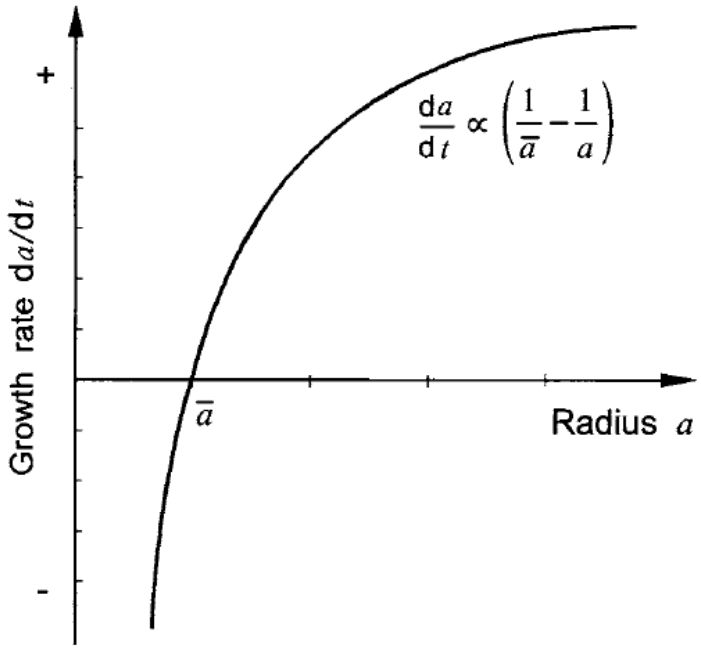

Fig. 2-4 (b) variation of particle growth rate for reaction-controlled growth[19]

doi:10.6342/NTU201702760

In the innovative technology by the presence of liquid phase, many kinds of sintering additives can play the role to enhance chemical reaction or increase diffusivity on the primary powders. Usually the particular additives were selected from ingredients of phase diagram. All of varied compositions were examined the relative density after a firing procedure. Many researches on additives to lower sintering temperature of $Ba_5Nb_4O_{15}$ material have been commercialized by LTCC technology[26-28]. The mains liquid phase sintering additives such as B_2O_3, CuO and glass dopes can reduce the reaction free energy. The sintering temperature is under 900^oC that $Ba_5Nb_4O_{15}$ cofire with silver metal. This system occurs to reduce the interfacial energy of chemical composition associate with matrix and solute composition. As a result, there is an activation energy for the total area of boundary to be reduced by solution and precipitation in liquid phase. The grain coarsening in the final stage of sintering accompanied was always verified from microstructure evolution.[29-30]

doi:10.6342/NTU201702760

2.4 Polarization of $Ba_5Nb_4O_{15}$ dielectric properties under microwave frequency

The behavior of $Ba_5Nb_4O_{15}$ microwave dielectric material has the macroscopic polarization which are formed by an inherently permanent dipole orientated dependence with the direction of the external electric field. The polarization is not instantaneous and need time to recovery the storage energy when release the applied field. $Ba_5Nb_4O_{15}$ can exhibit a low dissipated energy when dipolar polarization lost the response to electric fields at the highest frequencies.

In the presence of an oscillated electric field, the dielectric materials are polarized to dipole moment in the filed act like clouds charge. A classical dielectric model at different frequency of electric field oscillation can be classified by the dielectric material with four types models. The polarization model is varied by the relationship between the frequency of electric field and dipole moment. When the frequency of electric field is higher, the dipole moment tends to be the model from ionic to electric polarization. The essence of model in physics are summarized to be (a) space charge (Maxwell Wagner effect): Interfacial polarization which build up the charge at the interface (b) dipolar polarization: A permanent dipole result from electric field (c) ionic polarization: relative displacement of nuclei due to separation of positive and negative field (d) electronic polarization: arises from the realignment of electrons in the specific nuclei[31]. Fig. 2-5. In the electromagnetic spectrum range, microwave frequency extends the carrier wave range from 3MHz to 300GHz which correspond to wavelength between meter to millimeter scale respectively. The electromagnetic radiation wave will interact with condensed matter induce the vibration of lattice. The condensed matter will be polarized by electromagnetic wave like charge carriers are bound to relative displacements between positive and negative field.

doi:10.6342/NTU201702760

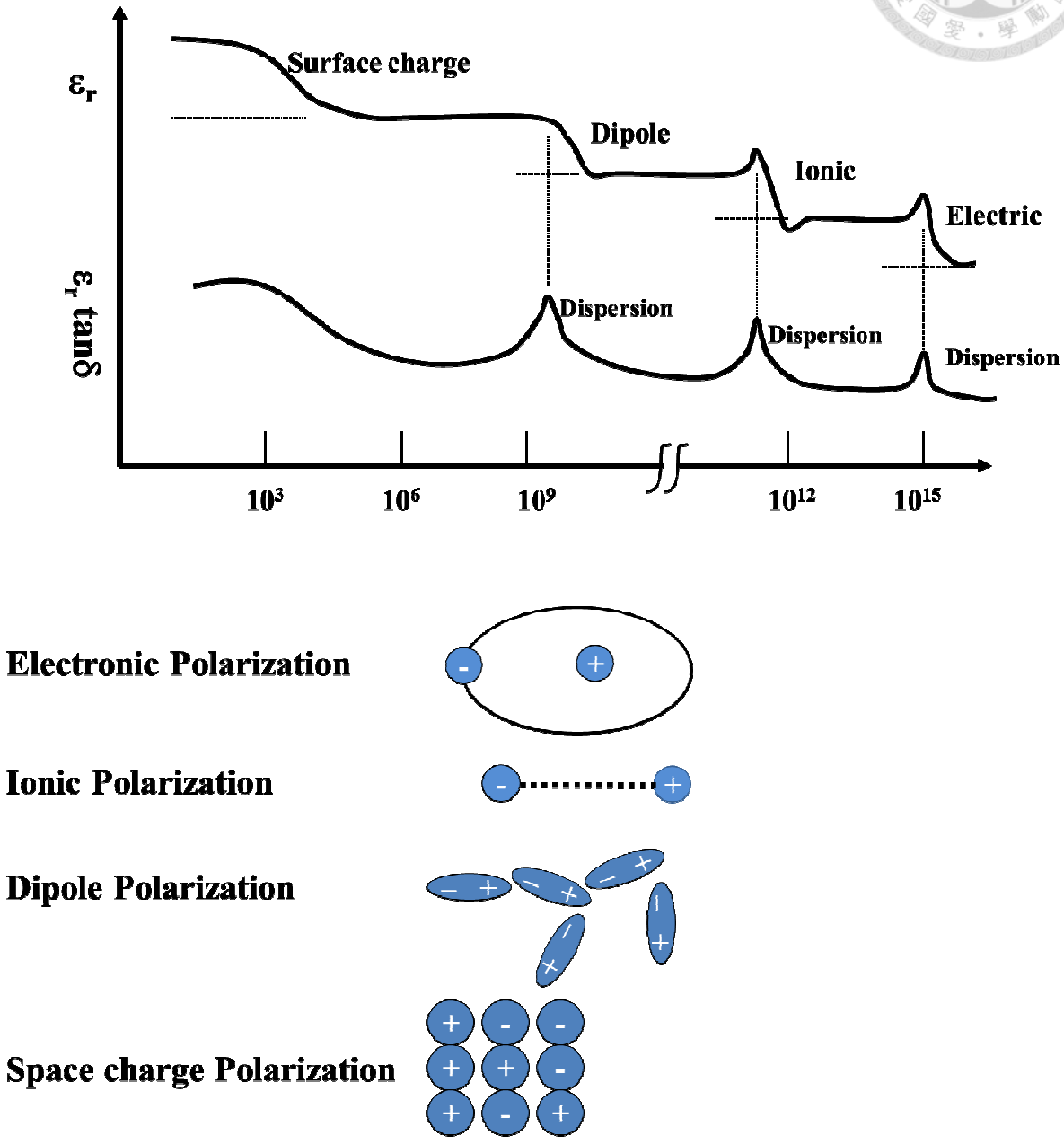

Fig 2-5. Models of polarization

doi:10.6342/NTU201702760

Microwave measurement techniques applied for permittivity and dielectric loss properties can be categorized to transmission-reflection and resonance methods[32-34]. In generally, the resonance method was classified two types of resonate models in closed cavity and open resonator Fig.2-6. This resonator model was constructed by conducting metal and lossy geometric structure which can be measured under microwave region. Due to microwave range energy is reduced by the conductive or magnetic material in the space, the incident EM wave propagation nearly reflected and the metallic case shields electromagnetic wave with preventing radiation loss. Both of the dielectric constant and loss factor can be deduced from the resonant frequency under a typical size. For industry application viewpoint, only easy and simple measurement method can be introduced to standardization procedure. Two most commonly used measurement methods are mainly introduced to microwave dielectric material applied to electromagnetic wave frequency under 40GHz.

doi:10.6342/NTU201702760

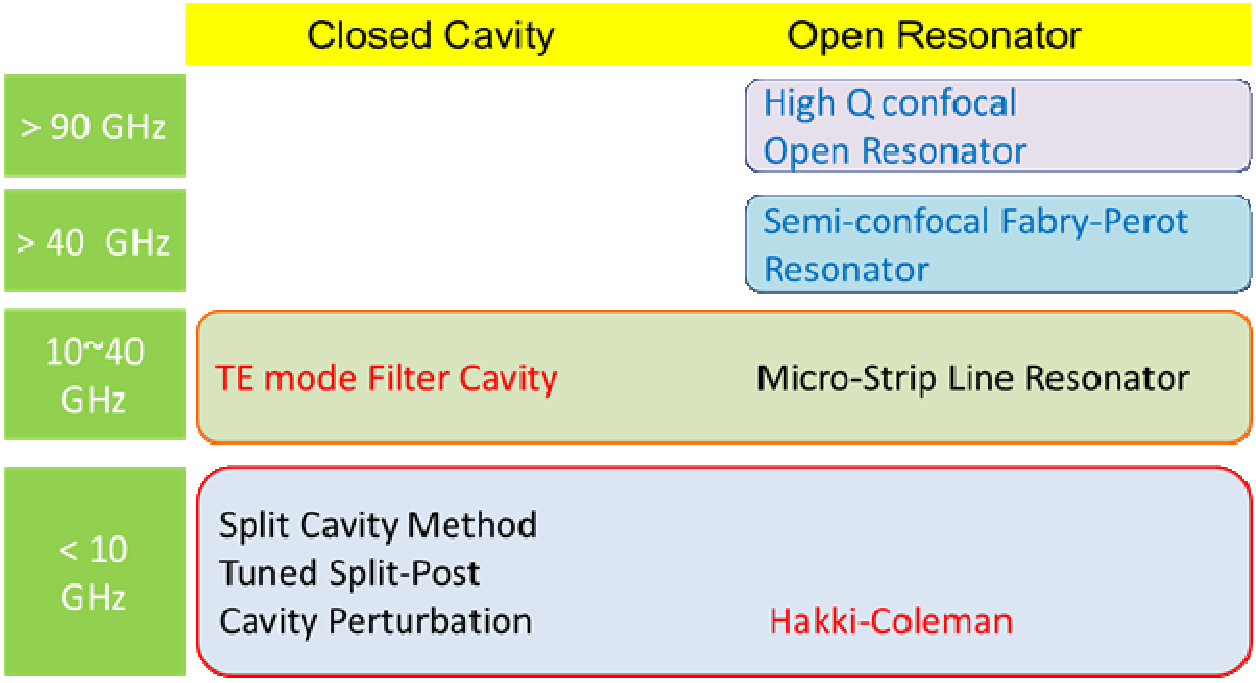

Fig 2-6. Microwave characteristics measurement methods

doi:10.6342/NTU201702760

2.4.1 Hakki-Coleman method

A general post-resonance technique which was similar to parallel metal plate proposed by B.W Hakki and P.D Coleman in 1960 for measurement of dielectric constant[35]. The dielectric constant is computed the inductive and capacitive of reactance at resonate TE_{011} mode derived from cylindrical dielectric sample[36-37] Fig. 2-7. It is complicated calculations for mathematical function which derived a complex Besell's equation to get the real part of permittivity by computer program. The measurement accuracy is higher that variation error under 0.5% and can be available to high permittivity material. Only one disadvantage of the method was low measurement accuracy of loss factor that the surface resistance of metal plates could affect the conductivity. To overcome the term of conductivity in the derived equation, two dielectric samples with TE_{011} and TE_{012} mode must be measured with the same material size. This method has been standardized under the regulation rule of JIS R1627 and IEC-61338-1-3.[38-39]

doi:10.6342/NTU201702760

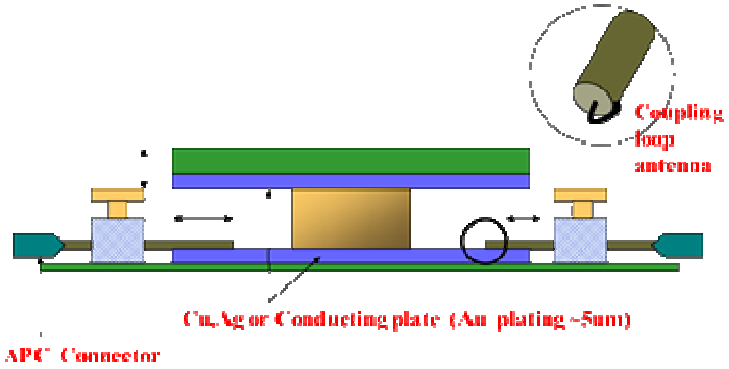

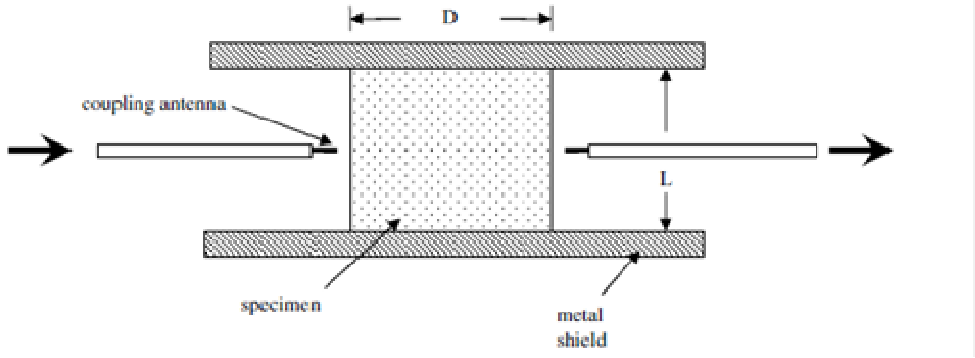

Fig 2-7 (a) Hakki-Coleman resonance technique[36]

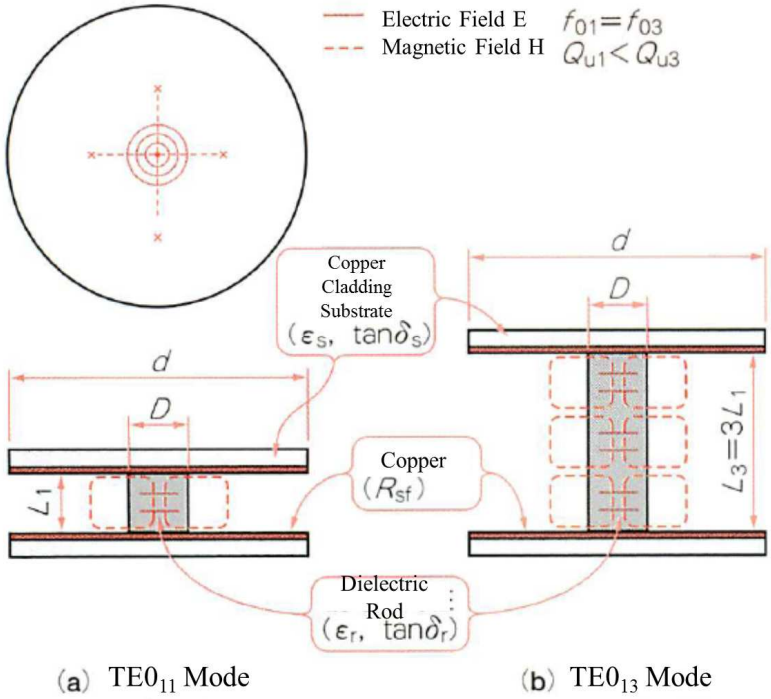

Fig. 2-7 (b) Cylindrical samples for permittivity and quality factor measurement[37]

doi:10.6342/NTU201702760

2.4.2 Cavity resonate method

Whatever the development of electromagnetic field computation, for simplifying measuring structure, the dielectric resonator is designed as a cylindrical type. The rod sample is placed inside a closed metal cavity. The waveguide reflection resonance mode in the cavity can get a highly accurate measurement for dielectric loss which resultant low conducting loss. Due to the samples suspended inside the metal shields and all resonated radiation wave conserved in the case, the conductor loss will be lower than that of Hakki–Coleman technique.

J. Krupka[40] proposed a simplified cylindrical metal cavity which restrict size of the sample and height of resonator cavity for measuring the resonate peak with the $TE_{01\delta}$ mode. The calculation equations for the dielectric properties are more easily derived than those of other modes. Referring to the cylindrical cavity structure in Fig. 2-8 (a)&(b), both of distance on top and bottom of sample to metal case are nearly equal. The $TE_{01\delta}$ mode resonated peak is easily identified from sweeping spectrum but lack of exact solutions of Maxwell's equation as same in parallel plate structure. The cavity structure family of dielectric resonator for precise measurement can be equipped with Vector Network Analyzer. It is installed specialized calculation software for determination of complex permittivity and quality factor of microwave dielectric material.

However, cavity resonant method can extract TE_{011} mode by the presence of a sample in the cylindrical cavity as Fig. 2-8. The plate type of dielectric sample cause to electric field perturbation when inserted in the metal cavity. That measurement method was committed to standardization regulation under the JIS R1641, IEC62562 (Plate)

doi:10.6342/NTU201702760

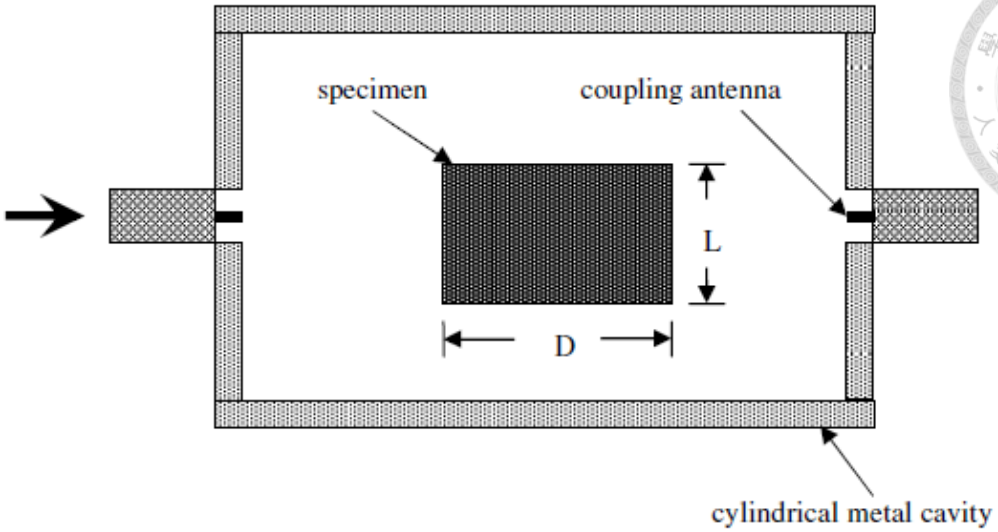

Fig. 2-8 (a) Cylindrical cavity $TE_{01\delta}$ resonance technique[36]

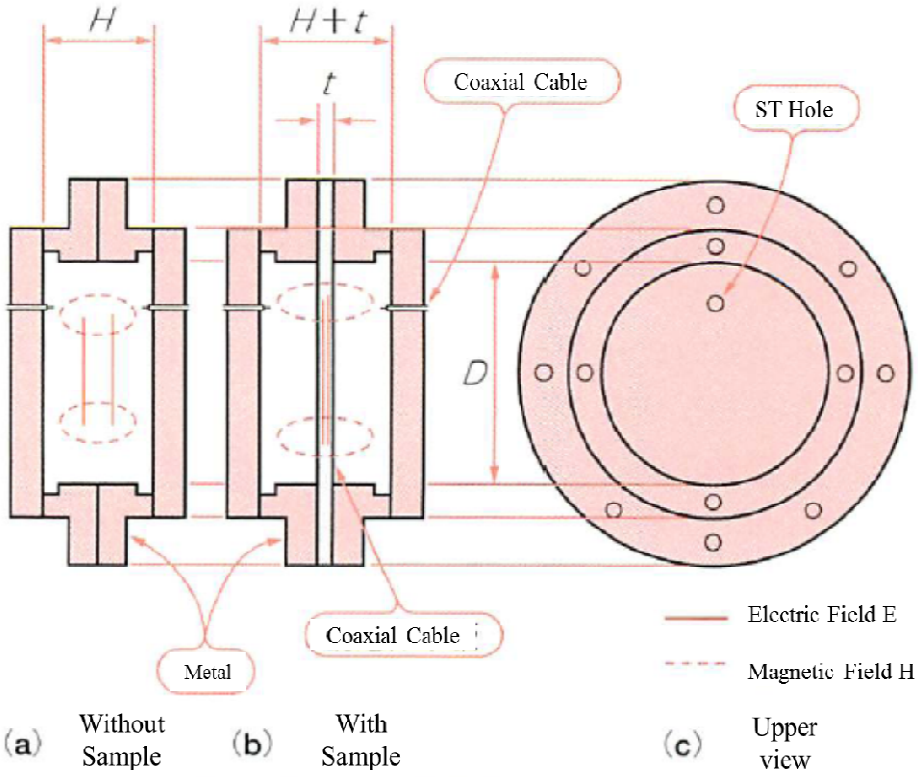

Fig. 2-8 (b) TE_{011} mode Cavity resonance technique[37]

doi:10.6342/NTU201702760

Table 2-1 Microwave dielectric measurement method accuracy comparison[37]

Measurement Method	Regulation STD	Sample Type	Parameter	f_0 [GHz]	ε_r	tanδ	σ_r
					$\Delta\varepsilon_r$ [%]	Δtanδ [%]	$\Delta\sigma_r$ [%]
Parrallel Plate	JPCA-FC01(2006)	Disk	ε_r tanδ	2~65	1.1~10	10^{-2}~10^{-4}	
	JFIA-FP001(2006)				±0.2~1.0	±5~20	
Cavity Resonate	JIS R 1641 (2007)	Plate	ε_r tanδ	2~40	1.1~50	10^{-3}~10^{-6}	
	IEC 62562 (2009)				±0.2~0.5	±2~10	
Wave Guide	JIS R 1660-1(2004)	Plate	ε_r tanδ	30~100	1.1~50	10^{-3}~10^{-6}	
	IEC 61338-1-4(2005)				±0.2~1.0	±2~10	
Dielectric Resonate	JIS R 1627(1996)	Cylinder	ε_r tanδ	2~30	2~1000	10^{-3}~10^{-7}	10~100
	IEC 61338-1-3(1999)		R_{sf} σ_r		±0.2~0.5	±5~20	±2~10
MIC type dielectric resonate		Plate Conductor	R_{sf} σ_r	2~30	-	-	10~100
					-	-	±5~15
TM_{010} mode cavity resonate		Rod	ε_r tanδ	1~30	1.1~50	10^{-2}~10^{-4}	
					±1.0~7.0	±10~30	

doi:10.6342/NTU201702760

2.4.3 Mathematical calculation of permittivity and quality factor

To standardize the permittivity and quality factor measurement method in commercialized regulation, the dielectric resonate method has been published on JIS R1627(1996) and IEC61338-1-3(1999). When electromagnetic wave propagates in the space to conserve the energy, the resonance phenomena occurs at the waves travel at different regions such metal and low-loss materials medium. The shape of resonator represents the boundary of wave function geometrically such as rectangular or cylindrical configurations. In general, a cylindrical type resonator is easily obtained by ceramic forming process. This resonate structure can be used to generate oscillation at specific frequency. The frequency was indicated to calculate ε_r from equation (1) and tan δ of low-loss material sample from equation (3) mathematically.[33-34]

$$\varepsilon_r = (\lambda_0/\pi D)^2(u^2+v^2)+1 \qquad \lambda_0 = c / f_0 \quad \ldots\ldots\ldots\ldots (1)$$

$$v^2 = (\pi D/\lambda_0)^2((l\lambda_0/2L)^2-1)$$

$$J_0(u) / J_1(u) = - vK_0(v) / K_1(v) \quad \ldots\ldots\ldots\ldots (2)$$

c: light velocity in vacuum D: diameter of specimen L: height of specimen

$J_n(u)$: Bessel function of first kind $K_n(v)$: Modified Bessel function of second kind

$$\tan\delta = A / Q_u - BR_s \quad \ldots\ldots\ldots\ldots\ldots\ldots\ldots\ldots (3)$$

$$A = 1+W/\varepsilon_r \qquad B = (l\lambda_0/2L)^3(1+W)/(30\pi^2\varepsilon_r l)$$

$$R_s = (\pi f_0 \mu/\sigma)^{1/2}$$

$$W = [J_1^2(u) / K_1^2(v)] [K_0(v)K_2(v) - K_1^2(v)] / [J_1^2(u) - J_0(u)J_2(u)]$$

Q_u = unload Q R_s = surface resistivity of metal plate

Both of characteristic were obtained from resonated frequency values f_0 and peak spectrum with half power band width of 3dB attenuation. The unloaded quality factor Q can be deduced from loaded quality factor which formed as Maxwell wave equation in cylindrical coordination. A

doi:10.6342/NTU201702760

complicated Bessel equation can be treated as scalar Helmholtz equation by separation of variables method. Remained Bessel equations can derive the radial direction of rod for both real and imaginary parts. Finally, the ratio of Bessel's first kind and modified Bessel's second kind equations (2) can be derived by graphical or numerical methods. The resonated electromagnetic wave travelling in a waveguide can possibly propagate several modes. The dominant mode has the lowest cutoff frequency is determined by the physical dimension. For example, transverse electric field (TE) mode means no electric field in the direction of wave propagation. It happened at certain frequency which boundary condition has radiation wave pattern can be described in term of transverse mode. Such as a K=38 with 8mm diameter 3.8mm height dielectric material was measured under Hakki- Coleman method, the resonated mode of full spectrum frequency can be observed by Network analyzer in Fig. 2-9. When select the TE_{011} mode frequency f_0 and confirmed the second twice height cylindrical sample with TE_{012} mode f_{02}, the permittivity ε_r and dissipated factor tan δ can be derived by computer program.

doi:10.6342/NTU201702760

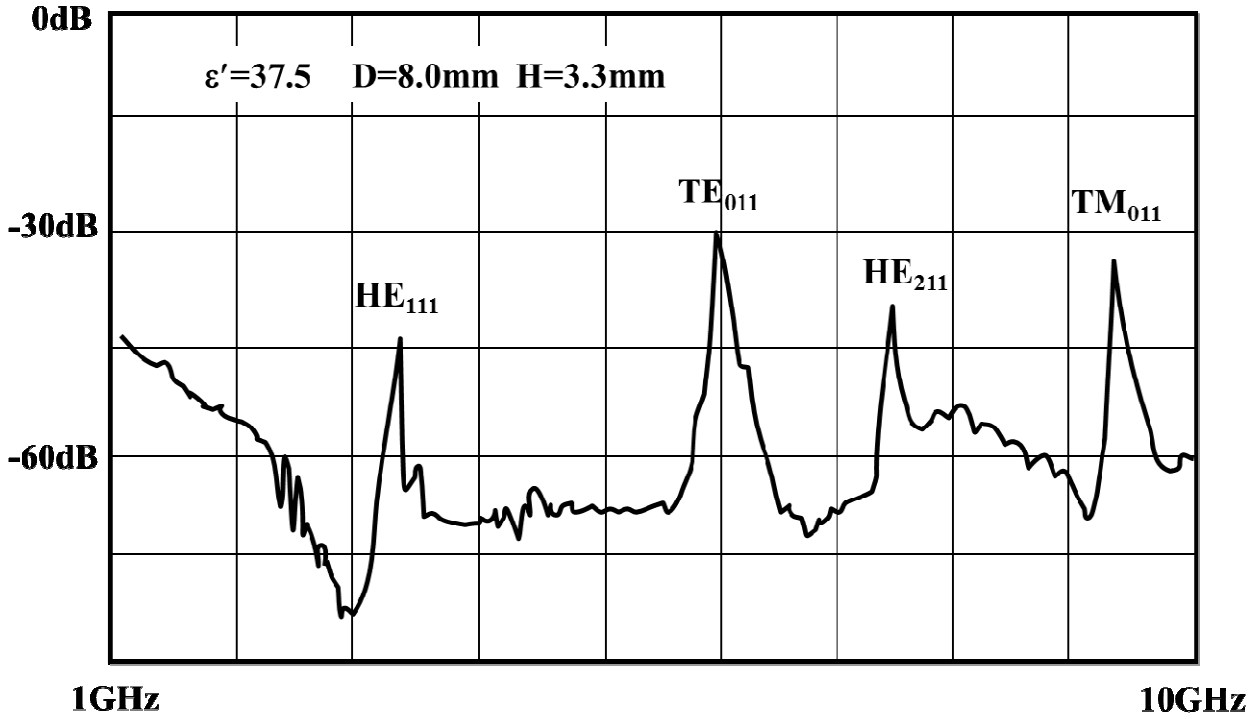

Fig. 2-9 Resonated mode of cylindrical dielectric sample under microwave test

doi:10.6342/NTU201702760

2.5 Ordering structure of high quality factor

There are a large number of A- or B-site vacant perovskite materials applied for microwave application. The crystal structural ordering of ceramics always improved the microwave dielectric properties especially for low loss cation deficient perovskite materials[41]. Fundamentally from crystallographic chemistry point of view, there are three mechanisms express the perovskite distortion including orbital ordering (Jahn-Teller distortion)[42], cation ordering and octahedra tilting[43-44]. The deficient cations cause ideal perovskite structure distorted and driven by electronic instabilities of the octahedral metal ion. The crystal distortion often combined effects of those mechanisms in structural features. The bond between B-O of BO_6 has a strong electronegativity to be rigid structure maintains its core-share connectivity. Only tilting the octahedra can contribute an energetic stabilization to be lowest energy distortion mode[45]. The internal strain derived from lattice distortion affects the polarization loss factor which can be varied non-linearly by cations concentration. Meanwhile, the dielectric constant and the temperature coefficient of the resonant frequency linearly changes with the composition. Internal lattice strain can be verified usually by FWHM of X-ray diffraction pattern but it is hardly achieved. Sometime the superlattice ordering is an indication of Q factors enhanced by the driving force from long time temperature sintering. The intensity ratio of a superlattice peak to a fundamental peak of x-ray diffractometry (XRD) is the method for evaluating the degree of ordering. The order parameter, *S*, which is calculated from the observed and calculated values of the superlattice peaks intensity ratio[46].

$$S = \{[I(\text{superlattice A})_{obs}/I(\text{fundamental B})_{obs}] \div [\, I(\text{superlattice A})_{cal}/I(\text{fundamental B})_{cal}]\}^{1/2}$$

The degree of structural order from ratio of plane intensity has been generally considered to identity Q factors improvement quantitatively.

doi:10.6342/NTU201702760

Chapter 3: Sintering Behavior and Microwave Properties of $Ba_5Nb_4O_{15}$

3.1 Introduction

Microwave dielectric ceramics had a good quality factor were always sintered at high temperature. They can be applied widely on wireless communication industry demanded for filter, resonator and antenna components. A novel application in miniaturized components must choice a high permittivity dielectric material due to the wavelength decrease in the medium. The high permittivity microwave material $Ba_5Nb_4O_{15}$ has been commercialized. The merit of $Ba_5Nb_4O_{15}$ ceramic exhibits its economical application for good dielectric constant and quality factor.

A cation-deficient perovskite[47-48], $Ba_5Nb_4O_{15}$, has attracted a lot of attention in last two decades. Though $Ba_5Nb_4O_{15}$ reveals the advantage on microwave properties, the preparation of dense of $Ba_5Nb_4O_{15}$ through pressureless sintering is a challenging task. Apart from $Ba_5Nb_4O_{15}$ perovskite, the existing literatures demonstrated that the abnormal grain growth and density decrease during high temperature sintering (de-sintering) are common for other microwave ceramics. For example, both abnormal grain growth and de-sintering at elevated temperatures are found for $Ba(Zn_{1/3}Ta_{2/3})O_3$. Similar to the case of $Ba_5Nb_4O_{15}$, little attention has been paid to these important issues.

The microwave performance of perovskite depends strongly on its intrinsic and extrinsic characteristics. The crystallographic structure belongs to the intrinsic characteristic; the microstructural features to the extrinsic characteristics. As far as the permittivity and quality factor are concerned, the amount of pore is the key parameter. Both permittivity and quality factor decrease with the increase of porosity. In this chapter study, the sintering behavior of $Ba_5Nb_4O_{15}$ perovskite is investigated. The microstructure and crystalline structure are characterized. The effect of sintering on microwave performance of $Ba_5Nb_4O_{15}$ perovskite is then established.

doi:10.6342/NTU201702760

Microwave characteristics of different researchers studied on sintered $Ba_5Nb_4O_{15}$ were compared in the Table 3-1. All examined results of dielectric samples were clearly performed on high relative density. The difficulty of getting high relative density was overcome by sintering technology. Adding sintering additives and lowering sintering temperature treatment can avoid the matter of fact in abnormal grain growth. Why has abnormal grain growth and what happened in de-sintering at high temperature are our interests for investigation in this study.

doi:10.6342/NTU201702760

Table 3-1 The different researches on $Ba_5Nb_4O_{15}$ sintering properties

Sintering Condition	Relative Density	Permittivity *K*	Quality F. Q*xf*	Remark	Reference
1420°C 4Hr	92.0%	41	7,100	No Additives	Streemoolanathan[12]
1250°C 2Hr	97.5%	40	56,000	B_2O_3/V_2O_5 Additives	Kim[13]
1450°C 4Hr	97.3%	39.5	22,700	None Calcination	Chen[17]
1380°C 2Hr	96.0%	39	23,700	No Additives	Jawahar[73]
1250°C 5Hr	97.3%	34	32,000	None Calcination	Kumar[18]

doi:10.6342/NTU201702760

3.2 Experimental

3.2.1 Raw material preparation

Samples of $Ba_5Nb_4O_{15}$ ceramics were prepared by conventional solid state reaction route. The starting materials were $BaCO_3$ and Nb_2O_5. and purity level was higher than 99.9%. The morphology of raw materials revealed in Fig.3-1 (a) & (b). Confirming both initial properties of raw materials were checked by particles size analyzer (LA-920, Horiba Co., Japan) and morphology by scanning type electron microscope (JSM-6360, JEOL Co., Japan). Both $BaCO_3$ and Nb_2O_5 materials weighted in stoichiometric mole ratio 1.000 are mixed with distilled water. The milling media was 2mm zirconia balls and planetary mill rotated 220rpm in 30min. The mixed slurry then dried and pressed powders into 25mm cake were calcined at 1000°C for 2.5 hours. After drying, the powder mixture was packed into cakes with a diameter of 25 mm. The weight loss behavior of the powder mixture at elevated temperatures was evaluated with a thermogravimetry analysis (TGA, MTC-1000S, Mac Science, Japan). The heating rate used was 5 °C/min. Based on the TGA result, the calcination for the $BaCO_3$ and Nb_2O_5 powder mixture was carried out at 1000°C for 2 h. The calcined cakes were pulverized by agate mortar to obtain the $Ba_5Nb_4O_{15}$ powder. The particle size was analyzed with a laser size analyzer (LA-920, Horiba Co., Japan). Furthermore, the calcined $Ba_5Nb_4O_{15}$ cake pulverized by agate mortar and milled to 2.3um.

doi:10.6342/NTU201702760

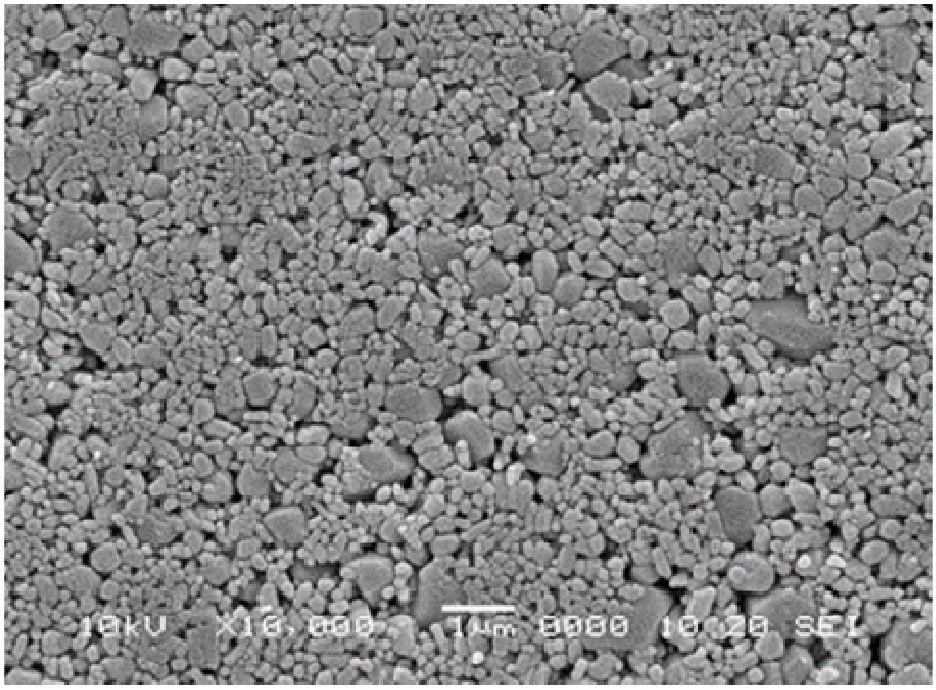

Fig 3-1 (a) 99.9% $BaCO_3$

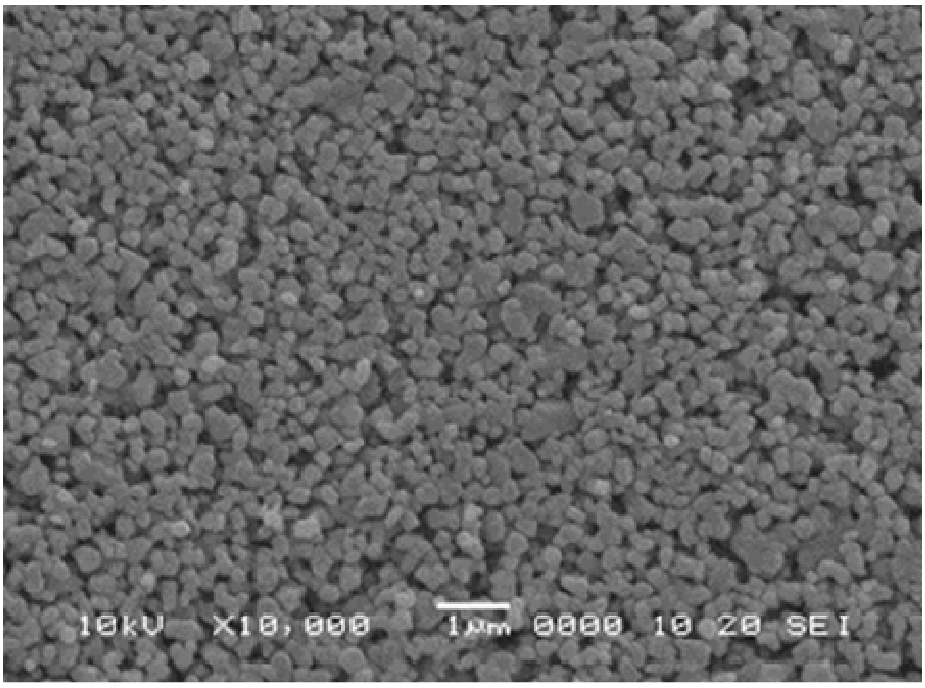

Fig 3-1 (b) 99.9% Nb_2O_5

doi:10.6342/NTU201702760

3.2.2 Experimental flow chart

The source of the $Ba_5Nb_4O_{15}$ calcined powder was prepared under pulverized process without wet milling in water. For ability of ceramic powder granules were formed as usual in the mold. The powder compact was prepared by uniaxial pressing at 140 MPa, assisting with the addition of a small amount (4 wt.%) of PVA. The relative density of the green $Ba_5Nb_4O_{15}$ powder compact is 64 %. The diameter of the green pellets was 10 mm; the thickness was 2.0 mm. The de-binder temperature was 600°C. The sintering temperature varied from 1200°C to 1435°C. The dwell time at the sintering temperature was 2.5 h. The heating and cooling rates were 2.5 °C/min. The weight before and after sintering was monitored. Some Nb_2O_5 specimens were also prepared by sintering at 1200°C to 1435°C for comparison purpose. For each sintering condition, at least 10 specimens were prepared. The density of the fired discs was determined with Archimedes method. The relative density of the sintered specimen was calculated using a value of 6.25 g/cm3 for the theoretical density of $Ba_5Nb_4O_{15}$. The phase analysis was conducted with an X-ray diffractometer (XRD, D8, Bruker Advance, Germany). Two ranges were scanned, the scanning rate for lower angle range ($25\sim70^o$) was 0.04 degree/step and 1 s/step; for higher angle range ($115\sim125^o$) was 0.01 degree/step and 2.0 s/step. Before the XRD analysis, the sintered specimens were crushed into powder. A small amount (5.0 wt.%) of silica was pre-mixed with the powder to serve as an external standard for the XRD analysis.

Microstructure observation was conducted with scanning electron microscopy (JSM-6360, JEOL Co., Japan) and transmission electron microscopy (JEM-2100, JEOL Co., Japan). For SEM observation, the cross-section of the sintered specimens was exposed by grinding and polishing. A thermal etching treatment was conducted at 1200°C to reveal the grain boundaries. For TEM observation, sintered samples were sectioned and thinner area by ionized Argon miller. The

doi:10.6342/NTU201702760

microwave characteristics of the sintered specimen were analyzed with a network analyzer (HP-8720ET, Agilent, USA) following a standardized Hakki-Coleman and Cavity method. To verify the phenomena of de-sintering and deduce the reduction of cation may happen at high temperature. The binding energy state of niobium ions and in the sintered $Ba_5Nb_4O_{15}$ specimen was determined with X-ray photoelectron spectroscopy[49] (XPS, ESCALAB 250, Thermo Scientific, UK). Fig. 3-2.

doi:10.6342/NTU201702760

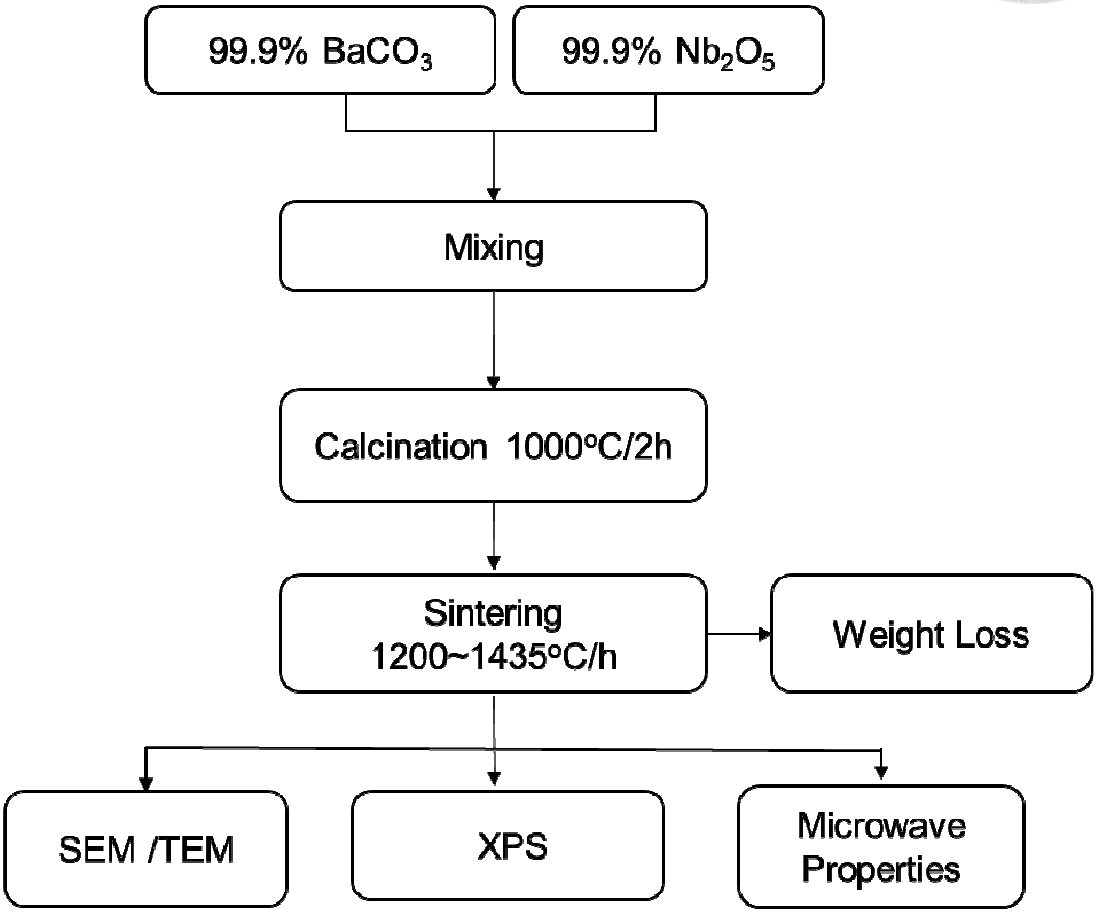

Fig. 3-2 Experimental flow chart

doi:10.6342/NTU201702760

3.3 Results

3.3.1 Weight loss characteristics

In order to make sure the removal of CO_2 from the powder mixture is complete, apart from the calcination process, the green $Ba_5Nb_4O_{15}$ powder compact was kept at 1000°C for 2.5 h. The specimens then fired to the sintering temperatures. Moreover, the XRD analysis detects no residual starting material in the sintered specimens. Only $Ba_5Nb_4O_{15}$ phase was found in the calcined powder. For each experimental condition, at least 10 specimens were prepared for increasing statistical accuracy. The error bar in the figures shows ± 3 standard deviations. In addition to compare the weight loss characteristics of $Ba_5Nb_4O_{15}$, Nb_2O_5 raw material is also granulated to be formed as reference samples.

Figure 3-3 shows the TGA curve for the powder mixtures of $BaCO_3$ and Nb_2O_5 as a function of temperature. The curve indicates that the decomposition of $BaCO_3$ starts from a temperature above 600°C, finishes around 900°C. The $BaCO_3$ is decomposed completely to form BaO at a temperature above 900°C. Finally, a temperature of 1000°C is then chosen as the calcination temperature for the preparation of $Ba_5Nb_4O_{15}$ phase. The powder morphology of $Ba_5Nb_4O_{15}$ products appear wide distribution examined by SEM in Fig. 3-4 (a). The particles exhibit a bimodal size distribution; the mean particle size is 2.3 μm as determined with the particle size analyzer. Fig. 3-4 (b).

Figure 3-5 shows the weight loss for the sintered $Ba_5Nb_4O_{15}$ specimens at the indicated temperatures for 2.5 h. The weight loss for the Nb_2O_5 specimens is also shown for comparison purpose. The $Ba_5Nb_4O_{15}$ specimen starts to decrease its weight above 1350°C. This weight loss corresponds closely to a density drop shown in Fig. 3-6. As the sintering temperature increases to 1435°C, the weight loss reaches 0.35%, the density decreases seriously to 82 %. For comparison

doi:10.6342/NTU201702760

purpose, the weight loss for the Nb_2O_5 specimens is also monitored; its weight loss during sintering is negligible.

A weight loss is obviously noted for the $Ba_5Nb_4O_{15}$ specimen after sintering above 1350°C. It can be considered as some substance will be gasified to evaporate out of condensed solid and generate pores inside. This weight loss method indirectly indicates $Ba_5Nb_4O_{15}$ ceramics as the evidence for the formation of volatile substance at those evaluated temperature. The volatile contents will leave out of ceramic body especially $Ba_5Nb_4O_{15}$ released much more than Nb_2O_5. The trend of loss weight is getting to worse at higher temperature.

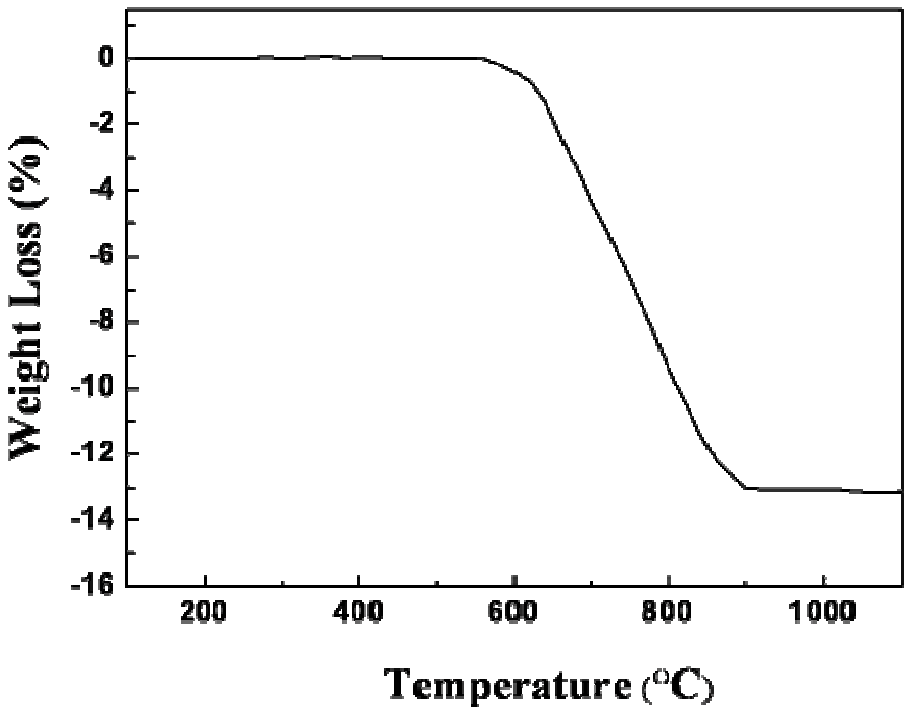

Fig. 3-3 TGA curve for the powder mixture of $BaCO_3$ and Nb_2O_5 as a function of temperature. The heating rate was 5 °C/min.

doi:10.6342/NTU201702760

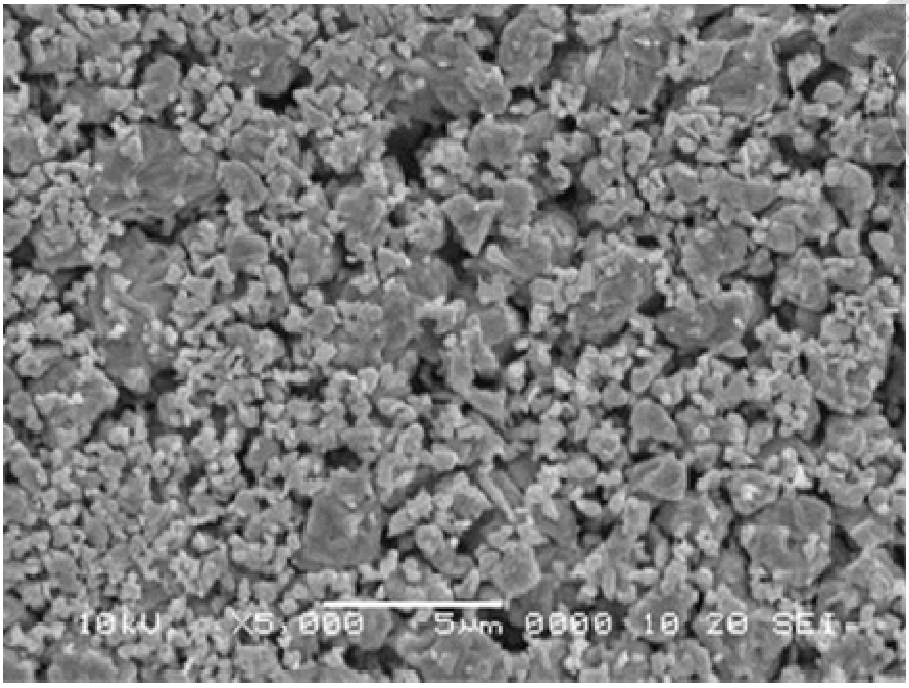

Fig. 3-4 (a) Morphology of the $Ba_5Nb_4O_{15}$ powder prepared by calcination at 1000°C.

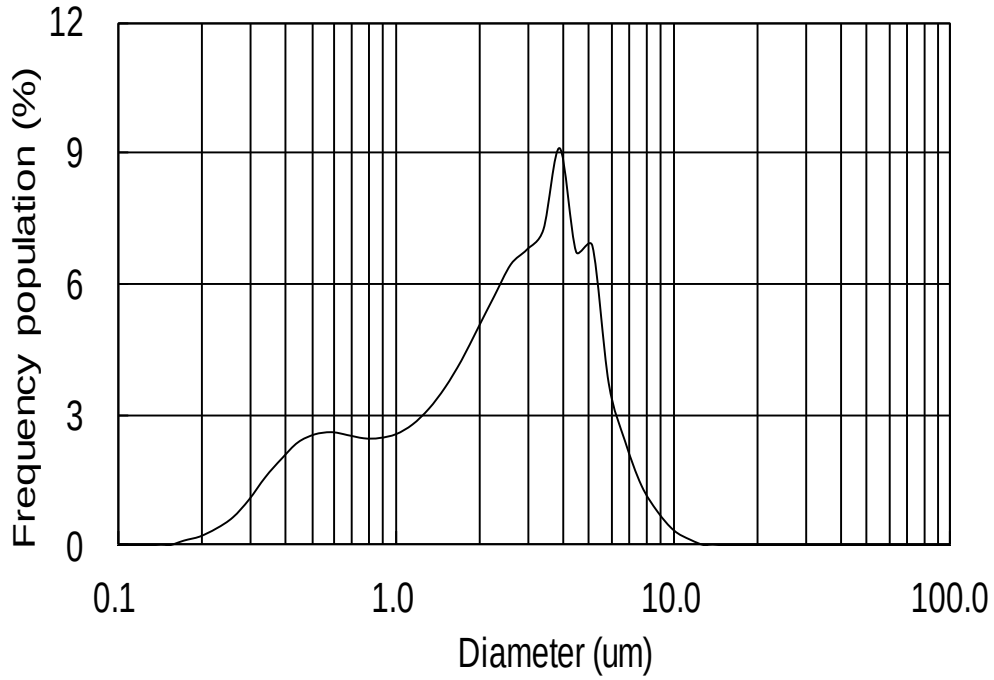

Fig. 3-4 (b) Particle size distribution of pulverized $Ba_5Nb_4O_{15}$ powders.

doi:10.6342/NTU201702760

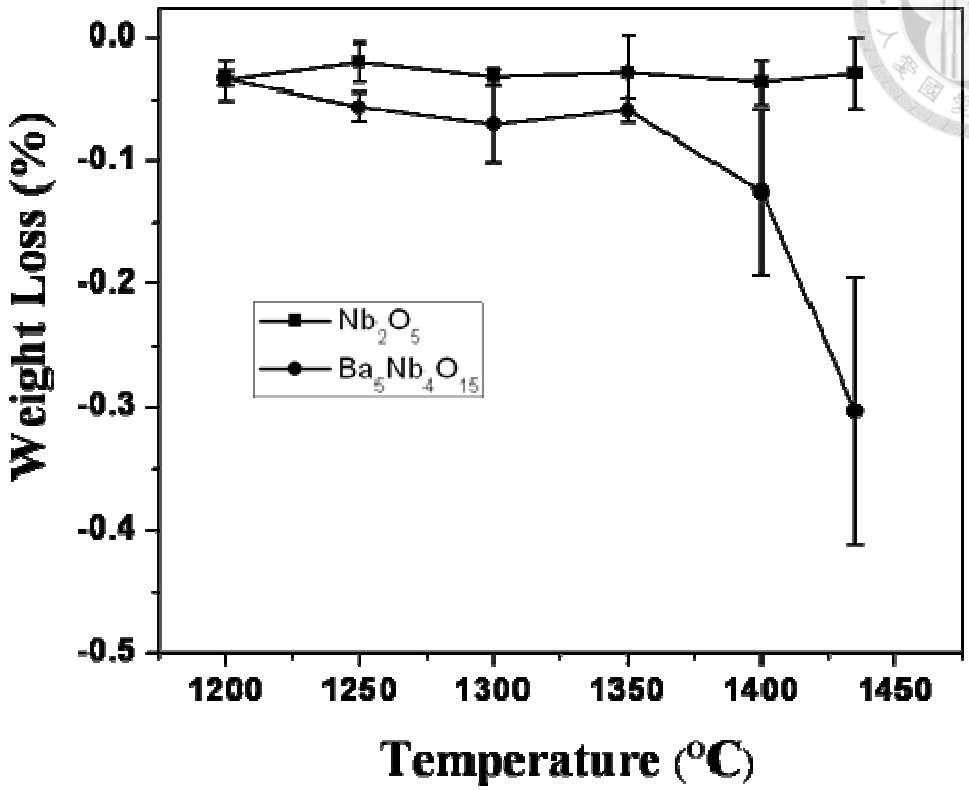

Fig. 3-5 Weight loss of $Ba_5Nb_4O_{15}$ specimens as a function of sintering temperature.

The weight loss of Nb_2O_5 specimens is also shown for comparison.

doi:10.6342/NTU201702760

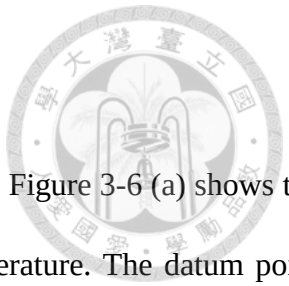

3.3.2 Sintering density degradation

Definitely weight loss causes to be low density of sintered $Ba_5Nb_4O_{15}$. Figure 3-6 (a) shows the relative density for the sintered specimen as a function of sintering temperature. The datum point shows the average value for 10 specimens, the error bars show ± 3 standard deviations. In general statement, the final stage densification curve of sintered body is nearly keeping at certain high relative density. It began when most of pores are closed and isolated. The mass of solid must be transported into pore and proceeds its shrinkage. The volume of ceramic body will decrease. But on the contrary, the sintered density curve of $Ba_5Nb_4O_{15}$ reaches its highest value, 93%, at the sintering temperature of 1250°C. The density starts to decrease from 1300°C; it is only 82% after sintering at 1435°C. The so-call degradation of sintered density at evaluated temperature higher than 1250°C can meet in coincidence tendency of weight loss experiment. For Nb_2O_5 samples, there is no markedly degradation of density at relative temperature.

Another approach on dimension of sintered specimen gives the evidence of density degradation of $Ba_5Nb_4O_{15}$. The shrinkage rate of radial and axial direction has near the same tendency as abnormal grain growth. The shrinkage rate reaches its highest level at 1250°C in Fig. 3-6 (b). The volume of ceramic body occurs to expand in all direction. When grain boundary moves fast and pores were closed and trapped in grain. It will likely be found from microstructure observation.

doi:10.6342/NTU201702760

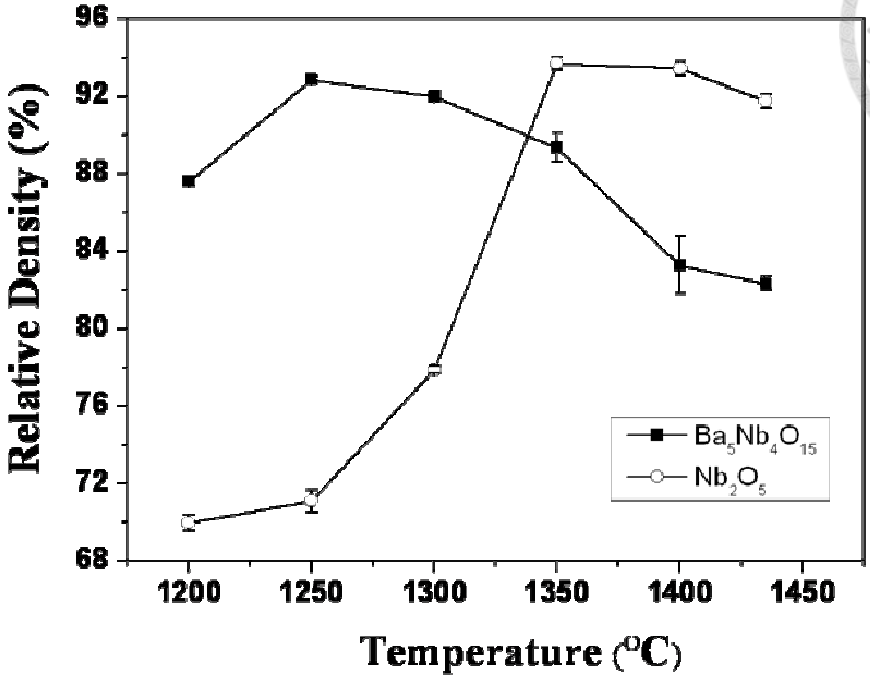

Fig. 3-6 (a) Relative density of $Ba_5Nb_4O_{15}$ specimens as a function of sintering temperature.

The density of Nb_2O_5 specimens is also shown for comparison.

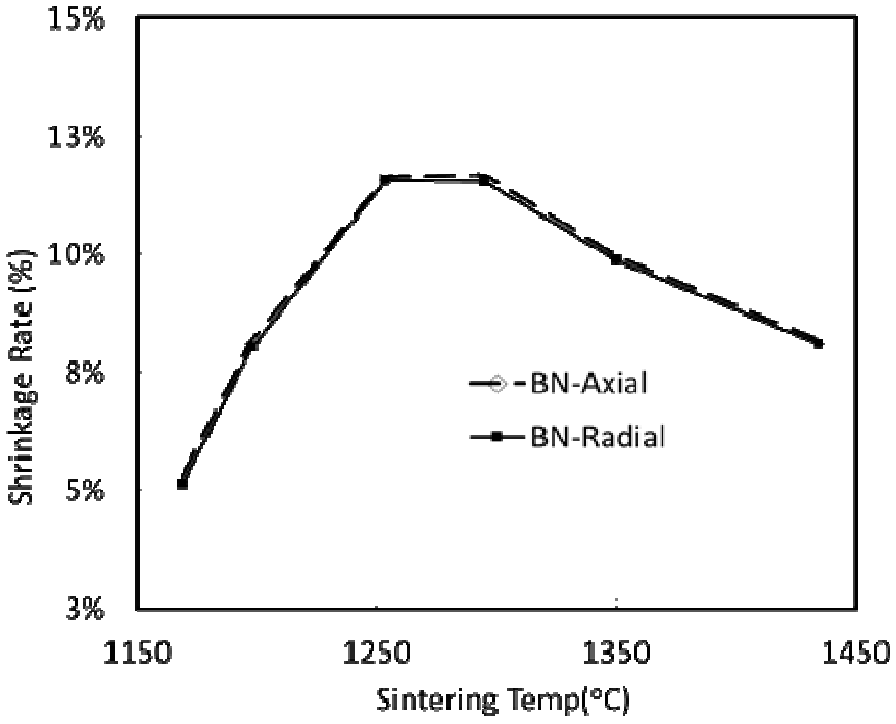

Fig. 3-6 (b) The shrinkage rate of $Ba_5Nb_4O_{15}$ specimens as a function of sintering temperature.

doi:10.6342/NTU201702760

3.3.3 Microstructure and X-ray diffraction

To look for $Ba_5Nb_4O_{15}$ fundamentally grain growth mechanism at different temperatures, the investigation on grains and pores morphology should be confirmed at inner of sintered ceramic body. Microstructure of ceramic body was examined by cross section with polishing and thermal etching treatment. The way used to inspect anisotropic grains and pore's growth from comparing different heat works. At the same time, a large amount of pore homogeneously distributed in sintered specimen. It starts on 1200ºC but will annihilate to grow hugely. They were complied with grain growth when sintering temperature increase. It also shows the evidence of numerously spherical pores isolated in the grain after grain boundary dragging out of the pores.

Figure 3-7 shows the free surface micrographs for the sintered $Ba_5Nb_4O_{15}$ specimen at different temperature. The anisotropic grains are evidently growing as longitudinal shape. It is not parabolic growth which rely on the curvature or surface tension of grain. The shape of grain can be defined to aspect ratio of length to width L/D. When sinter at higher temperature, the aspect ratio will change into smaller one and grain area increase dramatically. The grain boundary movement is fast and higher than pores that are all trapped inside of ceramic body.

The polished sections for the specimens sintered at 1250°C to 1435°C are shown in Fig. 3-8 and Fig. 3-9, respectively. These two specimens were thermally etched at 1200°C to reveal the grain boundaries. After sintering at 1250°C, the $Ba_5Nb_4O_{15}$ grains are no longer equiaxed. The length of the $Ba_5Nb_4O_{15}$ grains is longer than 10um. The size of $Ba_5Nb_4O_{15}$ grains increases with the increase of sintering temperature. Apart from the pores at the triple junctions, many isolated pores are found within $Ba_5Nb_4O_{15}$ grains. The strength of the specimens sintered above 1350°C is very low. Many pull-outs were observed during the grinding and polishing stages. It is thus not possible to present the micrographs for the polished sections of the specimens sintered above 1350°C. The fracture

doi:10.6342/NTU201702760

surfaces for the specimens sintered at 1250°C to 1435°C are shown instead in Fig. 3-10 and Fig. 3-11, respectively. On the fracture surface, both spherical pores within the grains and large pores at the corners of the grains are observed. Even though the grain growth rate is higher than pore mobility, the corner pores coalesced and grew up along grain boundary. The trapped pores will vanish or become spherical shape due to mass transport into the void by volume diffusion.

doi:10.6342/NTU201702760

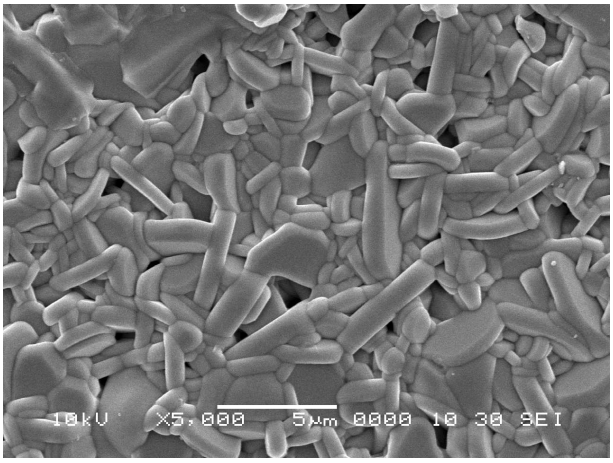

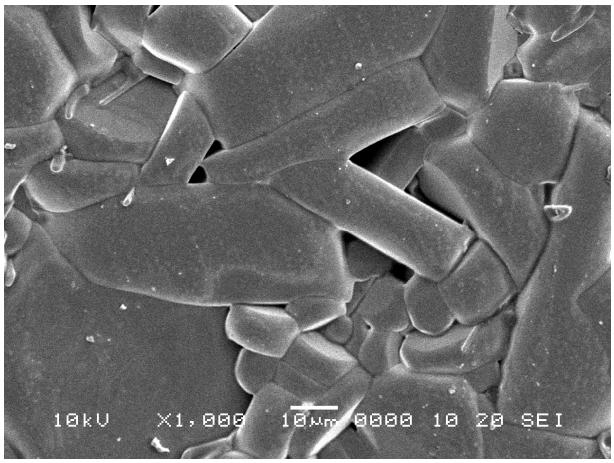

Fig. 3-7 Typical free surface micrographs of $Ba_5Nb_4O_{15}$ specimens sintered at (a) 1250°C (b) 1300°C (c) 1435°C

doi:10.6342/NTU201702760

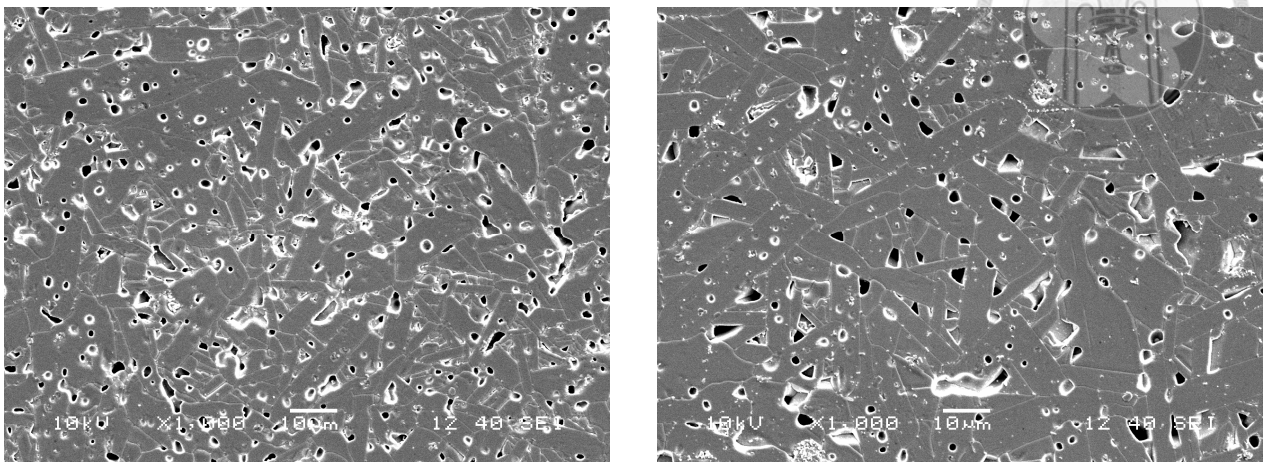

(a) (b)

Fig. 3-8 Typical polished sections micrographs of $Ba_5Nb_4O_{15}$ specimens sintered at

(a) 1250°C (b) 1300°C

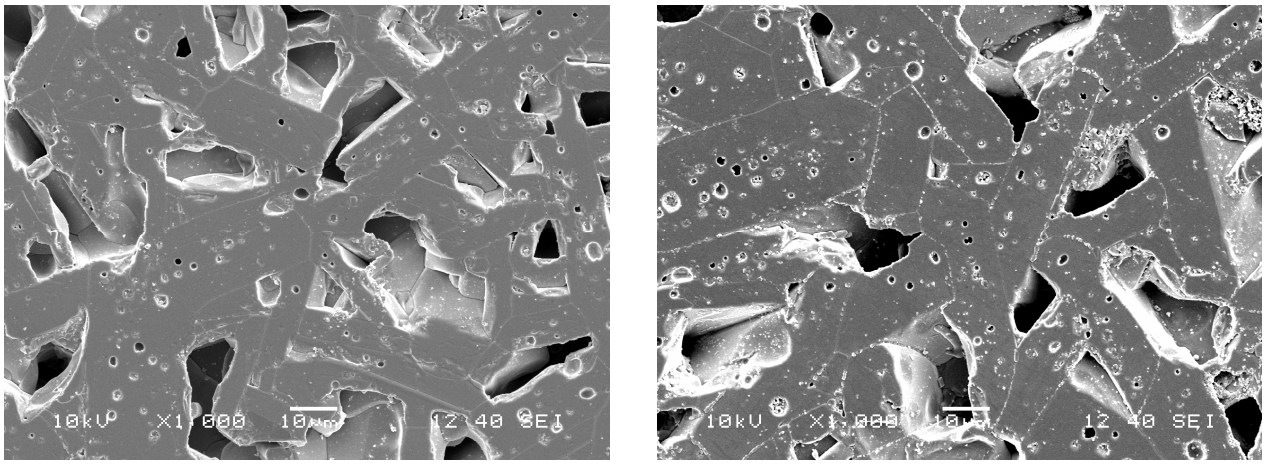

(a) (b)

Fig. 3-9 Typical polished sections micrographs of $Ba_5Nb_4O_{15}$ specimens sintered at

(a) 1350°C (b) 1435°C

doi:10.6342/NTU201702760

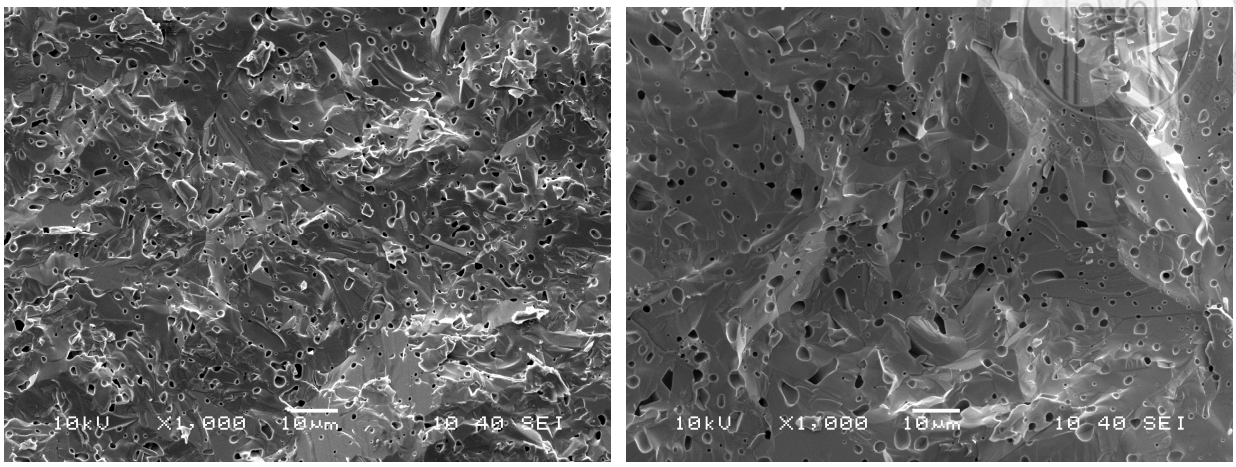

(a) (b)

Fig. 3-10 Typical fracture surfaces micrographs of $Ba_5Nb_4O_{15}$ specimens sintered at

(a) 1250°C (b) 1300°C

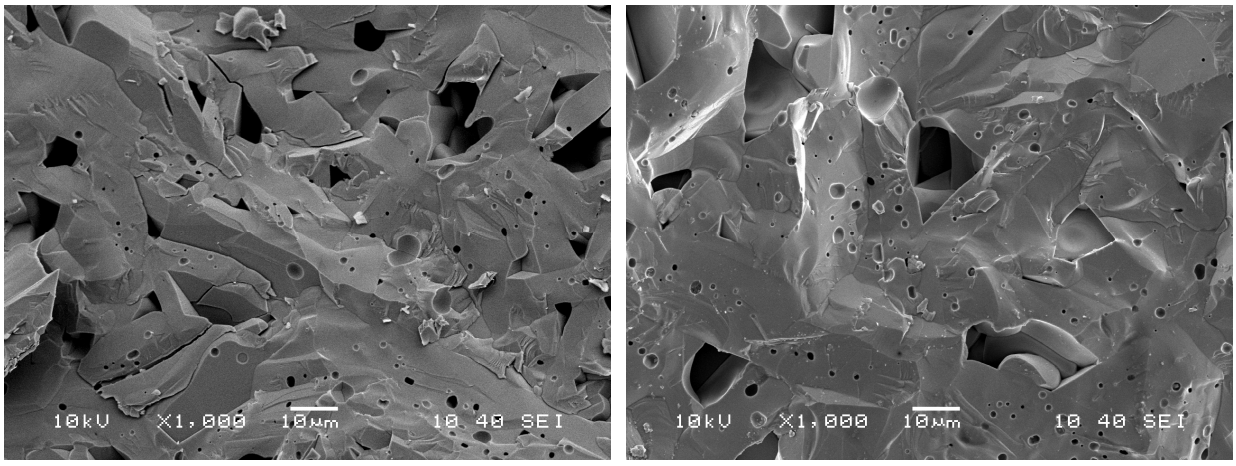

(a) (b)

Fig. 3-11 Typical fracture surfaces micrographs of $Ba_5Nb_4O_{15}$ specimens sintered at

(a) 1350°C (b) 1435°C

doi:10.6342/NTU201702760

To verify the anisotropic grain growth may be derived by liquid phase, Figure 3-12 (a)&(b) shows a high resolution TEM micrograph for the specimen sintered at 1350°C. An amorphous phase is found at the grain boundary, FFT (Fast Fourier Transform) images show the diffraction pattern on both regions of grain and boundary area. The thickness of the amorphous phase is around 10 nm. There is small amount of SiO_2 impurity was detected by EDS of HR-TEM.

The trapped pores were also observed at different sintering temperature with bright field image. Fig. 3-12 (c) to (e). Many voids were along with parallel direction that may comment to easily happen at certain crystal planes. The evidence of pores illustrated not only by packing of powders at sintering stage but also generated from some evaporation from substance of $Ba_5Nb_4O_{15}$.

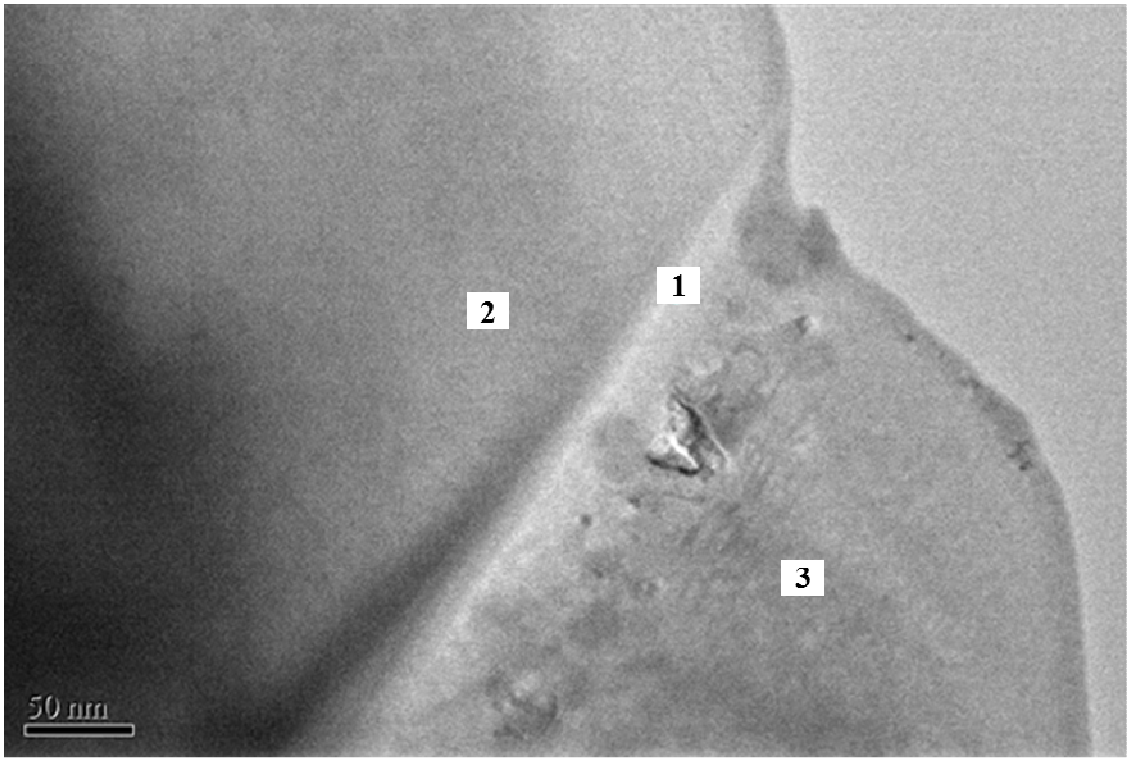

Fig. 3-12 (a) TEM micrograph of $Ba_5Nb_4O_{15}$ sintered at 1350 °C. The bright field image of grain (area 2,3) and grain boundary (area 1)

doi:10.6342/NTU201702760

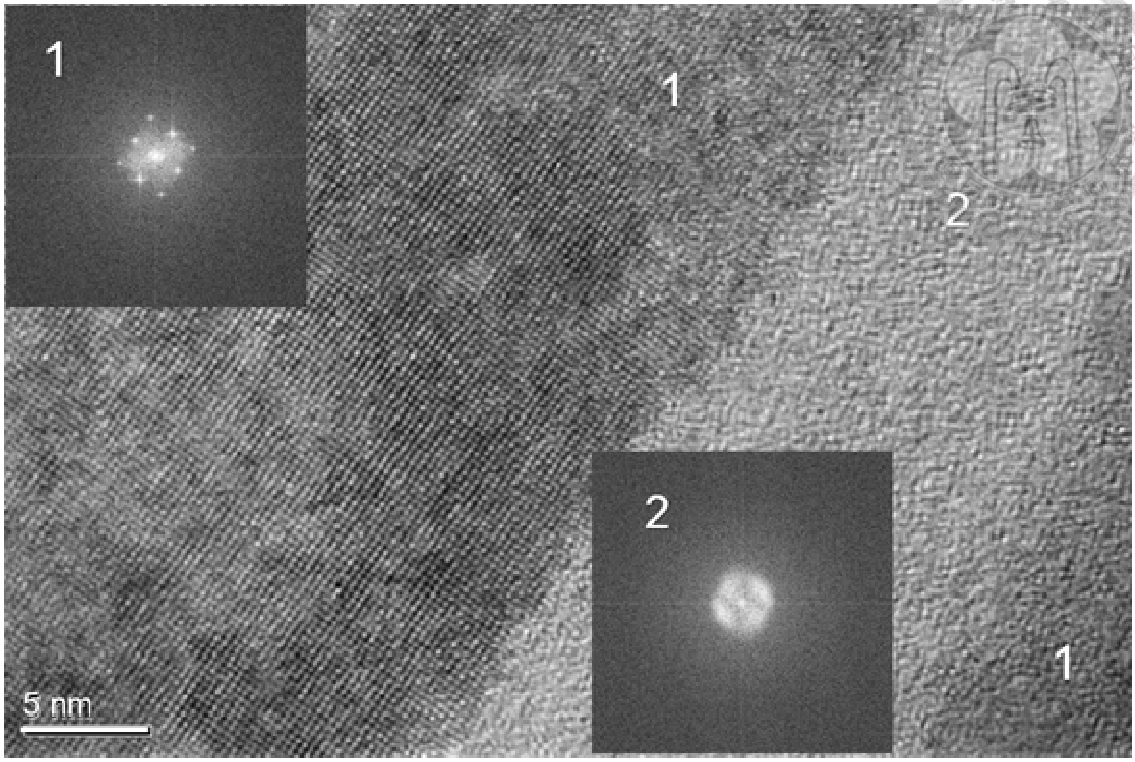

Fig. 3-12 (b) TEM micrograph of $Ba_5Nb_4O_{15}$ sintered at 1350 °C. The diffraction patterns for grain (area 1) and grain boundary (area 2) are shown in the inset.

Table 3-2 HRTEM-EDX for grain area 1 and grain boundary area 2

wt(%)	Area 1	Area 2
O K	14.3	16.8
Al K	0.0	0.6
Si K	0.1	1.3
Nb K	27.6	26.1
Ba K	58.0	55.2

doi:10.6342/NTU201702760

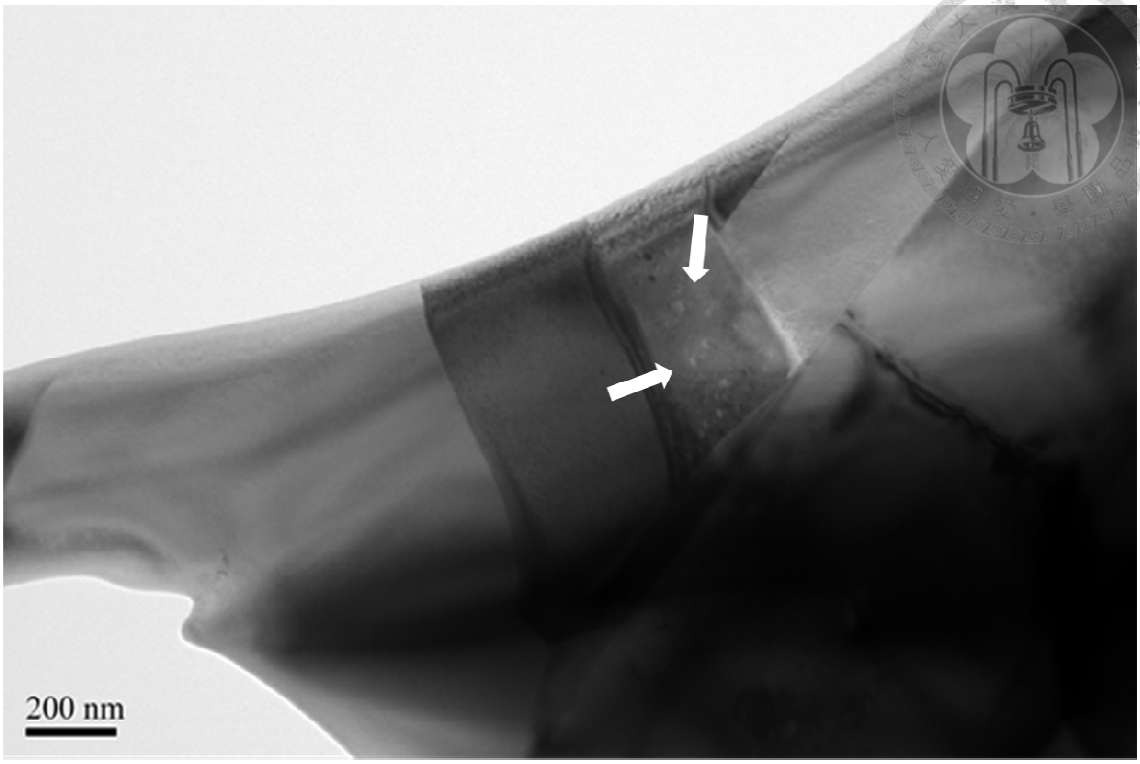

Fig. 3-12 (c) TEM micrograph of $Ba_5Nb_4O_{15}$ sintered at 1350 °C. Trapped pores are observed in the grain (white arrow).

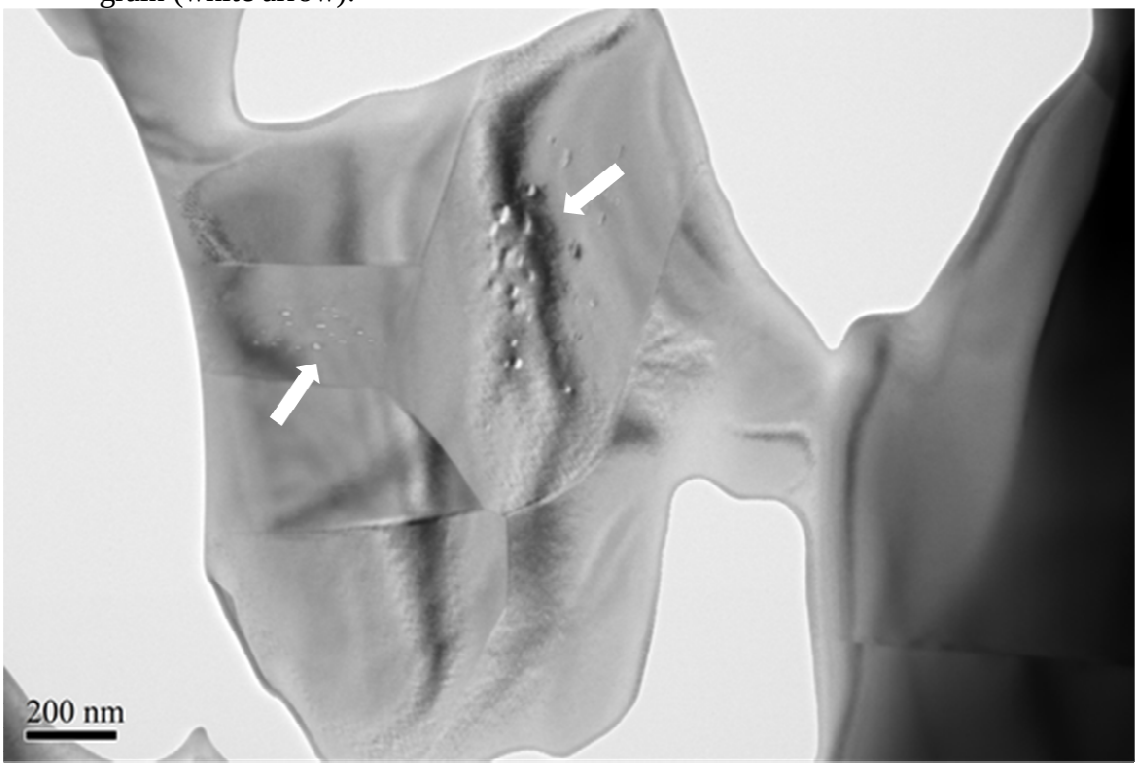

Fig. 3-12 (d) TEM micrograph of $Ba_5Nb_4O_{15}$ sintered at 1435°C. Trapped pores are observed in the grain (white arrow).

doi:10.6342/NTU201702760

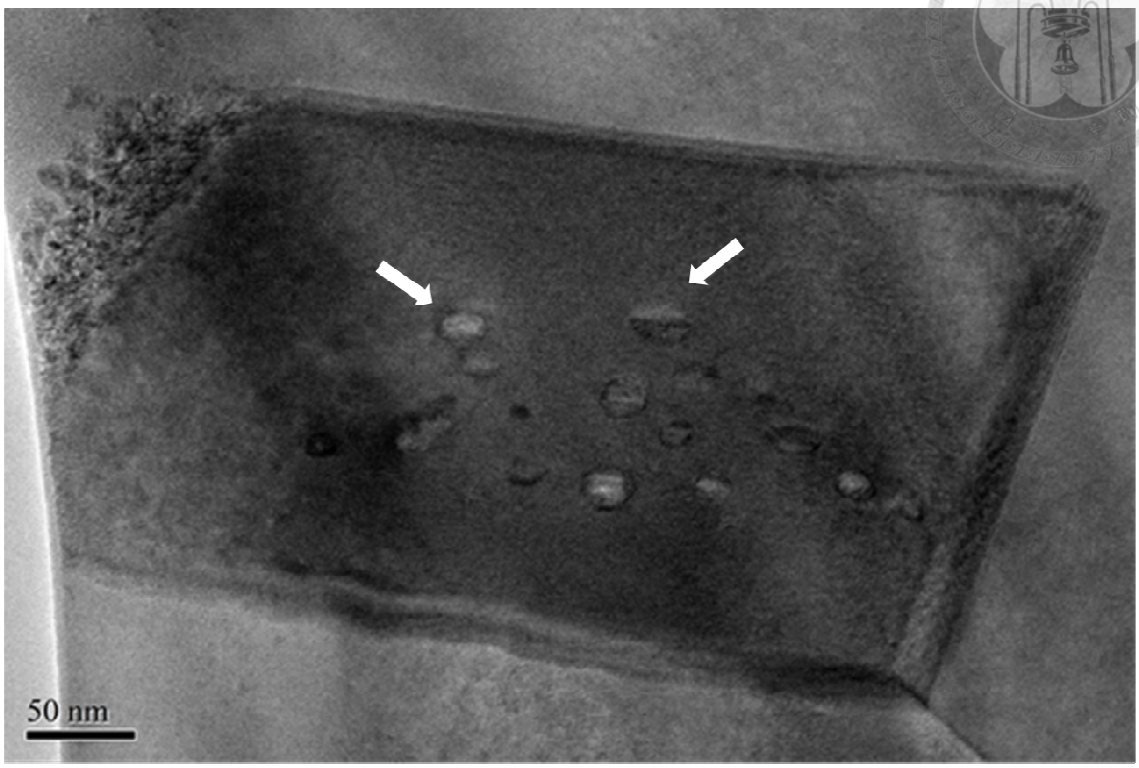

Figure 3-12 (e) TEM micrograph of $Ba_5Nb_4O_{15}$ sintered at 1435°C. Trapped pores are observed in the grain. (white arrow)

Only one crystalline phase, $Ba_5Nb_4O_{15}$ perovskite, is found for the calcined powder. The XRD patterns for the sintered specimens are also shown in Fig. 3-13. The XRD patterns for the sintered specimens are also shown in figure with different sintering temperature. It is similar to the calcined powder and no second phase detected. Using the peak for silica as the external standard, the shift for the $Ba_5Nb_4O_{15}$ peaks is very small after sintering. All diffraction peaks of 2θ angles in the range of 25~70° were identified by Rietveld refinement method. The constructive interference of

doi:10.6342/NTU201702760

monochromatic X-ray reflects the highest intensity peaks at planes (0 1 3) and (1 1 0). Using the peak for silica as the external standard, the shift for the XRD peaks is very small after sintering. Taking the (013) peak as the example, its 2θ shifts only 0.015 degree after sintering temperature increases from room temperature to 1435°C.

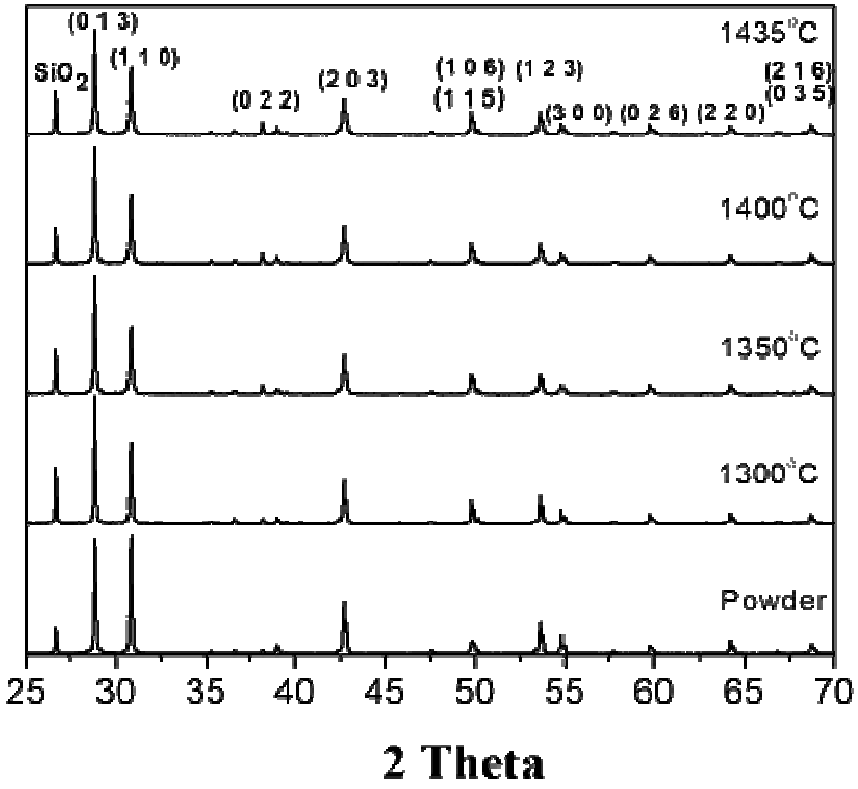

Fig. 3-13 XRD patterns for 2θ from 25° to 70° of the $Ba_5Nb_4O_{15}$ powder and sintered specimens. SiO_2 was added as the external standard.

doi:10.6342/NTU201702760

Apart from diffraction pattern at low angle side, a high resolution with increasing step scan and sweep time at high angle of 115~125° can distinguish the phase plane of sintered $Ba_5Nb_4O_{15}$ in Fig.3-14. A distinct plane at angle of 119.5° shows the intensity of peak increase in correspondence with sintering temperature. Here high index plane presents its higher surface enthalpy that need working energy to move plane satisfying long range ordering of crystal structure[50-51]. The high index plane ordering structure is always related to microwave characteristic such as quality factor. Another direct evidence in lattice images studying, a super high Q dielectric material exhibits its ordering structure proved by HRTEM analysis[52]. The quality factor of $Ba_5Nb_4O_{15}$ will be considered about lattice ordering structure later.

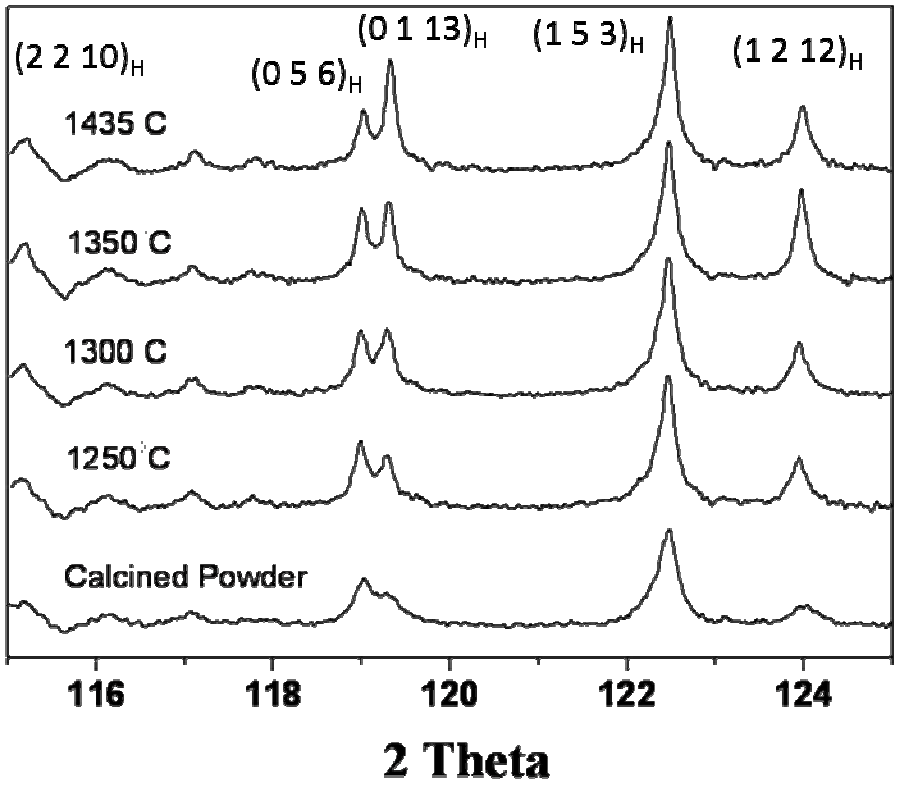

Fig. 3-14 XRD patterns for 2θ from 115° to 125° of the $Ba_5Nb_4O_{15}$

doi:10.6342/NTU201702760

3.3.4 XPS

XPS measurement on different sintered temperature $Ba_5Nb_4O_{15}$ ceramic surface results the spectra shift of Nb 3d orbital electron binding energy in Fig 3-15 (a). A spin-orbit splitting peaks exhibit two 3/2 and 5/2 quantum states of niobium 3d electron angular momentum energy. Sample sintered at 1300^{o}C exhibit binding energy position 209.85eV then slightly shifted to 209.55eV when sintered at 1350^{o}C. Finally, sample sintered at 1435^{o}C reveal partial of valence electrons has a clear chemical shift to 203.25eV that takes the advantage of the fact determined the reduction of niobium element[53]. After sintering at 1435°C, the Nb peaks shift by ~ 6 eV, indicating that the reduction from Nb^{5+} to Nb^{4+} or more low state is taken place. The XPS spectrum of oxygen atoms for the $Ba_5Nb_4O_{15}$ specimens after sintering is also shown in Fig. 3-15 (b). Obviously 1s state binding energy of oxygen is same as 3d state of niobium atom has a chemical shift at 1435°C. For Nb 3d, both Nb $3d_{3/2}$ and Nb $3d_{5/2}$ peaks are observed. The O1s peaks remain at the same binding energy for the specimen sintered at 1300°C and 1350°C. After sintering at 1435°C, the O peaks shift by ~ 6 eV, indicating that the reduction from Nb^{5+} to Nb^{4+} or more low state is taken place[54-55].

doi:10.6342/NTU201702760

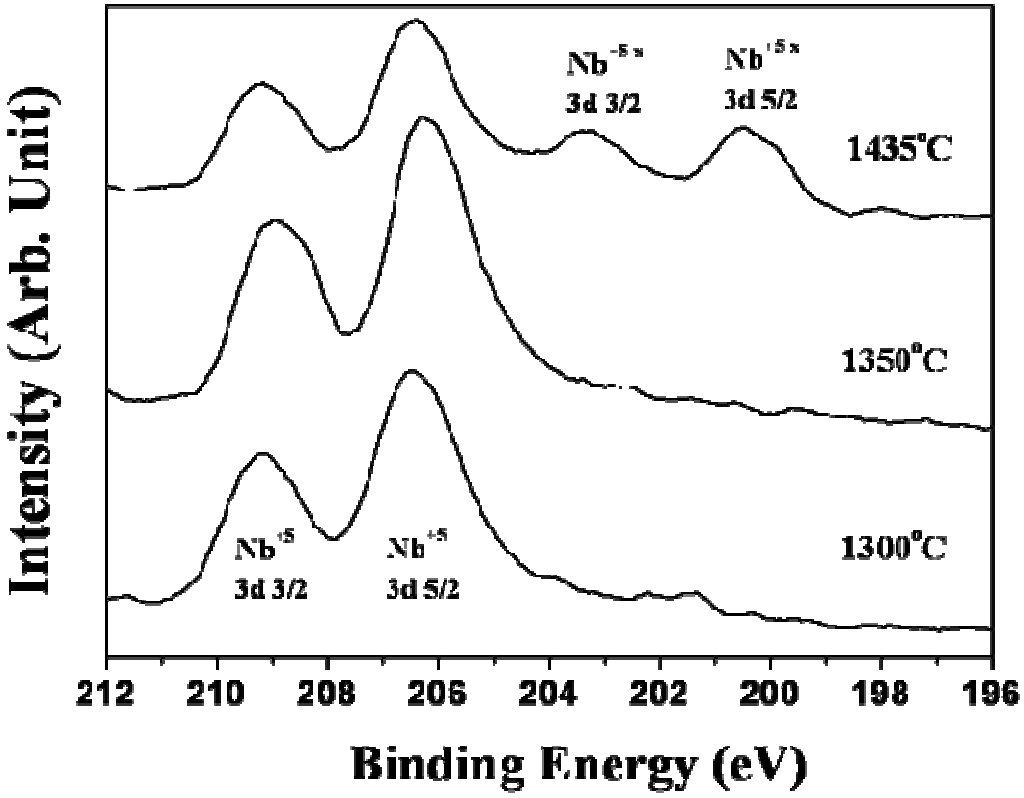

Fig. 3-15 (a) XPS Nb 3d binding energy spectra for sintered $Ba_5Nb_4O_{15}$ specimens

doi:10.6342/NTU201702760

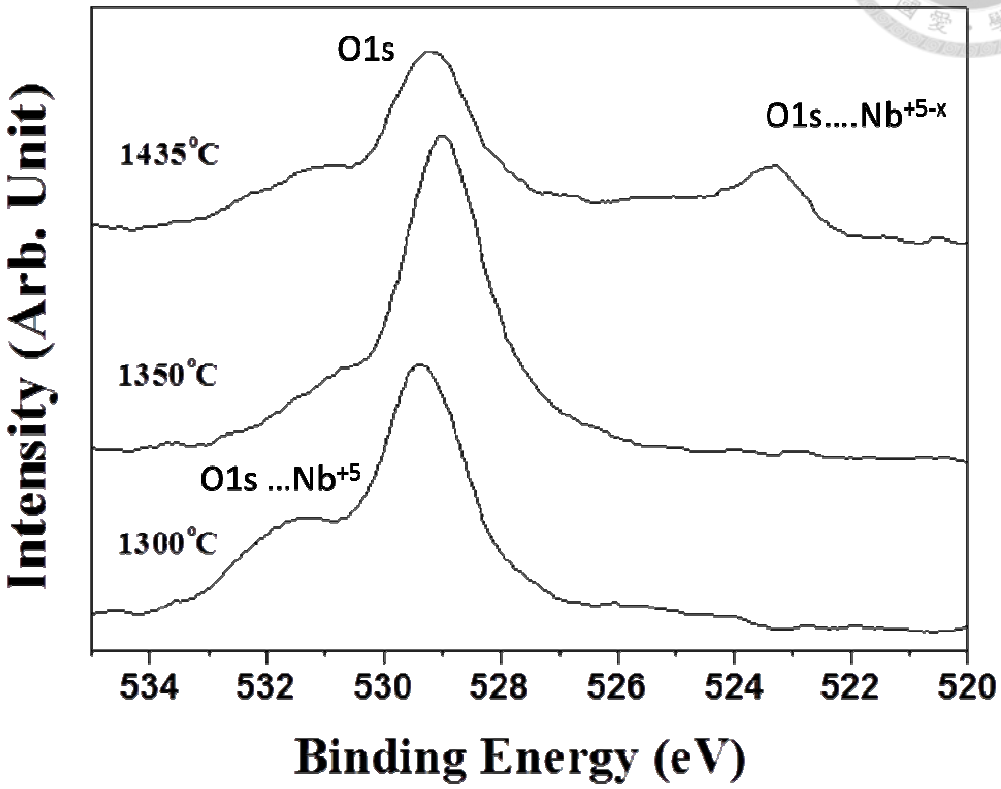

Fig. 3-15 (b) XPS O1s binding energy spectra for sintered $Ba_5Nb_4O_{15}$ specimens

doi:10.6342/NTU201702760

3.3.5 Microwave property

The permittivity of $Ba_5Nb_4O_{15}$ ceramics were relevant with density which presented from 32.8 to 37.8. Figure 3-16 (a) shows the microwave characteristics of the sintered $Ba_5Nb_4O_{15}$ specimen. The highest permittivity reaches 38 after sintering at 1250°C, then decreases its value to 33 as the sintering temperature is 1435°C. Strongly relevant tendency between permittivity and relative density reveals the porosity of $Ba_5Nb_4O_{15}$ has linearity influence on polarization. The permittivity can be derived from the relative density of $Ba_5Nb_4O_{15}$ directly. Quality factor Q×*f* value has also the tendency to sintered density of $Ba_5Nb_4O_{15}$ in Fig 3-16 (b) but reverses to lower when density degradation. No doubt the quality factor will decrease when ceramic porosity affects resonated electromagnetic wave cause to energy loss. In contrast to porosity effect on higher sintering temperature, the quality factor jumps to a value > 40,000 when increasing temperature over 1400°C. The trend of quality factor with relative density has never been found out before[6]. The investigation on high quality factor at high porosity of $Ba_5Nb_4O_{15}$ is the interests of this study.

doi:10.6342/NTU201702760

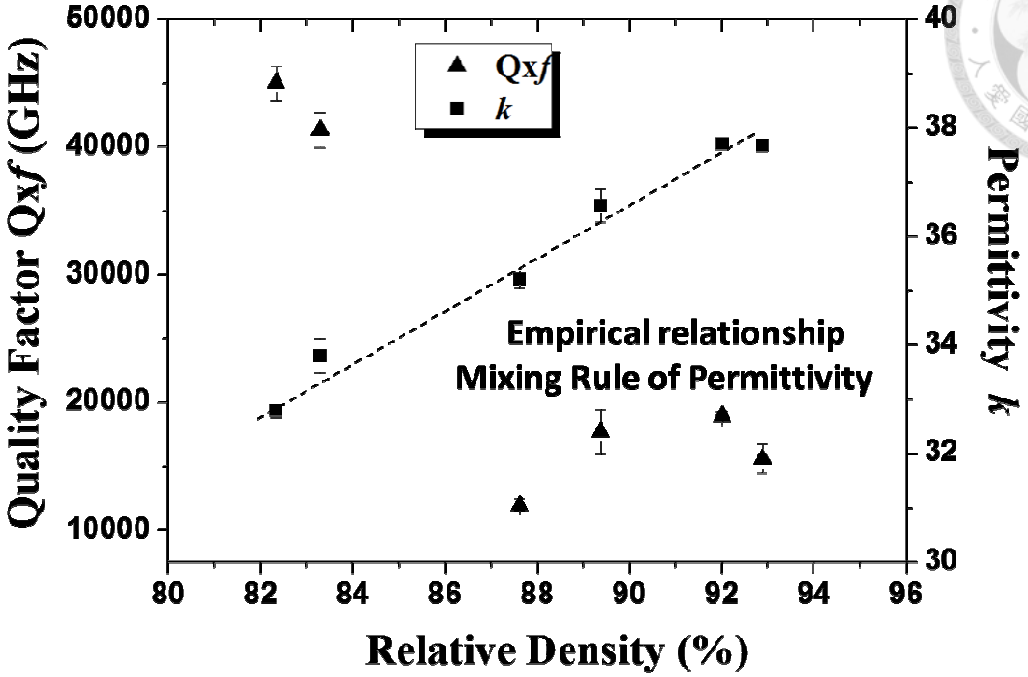

Fig. 3-16 (a) Dielectric constant and quality factor for $Ba_5Nb_4O_{15}$ specimen as a function of relative density.

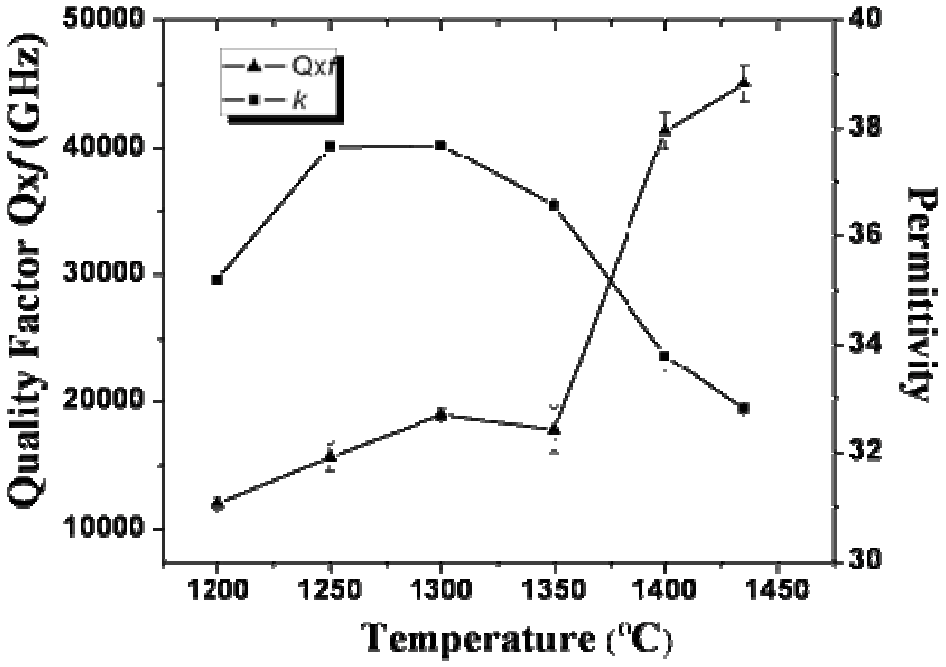

Fig 3-16 (b) Dielectric constant and quality factor for $Ba_5Nb_4O_{15}$ specimen as a function of sintering temperature.

doi:10.6342/NTU201702760

3.4 Discussions

3.4.1 De-sintering phenomena

The present study demonstrates that the densification of $Ba_5Nb_4O_{15}$ microwave ceramic is challenging. However, to the surprise of the present authors, the problem has seldom been addressed. The de-sintering at a temperature higher than 1250°C has never been carefully investigated. The present study is the first one addressing this important issue. It is obviously de-sintering phenomena happened at higher temperature and the samples size expanded when sinter over 1300°C. Abnormal grain growth always occurs at $A_5B_4O_{15}$ hexagonal perovskite material system[56-57]. Contrary to sintered density reveal the pores will not be annihilated but increased volume when temperature is over 1300°C. There are many rectangular like pores with 10~50um size distributed hugely along grain boundary. From energy point of views, it goes against sintering mechanism, pores trapped in grain or triple point of boundary at final stage. A temperature of 1000°C was used to synthesis the $Ba_5Nb_4O_{15}$ powder. The density of the $Ba_5Nb_4O_{15}$ specimen reaches its highest value of 93% after sintering at 1250°C. A weight loss is noted above 1350°C, it corresponds to a rapid density decrease. After sintering at 1435°C for 2.5h, the density is only 82%.

Sintering process usually involves the increase of density and the growth of grains. The density increase is a densification process that consumes the surface area; the grain growth is a coarsening process that reduces the area of grain boundary. The reduction of surface area and of grain boundary area contributes to the driving force of sintering[58]. The densification and coarsening are thus taken place simultaneously during sintering. Though density is usually increased with the increase of temperature; occasionally, a density decreases with the increase of sintering temperature or dwell time, usually termed as de-sintering, is observed for the present $Ba_5Nb_4O_{15}$ specimen. Such de-sintering can be related to two possible reasons. The first one is contributed by the coarsening of

doi:10.6342/NTU201702760

pores and the second one by the generation of volatile substance.

In the present study, the $Ba_5Nb_4O_{15}$ specimens are sintered in air. The air is entrapped within the pores as the specimen reaches its final stage of sintering. The coarsening of grains and pores can be found with the increase of sintering temperature Fig. 3-8~11. A density decrease may be accompanied with the coarsening of pores, due to that the collapses of two pores together resulting in a larger pore volume, as demonstrated in the Appendix.

The shape of starting $Ba_5Nb_4O_{15}$ particles is angular, as resulted from the grinding process used in the present study. The growth of $Ba_5Nb_4O_{15}$ grains is noted after sintering above 1250°C, Fig. 3-7. In the figure, the $Ba_5Nb_4O_{15}$ grains are no longer equiaxed, they are elongated in shape. The length of $Ba_5Nb_4O_{15}$ grains can reach a value larger than 10μm after sintering above 1250°C. The formation of elongated grains has been related to the presence of a liquid phase at grain boundary[59-60]. The amorphous phase found by TEM in the present study Fig. 3-12 is a liquid phase at elevated temperatures. The EDX analysis detects the presence of aluminum and silicon at the liquid phase. Though the purity of the starting powders is higher than 99.9%, a small amount of impurities produces a liquid phase at elevated temperature. Due to the anisotropic crystalline structure of $Ba_5Nb_4O_{15}$ perovskite, the growth of each crystalline direction is not the same[61], especially in the presence of a liquid phase. The $Ba_5Nb_4O_{15}$ grains with elongated shape are thus formed after sintering.

More importantly, many isolated pores are found within the grains after sintering above 1250°C. It suggests that the separation of grain boundary and pores is taken place during sintering, a typical phenomenon found for the abnormal grain growth. As the abnormal gain growth is started at 1250°C, the densification is prohibited. No density increase is thus observed above this temperature. From microstructure observation, the coarsening of pores is also observed. The de-sintering can thus

doi:10.6342/NTU201702760

be related to such coarsening process, at least partly. However, the coarsening of pores involves no weight loss. In the temperature range from 1250°C to 1350°C, the weight loss is minor. The de-sintering within this temperature range is mainly contributed by the coarsening of microstructure.

3.4.2 Reduction of $Ba_5Nb_4O_{15}$

Many possible routes generate gas phase from $Ba_5Nb_4O_{15}$ reaction formula such as volatility, ionic oxidation state change and or defect chemistry. There are two formulas demonstrate the niobium ionic oxidation state change can be illustrated possibly as:

$$Nb_2O_5(s) \rightarrow Nb_2O_{5-x}(s) + x/2O_2(g) \qquad (3.1)$$

$$Ba_5Nb_4O_{15}(s) \rightarrow Ba_5Nb_4O_{15-y}(s) + y/2O_2(g) \qquad (3.2)$$

Using the molar equation calculation, the x and y are mole equivalent of dissociating oxygen atoms theoretically which illustrate with different niobium ionic oxidation state. When sintering temperature run higher generate gas phase O_2 that niobium ionic oxidation state gradually increases in accordance with sintering temperature. Principle of conservation of mass for Nb_2O_5 theoretically convert oxidation in integer state has 6.0~18.0wt% loss and $Ba_5Nb_4O_{15}$ 1.23~3.70wt% weight loss by calculation. $Ba_5Nb_4O_{15}$ ceramics measure 0.35wt% loss convert to equivalent y mole of oxygen product is around 0.28 at 1435°C. It reveals $Ba_5Nb_4O_{15}$ material drastically dissociate oxygen atoms

doi:10.6342/NTU201702760

than Nb_2O_5 which examined by weight loss experiment. Therefore, the binding energy of oxygen atom with niobium atom occurs in $Ba_5Nb_4O_{15}$ is much lower than Nb_2O_5.

There are many reports on binding energy of different niobium oxidation state, all of evidences on chemical shift to lower energy prove high valence state changed to low valence state[62]. Basically, $Ba_5Nb_4O_{15}$ ceramic exhibit oxygen dissociated when niobium valence state change from +5 to +4 or +3. It can be referred to equation (3.1) that oxygen gas out of solid happened by temperature driving energy. More energy from sinter temperature and more dissociated oxygen happened at $Ba_5Nb_4O_{15}$ ceramic body. From microstructure of sintered ceramic, the gas phase generated by combined oxygen atom diffused into grain boundary and enlarge the volume of closed pores. Most of oxygen gas were trapped into the closed pores that along the grain boundary or isolated into grain.

There are many oxidation states for transition metals. The oxidation states for metallic niobium can be Nb^{5+} and Nb^{+5-x}. The Nb_2O_5 is the most stable oxide at low temperatures. The XPS analysis, Fig. 3-15 (a), demonstrates the shift of Nb $3d_{3/2}$ and Nb $3d_{5/2}$ peaks by ~6 eV after sintering temperature increases from 1300°C to 1435°C. It suggests the formation of Nb^{+5-x}. The formation of Nb^{+5-x} is accompanied with the release of oxygen gas, as demonstrated in the following reaction (3.3)

$$Ba_5Nb_4O_{15} \xrightarrow{>1350^\circ C} Ba_5Nb_4O_{15-x} + \frac{x}{2}O_2 \qquad (3.3)$$

The weight loss for Nb_2O_5 specimen at elevated temperatures is negligible Fig.3-5. It suggests that the reduction of Nb ions depends on their chemical environment. The $Ba_5Nb_4O_{15}$ perovskite is composing of NbO_6 octahedra and BaO_{12} dodecahedra lattice structure, which is different from that in Nb_2O_5. Such difference results in difference in the reduction capability for Nb ions. From

doi:10.6342/NTU201702760

semi-quantitative analysis by deconvolution of peak area, it proved near 40% of niobium reduction state from Nb^{+5} to Nb^{+5-x}. In additional to XPS results of oxygen state Fig. 3-15 (b). $Ba_5Nb_4O_{15}$ exhibits its O1s electron binding energy has chemical shift at 1435°C. The chemical shift of O1s also has 6eV which implies to the bond between oxygen and reduced niobium. This is the evidence of reduction happened to valence electrons transition between the niobium and oxygen atoms simultaneously.

It was found that $Ba_5Nb_4O_{15}$ sintered over 1350°C that all the relative density and microstructure reveal pores generated by oxygen dissociated from the variation on niobium oxidation state. The more driving energy from temperature caused to abundantly oxygen atoms leave out of lattice site and diffuse into gathering pores. anisotropic grain growth. An evidence of $Ba_5Nb_4O_{15}$ de-sintering phenomena was obtained by weight loss measurement. There is 0.35wt% loss at 1435°C when post sinter $Ba_5Nb_4O_{15}$ and Nb_2O_5 have 0% loss. The binding energy of Nb3d and O1s spectra exhibits chemical shift that prove the essential role of niobium atoms contributing the de-sintering property.

doi:10.6342/NTU201702760

3.4.3 Sintering density vs. microwave property

Pamu's study[18] observed the similar trend with relative density as a function of sintering temperature. The reason of dielectric loss still presented to volume of pores that trapped inside ceramic body abundantly. All of pores on the surface eliminated when grains grown in the final sintering stage. The dissociated oxygen can't release out of ceramic body. It is well known that resonated electric energy in the ceramic body that distorted by grain boundary, pores and others extrinsic phases.

The permittivity and quality factor of microwave ceramic are affected by both intrinsic (crystalline structure) and extrinsic (porosity, grain size, second phase, impurity) factors. The evidence of $Ba_5Nb_4O_{15}$ microwave permittivity in high sintering temperature is associated with the microstructure and relative density[63]. The presence of porosity and amorphous phase, the formation of large grains, are all detrimental to the value of permittivity.[64-65] The value of permittivity thus decreases from 38 to 33 along with the de-sintering. Fitting the linearity of final permittivity with relative density of $Ba_5Nb_4O_{15}$. It can be derived from a mixing rule of the equation (3.4).

$$\text{Effective Permittivity} \approx V_1(\text{porosity}) \times (\text{Permittivity of vacuum: 1}) + V_2(\text{ceramic}) \times (\text{Permittivity of } Ba_5Nb_4O_{15}: 40) \quad (3.4)$$

$V_1+V_2=1$ (Volume ratio of both porosity and ceramic)

The present study demonstrates the importance of sintering behavior on microwave performance. The growth of grains abnormally limits the density can be achieved by pressureless sintering. Further increase in sintering temperature to above 1400°C triggers the reduction of niobium ions. Therefore, the densification of $Ba_5Nb_4O_{15}$ specimen has to be done at a sintering temperature lower than 1400°C. It may be achieved through the addition of grain growth inhibitors or the use of hot-pressing. After a high density is achieved, the ordering of cations can then be

doi:10.6342/NTU201702760

manipulated through the use of an annealing treatment, as the case for $Ba(Zn_{1/3}Nb_{2/3})O_3$ and $Ba(Zn_{1/3}Ta_{2/3})O_3$ [66-67].

The sintering behavior of a cation-deficient perovskite, $Ba_5Nb_4O_{15}$, is investigated in the present study. The highest density can be achieved through pressureless sintering is only 93%. The low sintered density is related to a density decrease, de-sintering, at a sintering temperature above 1250°C. Such de-sintering is contributed by the formation of abnormal grains (>1250°C) and the reduction of niobium ions (>1400°C). When is lower than de-sintering temperature, quality factor Q*x f* value improves which according to the tendency of sintered density. On the contrary, it reverses to lower meanwhile density degradation occurs Fig. 3-16. The quality factor turning to higher when density degradation gets to worse at higher temperature can be illustrated to resonated crystal structure. More studies on the quality factor of microwave dielectric materials proposed the ordering degree of lattice structure. Though the permittivity of sintered $Ba_5Nb_4O_{15}$ is lower after sintering at a temperature higher than 1400°C, its quality factor is higher than 40,000. The increase in quality factor shows a strong dependence on the cation arrangement in the perovskite structure.

3.4.4 Ordering of cation and quality factor

For concerning about dielectric loss at microwave frequency, the grain size and porosity play a minor role. As for the role of structural characteristics, the ordering of cations within hexagonal perovskite is the key. Several studies suggested that the increase of ordering from short range to long range decreases the permittivity and enhances the quality factor. The relative density decreasing as sintering temperature over 1300°C in $Ba_5Nb_4O_{15}$ ceramic were caused by oxygen

doi:10.6342/NTU201702760

atoms dissociated from lattice sites. An obvious microstructure was investigated by pores distributed on grain boundary and grains of ceramics. All of pores were observed developing hugely when increase sintering temperature. Meanwhile the shape of sintered body expanded contrarily which explained to de-sintering phenomena. The obtained dielectric loss at resonated frequency proved to pores diminished density of $Ba_5Nb_4O_{15}$ when sintered at higher temperature. XPS analysis on sintered ceramics deduced chemical shift on niobium valence state generating oxygen atoms out of lattice site. The pores coarsened from diffusion of oxygen atoms continually driving by temperature. Finally expanded volume of ceramics exhibit relative density decreasing.

As for the quality factor, the increase of porosity, the growth of grains and the presence of an amorphous phase all lower its value. However, the quality factor increases significantly as the specimens are sintered above 1400°C. Apart from extrinsic factors, the quality factor of microwave ceramic depends strongly on its crystalline structure, especially on the cation arrangement within the structure. Nevertheless, the XRD patterns for the sintered specimens in the 2θ range from 25°to 70° are the same in Fig. 3-11. The ordering of cations can be characterized with XRD analysis at high 2θ angles[68-69], or with a Raman technique[70], or with the atomic position simulation from HRTEM micrographs[71-72]. Figure 3-12 shows the XRD patterns in the 2θ range from 115° to 125°. A broad peak near 119.5° splits into two peaks with the increase of sintering temperature, implying the ordering of cations increases from short-range to long-range. It suggests that the increase of sintering temperature, apart from de-sintering, the ordering of cations is improved. However, the increase of cation ordering is not beneficial to permittivity, the permittivity is thus further decreased above 1400°C.

Another approach to improve lattice ordering of $Ba_5Nb_4O_{15}$ is to increase the soaking time at a certain temperature 1300°C. Fig. 3-17 (a) reveals the quality factor slightly enhanced by soaking

doi:10.6342/NTU201702760

time. Although it raises quality factor, but the contribution from increment of soaking time is much less than the driving force from temperature. There is a tendency of work energy can give the benefit of moving a certain lattice plane into a long- range ordering. XRD pattern of Fig. 3-17 (b) at high 2θ angle also has a proof on 119.5° plane as different soaking time.

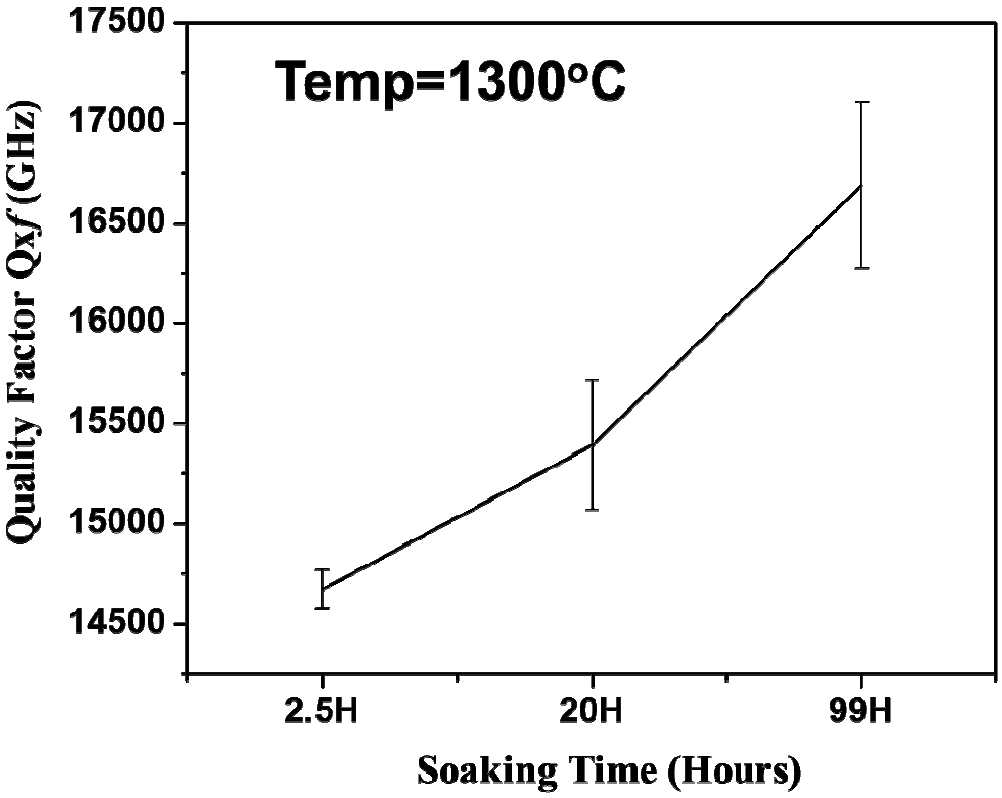

Fig. 3-17 (a) The quality factor vs. soaking time of sintering $Ba_5Nb_4O_{15}$ at 1300°C

doi:10.6342/NTU201702760

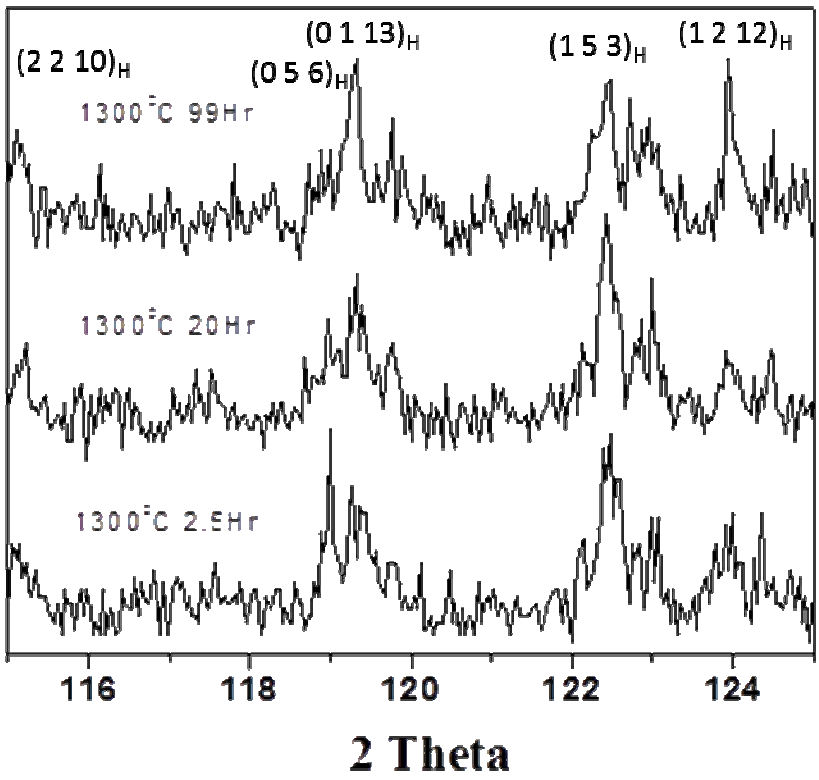

Fig. 3-17 (b) XRD intensity of ordering lattice plane vs. soaking time at 1300°C

doi:10.6342/NTU201702760

3.5 Conclusion

High temperature sintered $Ba_5Nb_4O_{15}$ conducts to counter densification in this study. There is a limiting density for the preparation of $Ba_5Nb_4O_{15}$ specimen through liquid phase sintering. Such density limit is mainly resulted from the abnormal grain growth at a sintering temperature above 1250°C. At the temperature, the density is only 93%, further increase of density is not possible. The increase in the sintering temperature results in the reduction of Nb^{+5} ions at a temperature above 1400°C, the density is further reduced. Oxygen gas are generated along with the reduction reaction. Weight loss experiment gives proof of gas phase evaporation. The increase of porosity and grain size reduces the permittivity of $Ba_5Nb_4O_{15}$ specimen. However, the order of cations in $Ba_5Nb_4O_{15}$ perovskite is improved with the increase of sintering temperature; the quality factor is therefore enhanced. Increasing soaking time can help to improve the quality factor slightly.

doi:10.6342/NTU201702760

Chapter 4: Mechanochemical Property of $Ba_5Nb_4O_{15}$

4.1 Introduction

$Ba_5Nb_4O_{15}$ belongs to 5H-hexagonal perovskite structure[73]. It exhibits high permittivity with low dissipated energy at microwave frequency. And without a doubt it is candidate of industrial material for RF components. To synthesize $Ba_5Nb_4O_{15}$ material is always a challenging route for stabilizing performance such as quality factor properties. A solid-state route for preparing $Ba_5Nb_4O_{15}$ through mechanical treatment is an ordinary process step. The reported Q×*f* quality factor for the dense $Ba_5Nb_4O_{15}$ is usually lower than 40,000. The disadvantage of dissipation performance applying into microwave components is still an object to improvement. However, the quality factor behavior of $Ba_5Nb_4O_{15}$ has attracted little attention.

High speed mechanical rotating ball milling or high energy attrition process has been utilized to homogenize complex compositions of ceramics in few decades. There are abundantly researches on mechanochemical phenomena in size scale control of ceramic powders[74-76]. Apart from $Ba_5Nb_4O_{15}$ layered perovskite material, the well recognized process is the most promising method to activate reactivity of starting materials and increase numbers of nucleation sites through mixing downsizing powders. In contrary, Senna's study on soft-mechanochemical synthesize route accommodates stereotyped demerit of mechanochemical process[77]. Psiuk's work on $SrTiO_3$ demonstrated the disadvantage of unstable stoichiometry at near surface layer of grain area[78]. It concluded electronic structure changed via milling process. Regarding to the case of $Ba_5Nb_4O_{15}$, there is a lack of attentions on researching these issues.

The explanation of quality factor performance of microwave ceramics was originated from its intrinsic and extrinsic characteristics. In general, the role of ordering structure in layered perovskite can be carried out investigation practicall[79]. As far as mechanochemical energy activating on

doi:10.6342/NTU201702760

$Ba_5Nb_4O_{15}$ influence the quality factor are concerned[80], the decline of ordering structure has been discovered. In the present work, the mechanochemical behavior of $Ba_5Nb_4O_{15}$ hexagonal perovskite is investigated. The polarization performance of $Ba_5Nb_4O_{15}$ in radio frequency is verified with its microstructure and crystalline structure. The grain will grow along with a habit plane of $Ba_5Nb_4O_{15}$ when sintered at elevated temperature 1435°C. It was enhanced by mechanical treatment combined with water and confirmed by TEM analysis. From macroscopic verification of the preferred orientation planes, XRD pole figure and EBSD analysis also have a consistence evidence on this study.

4.2 Experimental method

4.2.1 Raw material preparation

A conventional solid-state reaction process synthesized $BaCO_3$ and Nb_2O_5 materials with stoichiometric mole ratio 5.0:2.0 was used to prepare $Ba_5Nb_4O_{15}$ powder. Both of raw materials are electronic grade purity higher than 99.9% which mixing with distill water accomplish on 220rpm planetary mill. The media balls were 2mm yttrium stabilized zirconia and milled powders to 1.50um. After drying, powders were calcined at 1000°C with soaking 2.0 h to complete solid-state reaction then pulverized it. The pulverized powders were treated as a standard sample without wet

doi:10.6342/NTU201702760

mechanical treatment process. To control $Ba_5Nb_4O_{15}$ particle sizes, 63% solid content of powders with distilled water were treated by high energy planetary mill for different milling time duration. In this stage, all milling conditions are set 2mm YTZ ball as grinding media but 2mm Al_2O_3 ball will be another choice to compare with reference.

4.2.2 Experimental flow chart and procedure

The milled powders were measured by laser diffraction type particle size analyzer (LA-920, Horiba Co., Japan). After drying, all milled powders forming to 10mm diameter cylinder type samples were sintered at elevated temperature 1435°C. To verify the milling effect on $Ba_5Nb_4O_{15}$ ceramic that barium ion dissolved into water after mechanical treatment, 63% solid content of milled slurry were diluted to 10% by distilled water then sieved by filter paper. All filtered water represents the specimen were quantitatively analyzed by Inductively coupled plasma spectrometer (ULTIMA2, Horiba Co., Japan). The weight loss characteristics of milled $Ba_5Nb_4O_{15}$ can be conducted by weighting samples procedures same as previous chapter. Both of milled powders and crushing sintered specimen to powders were identified the phase by X-ray diffractometer (D8 Advance, Bruker Co., Germany). Two ranges of scanned angles were set at lower angle range ($20\sim50^o$) with 0.015 degree/step and 1.0 s/step; for higher angle range ($115\sim125^o$) was 0.01 degree/step and 2.0 s/step.

To observe $BaCO_3$ which is transferred from dissolved barium ion, more distilled water can be used to flush slurry into a beaker. The suspended powder on the top of water will be captured after

doi:10.6342/NTU201702760

diluted slurry sedimentation. Meanwhile the microstructure of sintered $Ba_5Nb_4O_{15}$ specimen were observed on free surface and fracture surface conducted with scanning electron microscopy (JSM-6360, JEOL Co., Japan). A preferred orientated lattice plane of milled $Ba_5Nb_4O_{15}$ ceramic has been investigated by TEM (JEM-2100, JEOL Co., Japan) analysis. Another demonstration of two dimensional detectors X-ray diffraction analysis (D8 SSS, Bruker Co., Germany) proved the textured grains by pole figures. EBSD analysis (Helios 600i, FEI Co., USA) can figures it out at small range of detection area.

The diameter of the green pellets was 10 mm; the thickness was 5.0 mm. The milled $Ba_5Nb_4O_{15}$ powder granular with 4% PVA binder was formed under 140MPa to compact 64 % R.D. The de-binder temperature was 400°C then ran with sintering temperature at 1435°C holding 2.5hr. Permittivity value and quality factor of each $Ba_5Nb_4O_{15}$ ceramic specimen were measured by cavity resonated method which were analyzed with a network analyzer (HP-8720ET, Agilent Co., USA) at the frequency of 5 GHz to 6 GHz. Fig. 4-1.

doi:10.6342/NTU201702760

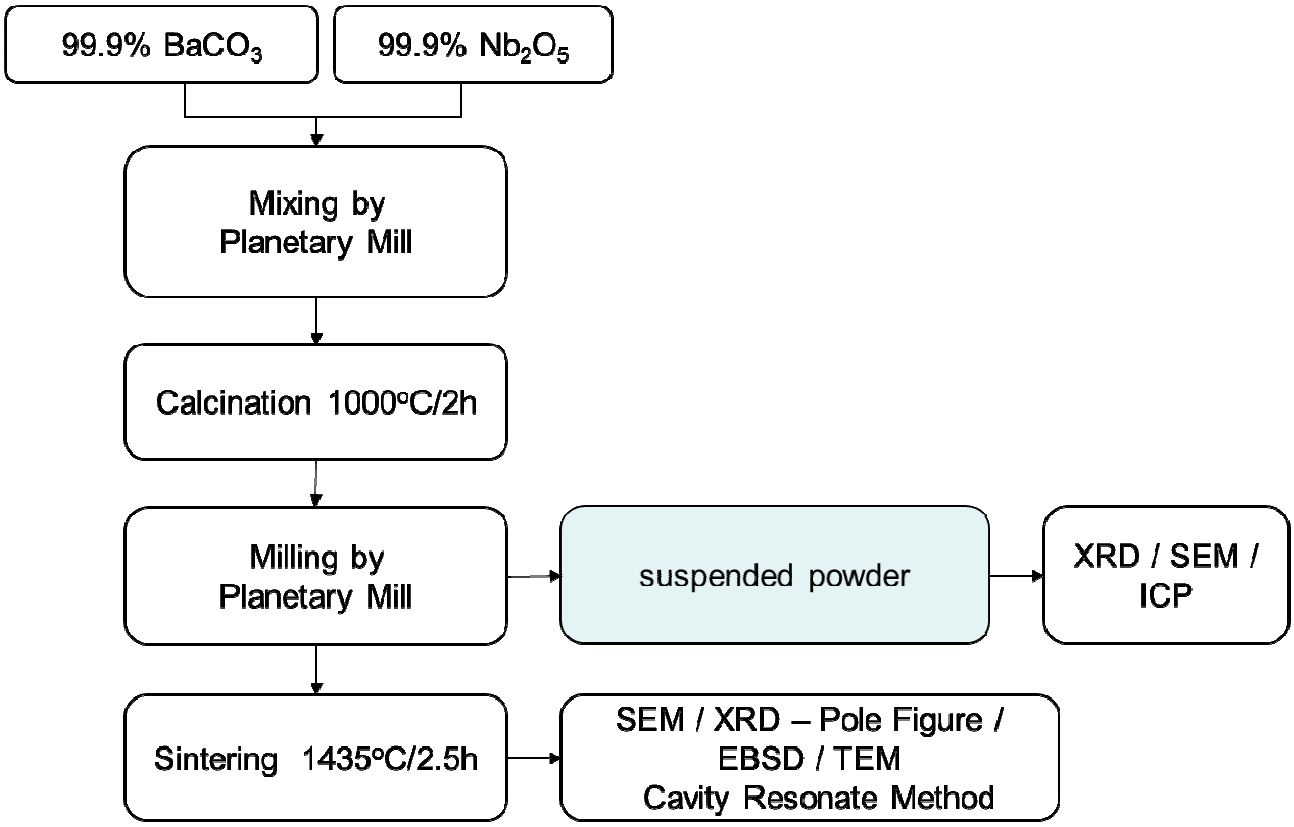

Fig. 4-1 Experimental flow chart

doi:10.6342/NTU201702760

4.3 Result

4.3.1 Milling ability of $Ba_5Nb_4O_{15}$ powder

After planetary mill process, the curve of $Ba_5Nb_4O_{15}$ powder size distribution compared to milling time reveals on Fig. 4-2. Mean size of pulverized powder is 2.52um with broaden distribution before wet milling. As pulverizing force adding to calcined powders, the signification of coarse powder is breaking down through mechanical energy. Bimodal distribution of particle size transforms into Gaussian distribution progressively. The final specimen is achieved to 0.44um mean size has one normal distribution after operating 120min in Table 4-1. At the same time, sintered density is also investigated by Archimedes method. There is tremendously worse thing happened at milling treatment. De-sintering phenomena appears more easily. Density degradation is always accordance with particles size decrease. But on the contrary, the finest specimen turns upward due to higher densification rate. The intensive energy from mechanical practice may induce anisotropic grain growth or niobium ion reduction as previous study.

Figure 4-3 shows the weight loss of milled powder at 1435^{o}C for 2.5h. The weight loss corresponds the trend of loss percentage related to particle size. The finest powder sample reveals nearly 0.97% loss compared to pulverized powder is 0.63%. The lost substance is not only oxygen gas from reduction of $Ba_5Nb_4O_{15}$ but also other matter which should be verified by XRD phase identification. The weight of sintered finer powder lost higher than coarser powder. It is a hint of more decomposed $Ba_5Nb_4O_{15}$ caused to weight loss through mechanical energy transportation.

doi:10.6342/NTU201702760

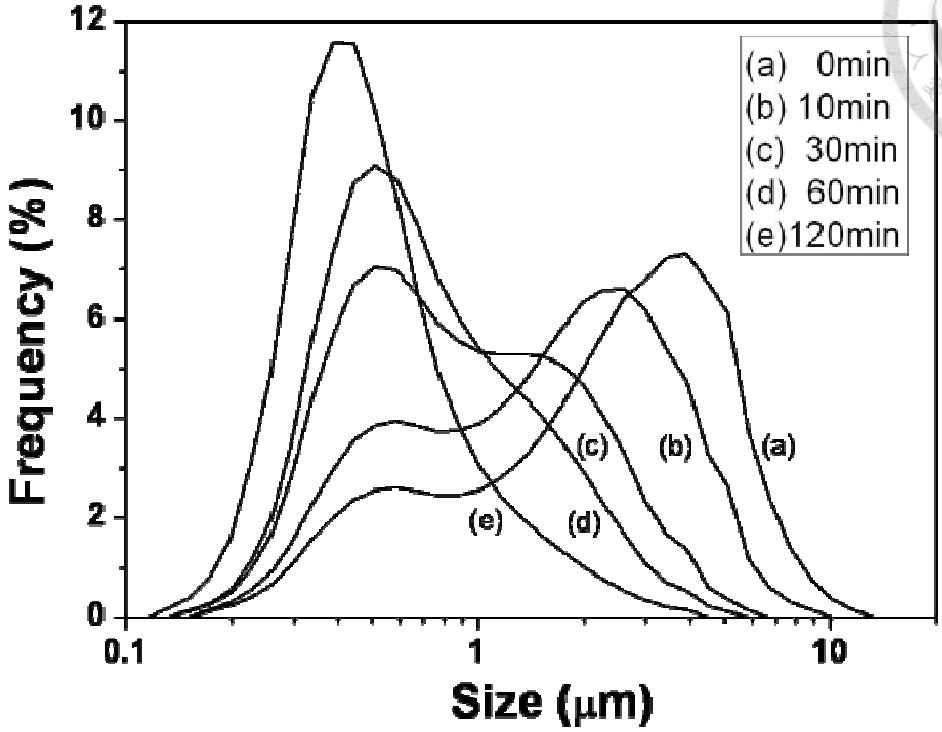

Fig. 4-2 Particle size distribution for milled $Ba_5Nb_4O_{15}$ powders vs. milling time

Table 4-1 Particle size and sintered density of milled $Ba_5Nb_4O_{15}$ powders vs. milling time

Milling Time (min)	Mean particle size / μm	Sintered density / g/cm^3
0	2.52	5.49
10	1.63	5.07
30	0.96	5.01
60	0.67	4.72
120	0.44	4.77

doi:10.6342/NTU201702760

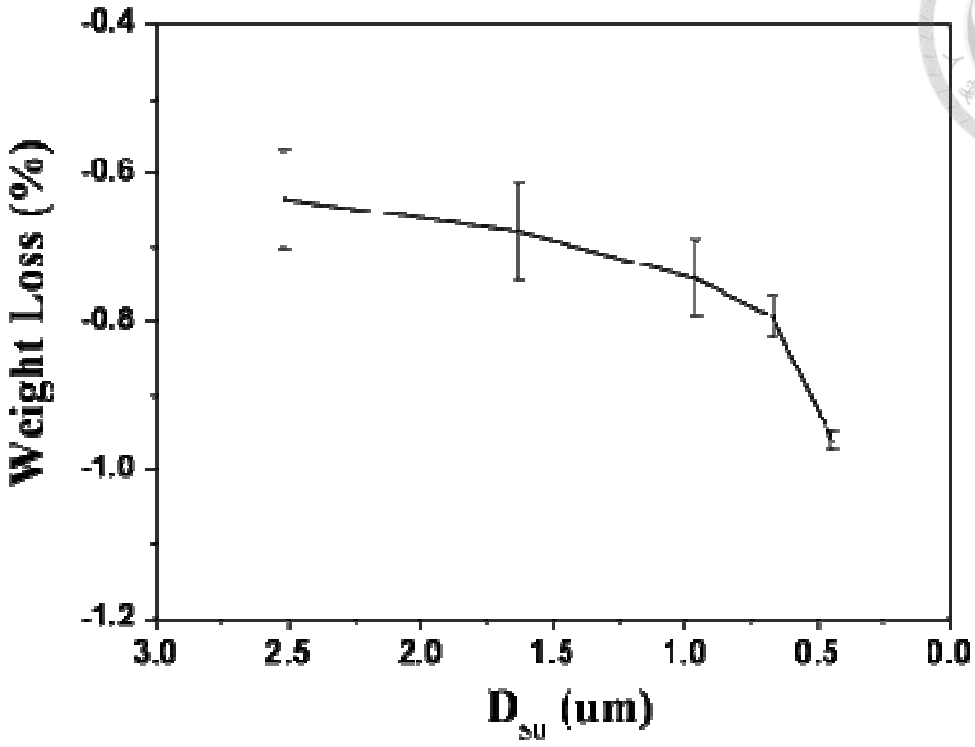

Fig. 4-3 Weight loss of $Ba_5Nb_4O_{15}$ specimen as a function of milled particle size

Another trail test using Al_2O_3 grinding media at milling process shows a terrible result on density degradation and weight loss properties. Certainly, the microwave characteristic is much worse than YTZ media affect Fig. 4-4. Comparing both milled powders to check contamination by XRF (WDS3370, Rigaku Co., Japan), Al_2O_3 content is much higher than ZrO_2 under the sample milling condition. (Table. 4-2). The impurity composition is the root cause to degrade densification.

doi:10.6342/NTU201702760

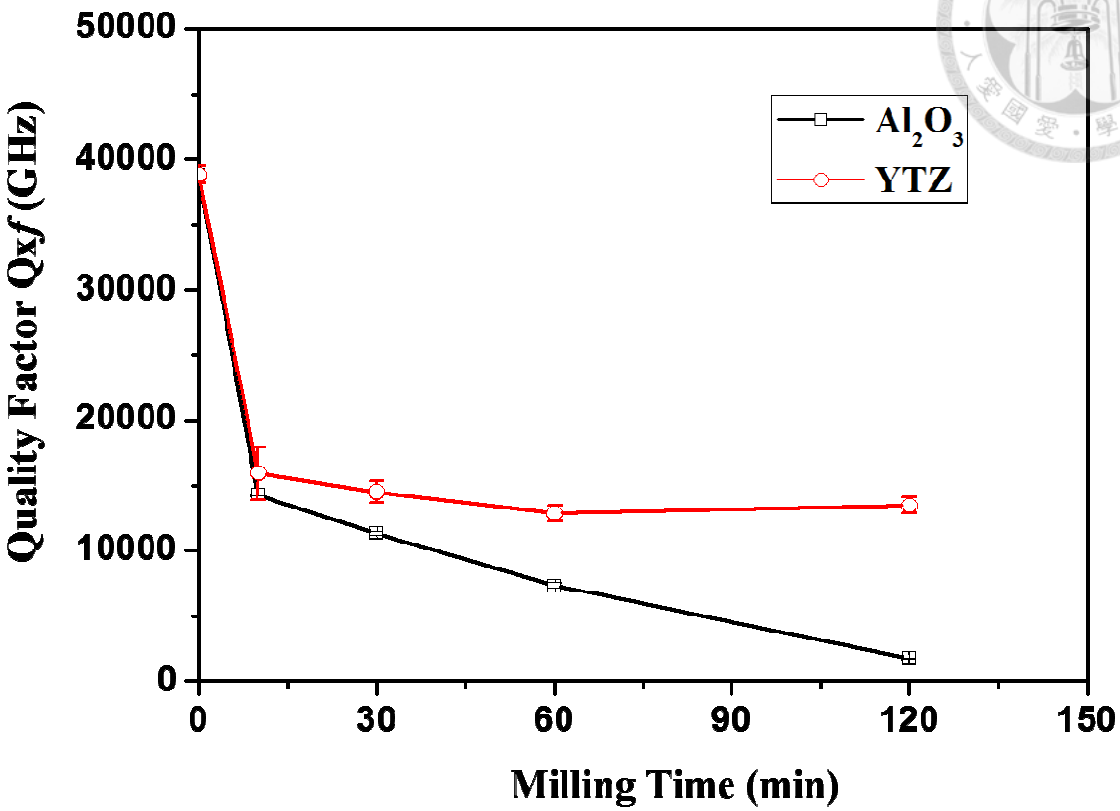

Fig. 4-4 Milling media influence on quality factor of $Ba_5Nb_4O_{15}$

Table 4-2 Grinding media contamination through milling time

Media	2mmYTZ				2mm Al_2O_3			
Time (min)	BaO (%)	Nb_2O_5 (%)	ZrO_2 (%)	Al_2O_3 (%)	BaO (%)	Nb_2O_5 (%)	ZrO_2 (%)	Al_2O_3 (%)
10	39.118	60.750	0.001	0.131	38.854	60.855	0.000	0.291
30	38.233	61.631	0.000	0.137	38.868	60.705	0.000	0.427
60	37.815	62.038	0.011	0.125	38.863	60.347	0.000	0.790
120	36.804	63.031	0.048	0.117	37.945	60.123	0.000	1.932

doi:10.6342/NTU201702760

4.3.2 Leaching phenomena

Milled $Ba_5Nb_4O_{15}$ powders were also checked by XRD and obviously find second phase on pattern compared with different milling time. All diffracted peaks in Fig 4-5 presents the patterns of $Ba_5Nb_4O_{15}$ powder at different milling time. The Rietveld analysis of patterns from 20 to 50° determines all the diffraction planes. Enlarge the pattern to seek the low intensity of exclusive peak, a plane at 23.9° was not original phase. Identifying the peak by JCPDS 71-2394 database, it is fit with the (111) plane of $BaCO_3$[81]. The intensity of $BaCO_3$ was a little dependent on milling time. More pulverization energy applied on $Ba_5Nb_4O_{15}$ powder, more residual barium carbonate was generated from treated powder. Based on the principle of mass conservation, the chemical substance never disappeared but only transferred to other form with the same weight. Barium carbonate must be recovered from barium ion leaching at aqueous solution. Barium ion reacted with carbonate water according to a sequential precipitation to recrystallization. Finally, the new phase barium carbonate precipitated in the aqueous solution and found by XRD identification.

The extraction of barium ion from $Ba_5Nb_4O_{15}$ crystal site through the mechanical energy occurs the solid phase into water phase. Leaching phenomena is the unique feature in $Ba_5Nb_4O_{15}$ milling process. Precipitated $BaCO_3$ plays a role of segregation substance mixed into main powder. Later the sintered microstructure also proved the existence of excess composition. From the Rietveld refinement of diffraction peaks of sintered specimens, it can be identified the peak 38.1° is (0 0 5) plane. The fluctuated intensity of (0 0 5) plane and broad FWHM of others peaks show not all planes are smaller crystalline size. There will be a preferred plane must enhance the formation of $BaCO_3$ by mechanical energy. Fig. 4-6.

doi:10.6342/NTU201702760

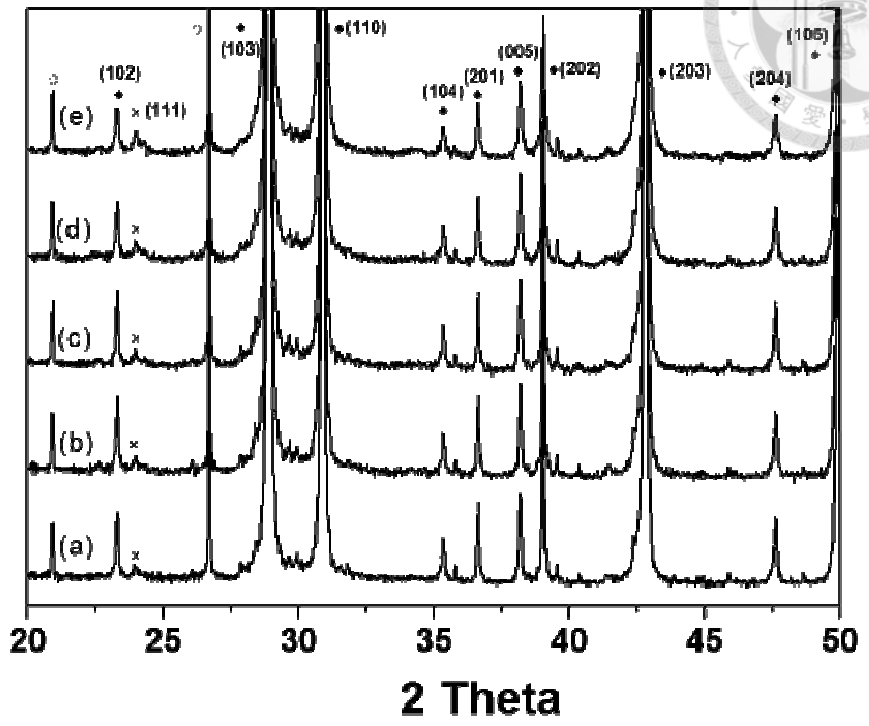

Fig. 4-5 XRD patterns of the milled $Ba_5Nb_4O_{15}$ powder: (111) $BaCO_3$ (a) 0 min (b) 10min (c) 30min (d) 60min (e) 120min ◆:$Ba_5Nb_4O_{15}$ ×: $BaCO_3$

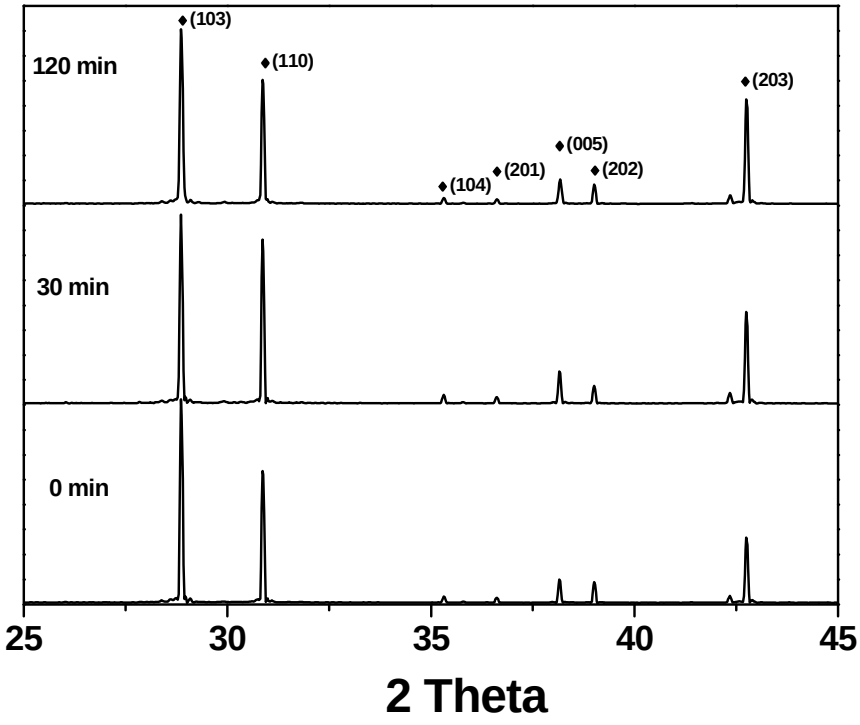

Fig. 4-6 Sintered samples of milled $Ba_5Nb_4O_{15}$ with different milling time

doi:10.6342/NTU201702760

4.3.3 Interaction with water of milled $Ba_5Nb_4O_{15}$

The excess decomposition indicates that $Ba_5Nb_4O_{15}$ generate reactant matter when milled with water. Fig. 4-7 shows an evidence of free barium ion in the water which separating from diluted slurry and determinate the concentration by ICP. Measuring all filtering water quantitatively calibrate with 1000ppm Barium standard solution. The dissolved barium ion from $Ba_5Nb_4O_{15}$ has 535ppm after 120min milling time. Milling in water is approximately 50 times higher than pulverized powder. The mechanical energy apply on $Ba_5Nb_4O_{15}$ will generate free barium ion dissolved into water. The evidence of $BaCO_3$ peak reaches its highest value at milling 120min. The semi-quantification of precipitated $BaCO_3$ is relative to ICP result of barium ion concentration.

To observe the precipitated $BaCO_3$ which was taken from milled solution, 10% solid content diluted slurry drains into 500c.c beaker with clean water. After 30min sedimentation, there are abundantly suspended white powder flocculates on the top of water. More pulverizing energy(time) applying, there will produce more chipped powder with reduction of barium ion precipitation suspend on the surface of diluted solution. Figure 4-8 exhibits precipitated powder $BaCO_3$ were needle-like morphology from nano to micro scale. All of them blend with chipped $Ba_4Nb_4O_{15}$ powder.

A typical redox reaction as equations (1) & (2) can illustrate the formation of $BaCO_3$ when mechano-chemical interaction between $Ba_5Nb_4O_{15}$ and H_2O two reactants. External carbonate ion came from carbon oxide gas dissolving into acidic water. Amorphous $BaCO_3$ precipitate initially and grows into recrystallization under drying temperature and time.

$$Ba^{+2} + H_2O \rightarrow Ba(OH)_2 + 2H^+ \quad (1)$$

$$Ba(OH)_2 + CO_{2(aq)} \rightarrow BaCO_{3(s)} + H_2O \quad (2)$$

doi:10.6342/NTU201702760

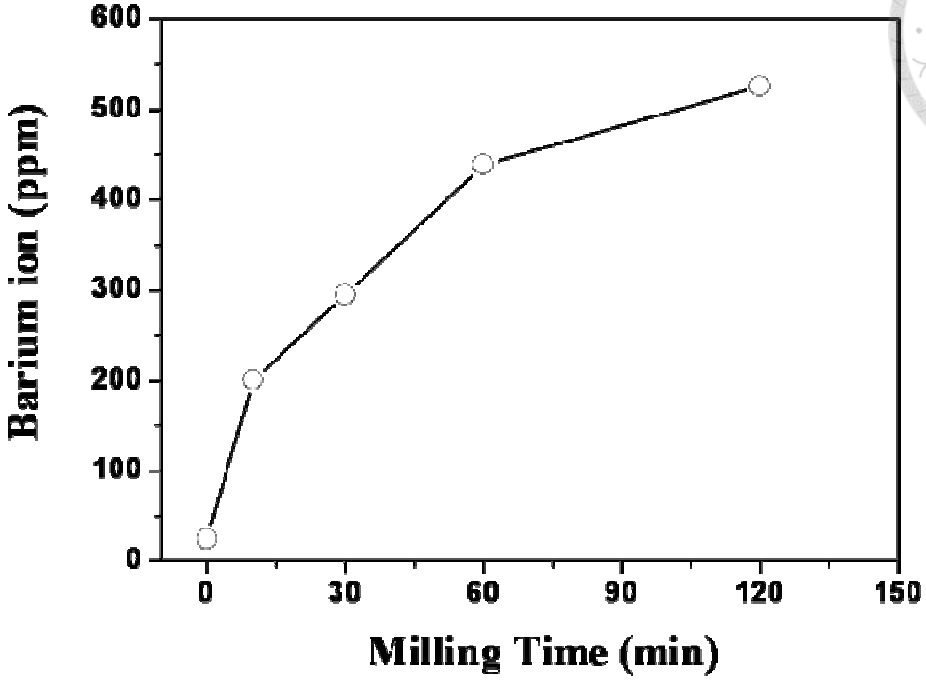

Fig. 4-7 Barium ion concentration after milling

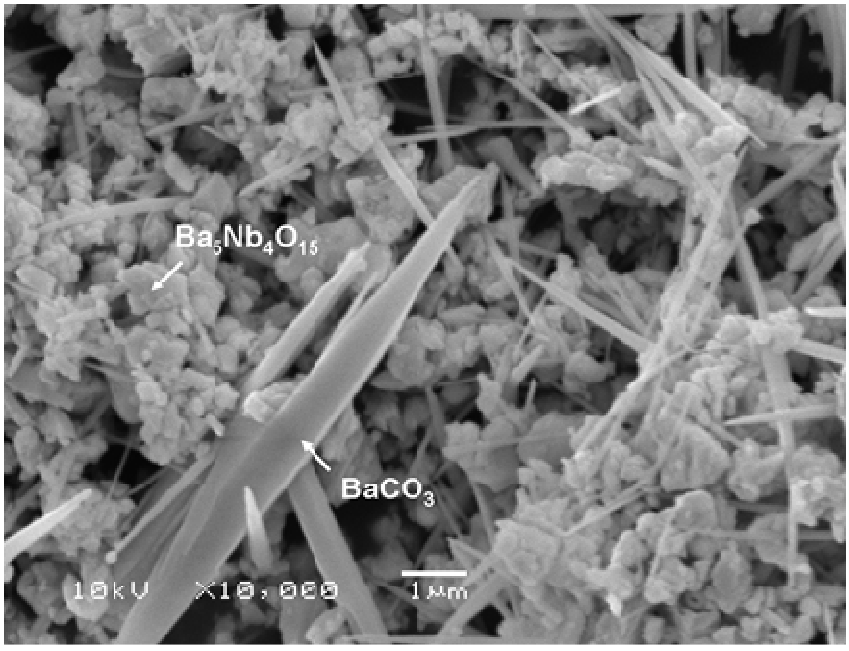

Fig. 4-8 Morphology of $BaCO_3$ precipitated from filtering water of milled slurry

doi:10.6342/NTU201702760

Proposed mechanism for the leaching of metal ion model in Fig. 4-9 shows barium ions were split out from corner of lattice site. It dissolved with H_2O reactant to form hydroxide product. On the other hand, carbon dioxide entered the water through equilibrium with atmosphere. The aqueous carbon dioxide reacts with water forming carbonic acid. In the end, the neutralization reaction has taken place at barium hydroxide alkaline base with carbonate acid to form $BaCO_3$ precipitate product.

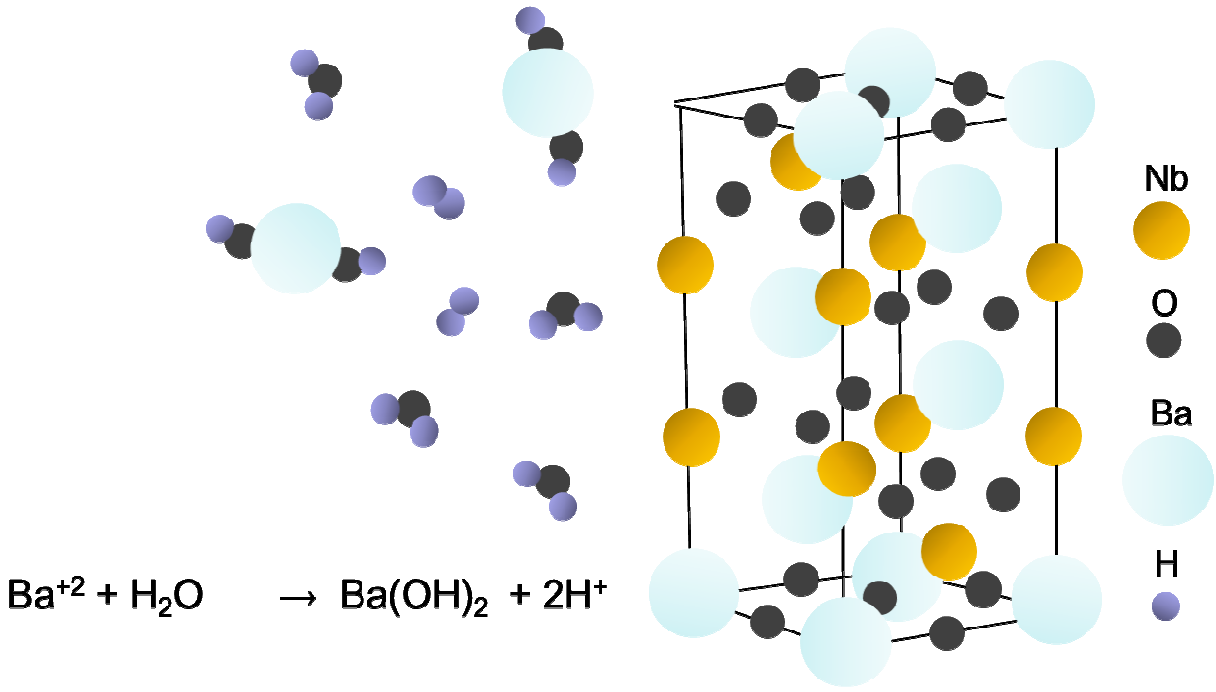

Fig. 4-9 Mechanochemical reaction mechanism of barium ion dissolving in water

doi:10.6342/NTU201702760

4.3.4 Anisotropic grain growth

Fig 4-10 (a)&(b) shows the free surface microstructure of sintered specimen at different milling time. Pulverized powder without wet milling operated at 1435°C reveals nearly angular grain. The anisotropic grains grow at preferred direction present abnormal growth when milling with water intermedia. More intensive milling time transfer to mechanochemical energy on $Ba_5Nb_4O_{15}$ ceramic which grows habitually on an oriented plane. The aspect ratio of grains was varied from 2.5 to 50. The more mechanical energy impacts on the powders, the more surface area of powders will generate leaching barium ions. There are extensive high aspect ratio type grains accomplished by milling 120min Fig. 4-10 (d). The morphology is not so much as textural structure but random distributed on free surface. There is strong tendency of crystalline direction which a preferred plane plays the role of grain growth plane.

The fracture surface microstructure of specimens is also shown in Fig 4-11. No doubt, abundant pores were isolated and accumulated along the grains boundary. Some pores trapped in grain indicates grain boundary moving speedily than pore vanish under temperature driving force. All of the pores in grains has spherical shape due to balance the vaporization pressure of oxygen gas coming from niobium reduction. In contrary to the increase milling time as in Fig 4-11(b), observation of trapped pores was less than Fig 4-11(a) but pores at the triple area of conjunctive grains were much more and bigger. It seems to anomalous mobility of pores has been related to high diffusivity at a preferred lattice site. That pore mobility is higher than grain boundary mobility.

doi:10.6342/NTU201702760

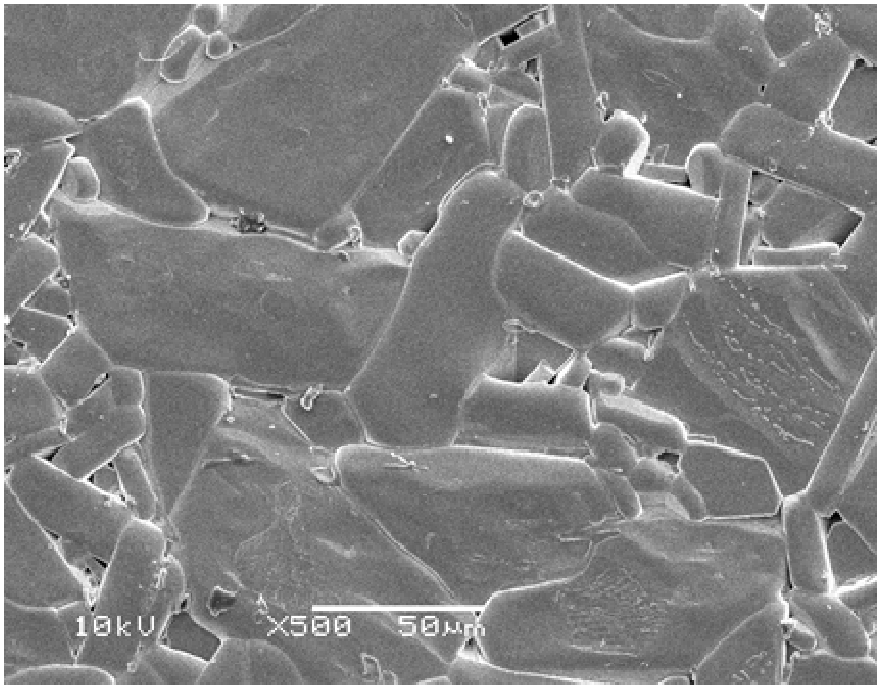

Fig. 4-10 (a) Free surface of unmill $Ba_5Nb_4O_{15}$

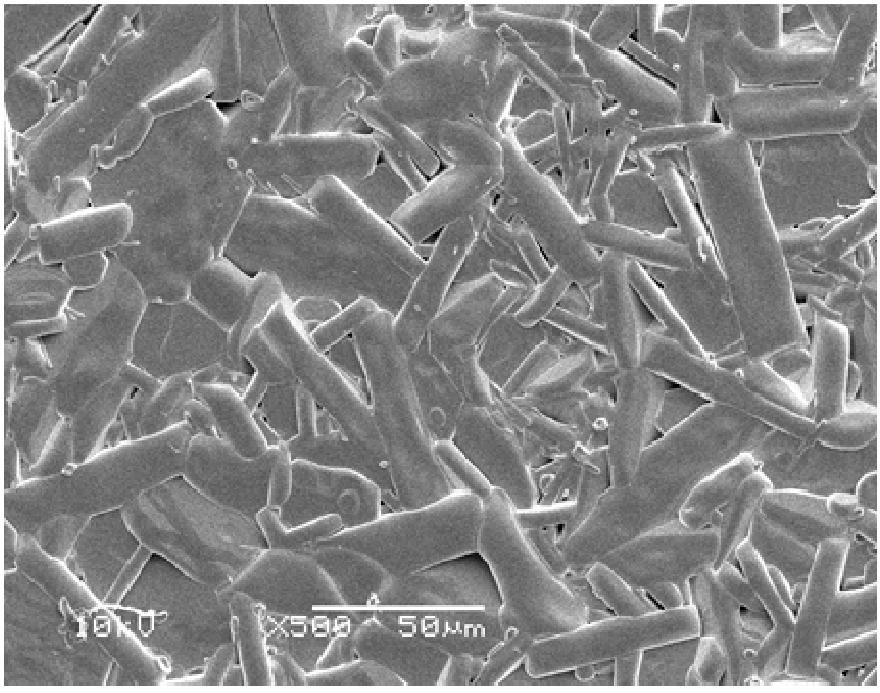

Fig. 4-10 (b) Free surface of mill 30min $Ba_5Nb_4O_{15}$

doi:10.6342/NTU201702760

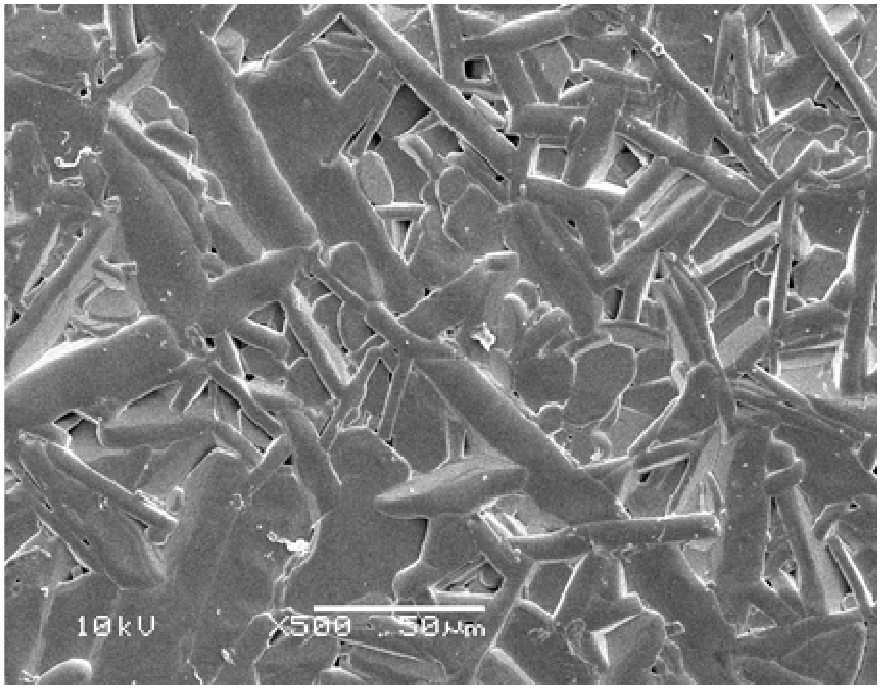

Fig. 4-10 (c) Free surface of mill 60min $Ba_5Nb_4O_{15}$

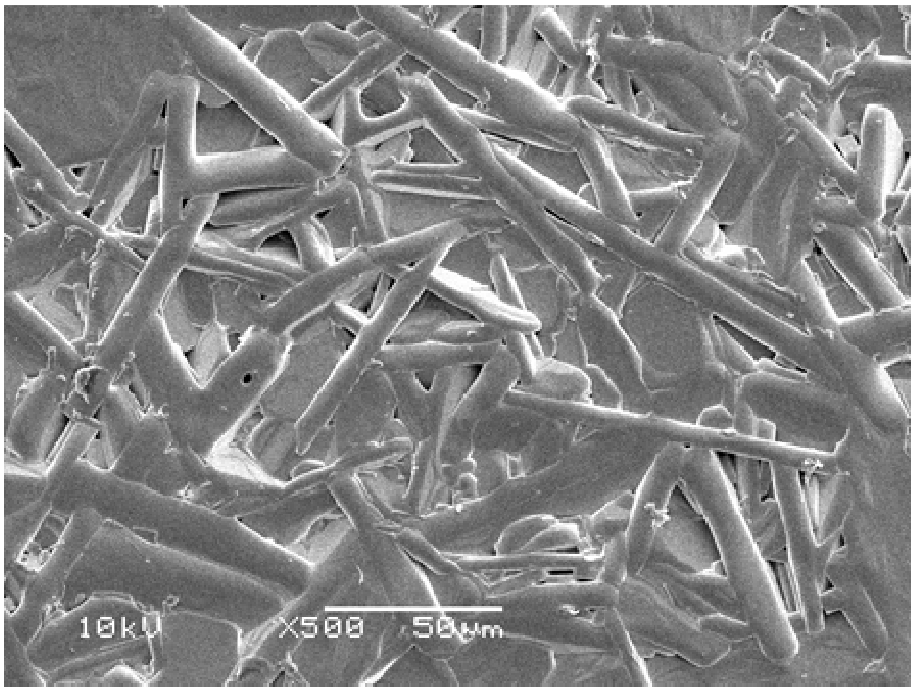

Fig. 4-10 (d) Free surface of mill 120min $Ba_5Nb_4O_{15}$

doi:10.6342/NTU201702760

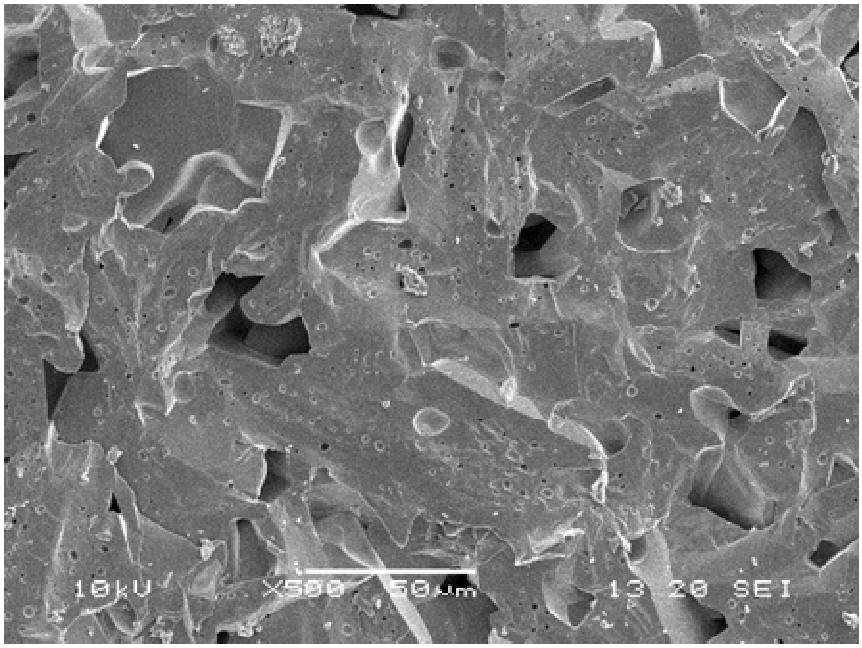

Fig. 4-11 (a) Fracture surface of milled 60min $Ba_5Nb_4O_{15}$

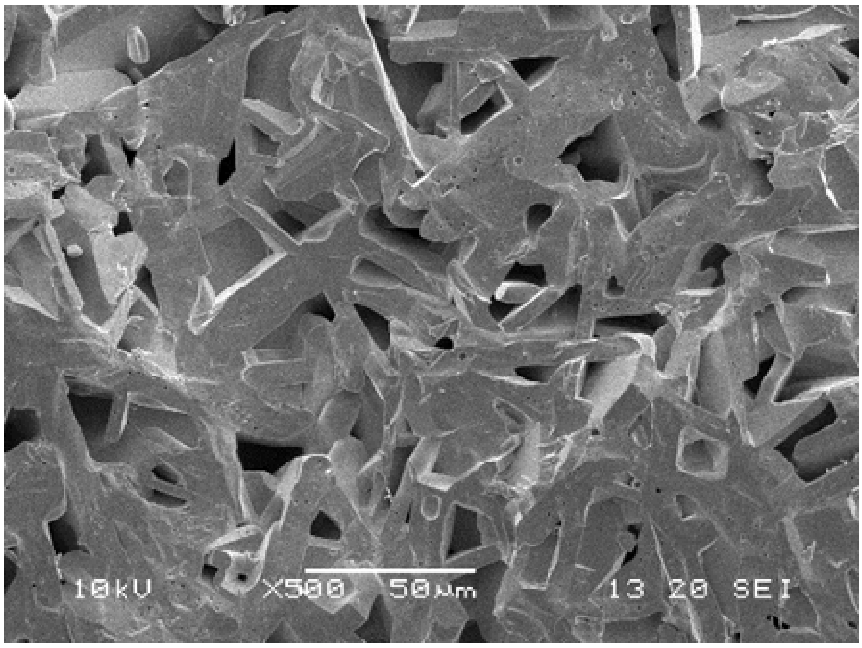

Fig. 4-11 (b) Fracture surface of milled 120min $Ba_5Nb_4O_{15}$

doi:10.6342/NTU201702760

4.3.5 Weight loss of sintered $Ba_5Nb_4O_{15}$

The indication of weighting sintered specimen is an easily experimental method for observing the differentiation. $Ba_5Nb_4O_{15}$ has been identified the high temperature weight loss characteristics. The result from milled specimen by milling time has linearly decomposed trend within weight loss test. Fig. 4-12. Comparing to Fig.4-3, the relevance of particle size and weight loss can't show much empirical evidence on mechanical energy factor. The precipitated $BaCO_3$ offers CO_2 decomposed from milled powder.

Furthermore, the relative density of sintered specimen disastrously degraded when treated by wet milling process. It declined to 75% relative density at the last specimen. Anisotropic growth and pores generation are the main causes of de-sintering phenomena. The milling process for treating $Ba_5Nb_4O_{15}$ gives a trap for densification stage.

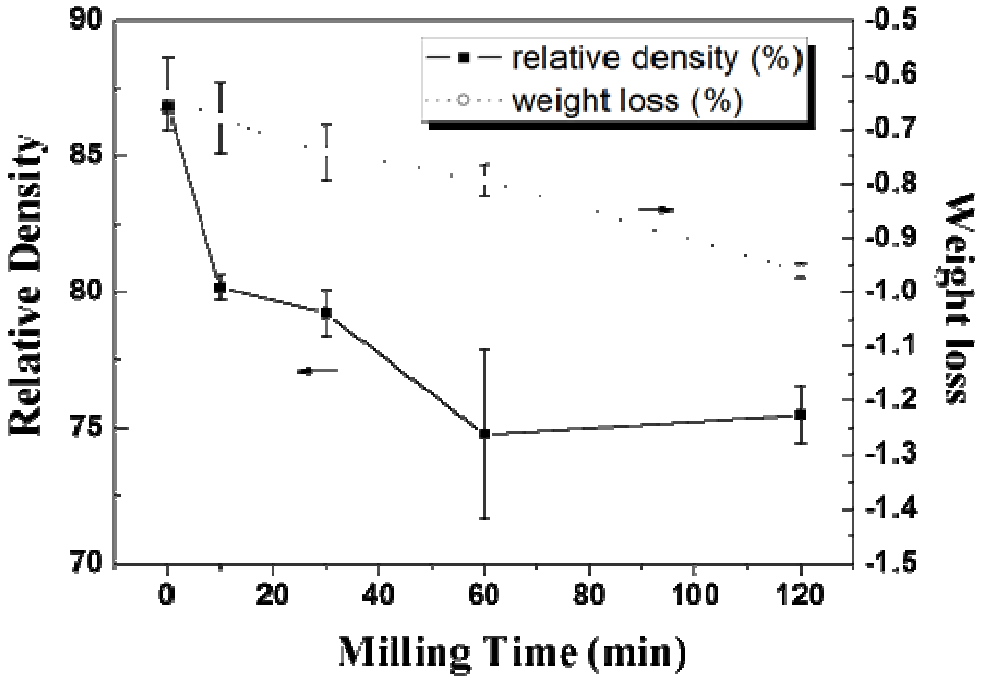

Fig. 4-12 Milling vs. weight loss and relative density

doi:10.6342/NTU201702760

4.3.6 Microwave characteristic

Once again, the relation between relative density and permittivity is complying with a mixing rule. Effective permittivity of sintered specimen can be derived from level rule of vacuum and theoretical permittivity of $Ba_5Nb_4O_{15}$. Fig. 4-13. The microwave characteristics of sintered $Ba_5Nb_4O_{15}$ specimen compared with mechanical treatment process condition as in Fig 4-14. Permittivity value of sintered $Ba_5Nb_4O_{15}$ ceramic varied from 35.2 to 30.6 complying with milled particle size.

The importance of quality factor is the merit of microwave dielectric material. High quality factor is the performance of passive electronic component which has a good selectivity and less energy dissipation in circuit. Regard to $Ba_5Nb_4O_{15}$ material system, the highest quality factor can reach to 42,500 GHz without wet milling treatment. If treated to milling in water, the quality factor declines dramatically as more intensive milling energy apply on $Ba_5Nb_4O_{15}$ ceramic. It is near to half the original value.

However, XRD diffraction analysis can give an evidence on the degree of ordering structure at high Miller index plane. Considering the analysis results between quality factor and high angle plane of $Ba_5Nb_4O_{15}$ is highly related. In previous chapter, the X-ray diffraction pattern of sintered ceramic confirmed the 2θ angle at 119.3° was the indication of ordering plane (0 1 13). The intensity of diffraction peak tends to decrease when milling time increase. Fig 4-15. The lateral plane (0 5 6) oppositely increases as long as milling time increasing. Many literatures state on microwave dielectric materials explain oxygen octahedral tilt is the fundamental essay for contributing lattice ordering[82-84]. Two adjacent planes owned high indices can be associated to oxygen octahedral tilt indirectly.

doi:10.6342/NTU201702760

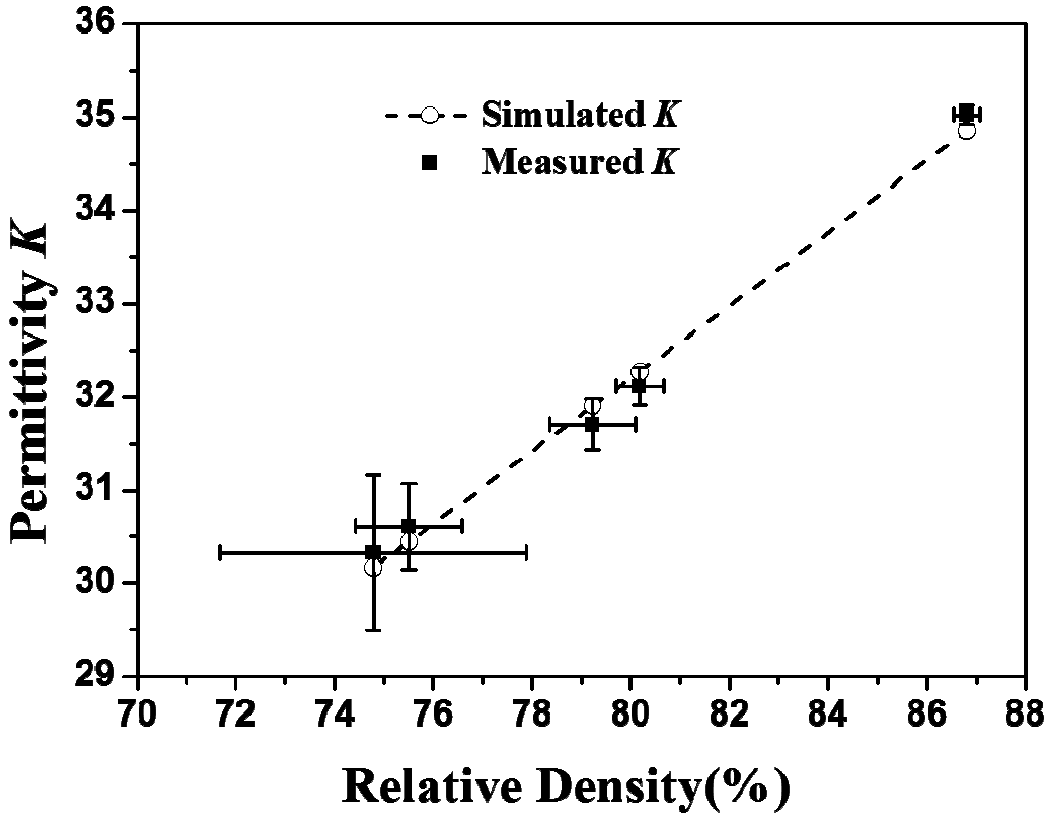

Fig. 4-13 The relative density vs. permittivity of $Ba_5Nb_4O_{15}$

doi:10.6342/NTU201702760

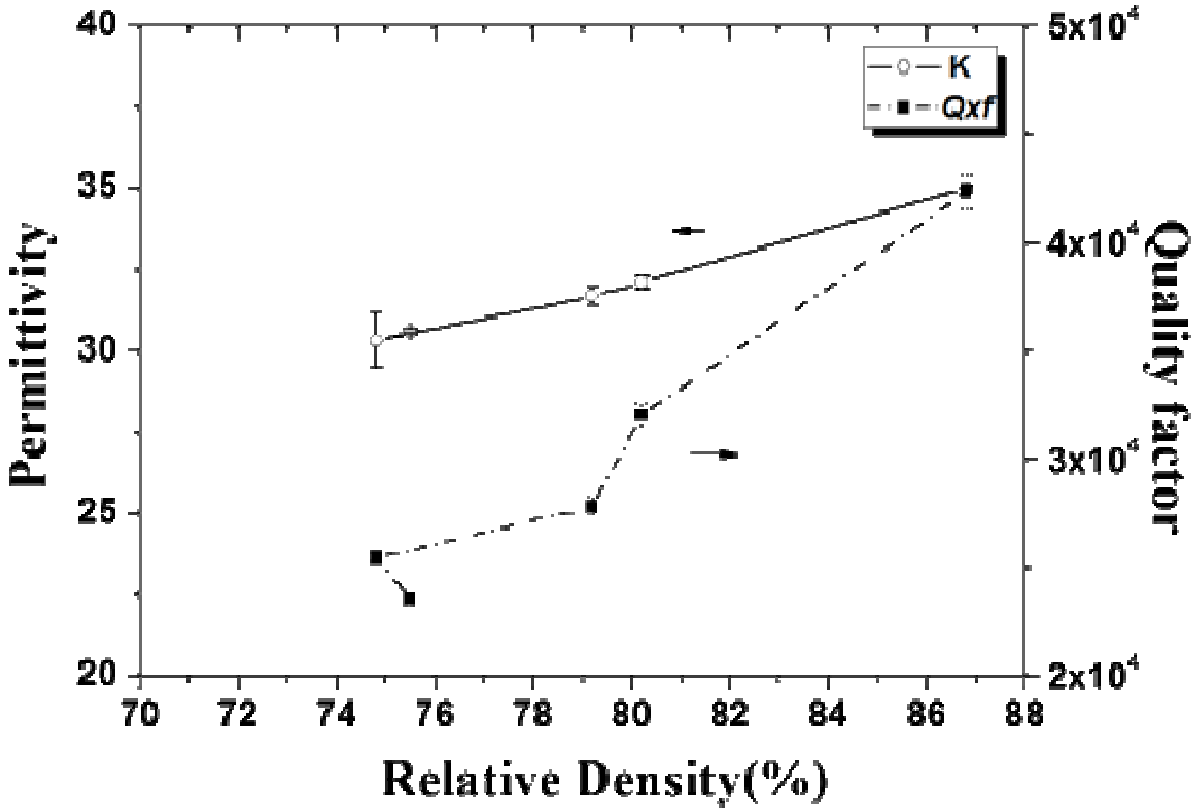

Fig. 4-14 Permittivity (*K*) and quality factor (*Qxf*) for the sintered $Ba_5Nb_4O_{15}$ specimens prepared using the powders milled for various times.

doi:10.6342/NTU201702760

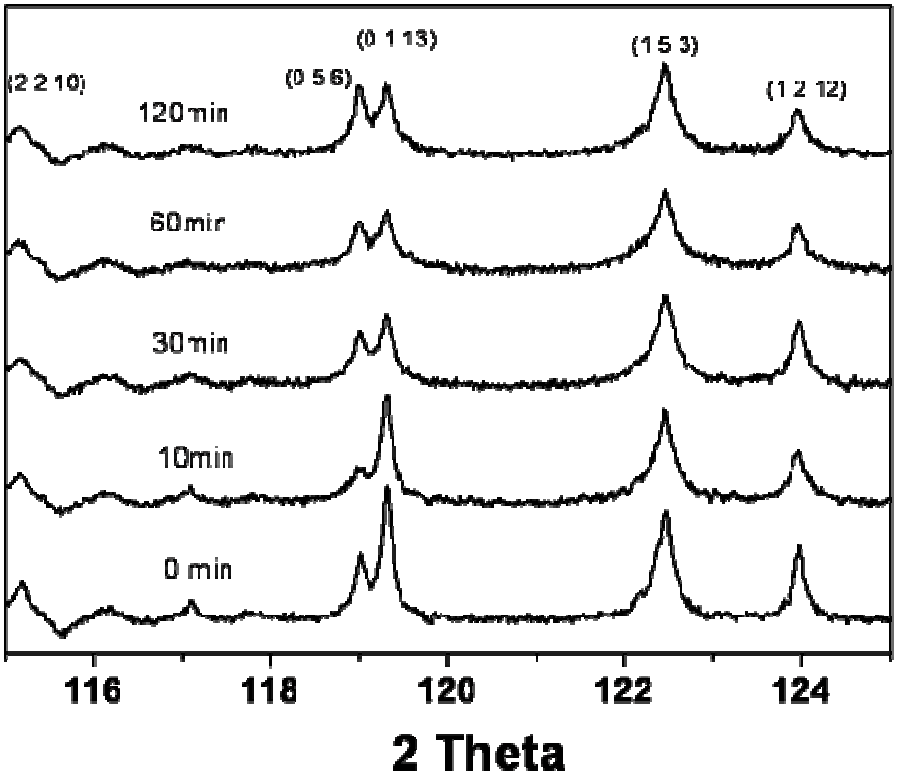

Fig. 4-15 High angle diffraction pattern of milled $Ba_5Nb_4O_{15}$

doi:10.6342/NTU201702760

4.4 Discussion

4.4.1. Milling behavior of $Ba_5Nb_4O_{15}$: Barium dissociated from lattice site

$Ba_5Nb_4O_{15}$ calcined powders are easily pulverized through wet mechanical treatment. The initial mean size 2.52um particles can be grinded to 0.44um by the planetary mill. In the beginning, powder distribution is bimodal population and tends to Gaussian normal distribution after grinding. Deducing energy and particle reduction size can roughly calculate the relation of milling time and particle mean size.

$$\kappa \times (1/d_2 - 1/d_1) = \text{Energy (media mass} \times \text{rotation speed} \times \text{milling time)} \cdots\cdots\cdots (4.1)$$

κ : Rittinger's coefficient $1/d_1$: before size reduction $1/d_2$: after size reduction

The equation 4.1 following Rittinger's law[85] is the energy applying on particle. It is proportional to the change of surface area between primary and final reduction particle. Fig. 4-16. The line between milling time and reciprocal of reduction size have linear relevance by fine grinding process. Mechanical energy obviously changes particle surface area. Through the use of grinding media yttrium stabilized zirconia, less contamination contributed on the milled powders. The zirconia contamination is lower than 500ppm at milling 120min confirmed by XRF analyzer.

Intensive milling apparently induces more surface area of particle[86]. The new surface of particle can weaken the valence bond of barium atom and tend to react to H_2O. Only barium ions were detected quantitatively from filtered water of milled slurry. There are no free niobium ions detected by ICP analyzer. Which certain barium ion in unit cell of lattice structure is easily dissociated? Is it implied to the preferred orientation plane growth? The SAED method by HR-TEM will give the evidence on crystallographic observation. It will be explained next section. Continuously, the barium ions react to water and convert into barium hydroxide. The carbonic acid from CO_2 entering into water neutralized with barium hydroxide to form $BaCO_3$. The evidence on

doi:10.6342/NTU201702760

typical orthorhombic structure of $BaCO_3$ is also verified from X-ray diffraction pattern. SEM morphology of $BaCO_3$ illustrates the recrystallization of precipitated product to accomplish needle-like shape[81,87]. This study on milling process indicated more weight loss from dissociation of $BaCO_3$ at elevated temperature 1435ºC. The milling time have relatively physical quantity on weight loss of sintered $Ba_5Nb_4O_{15}$. It is also accordant with surface area generated by mechanical energy. The weight loss of 0.44um $Ba_5Nb_4O_{15}$ is near to 1.0wt.% at sintering 1435ºC. All routes of milled $Ba_5Nb_4O_{15}$ results prove the fundamental mechanochemical phenomena which barium ions leach into water through applying mechanical energy.

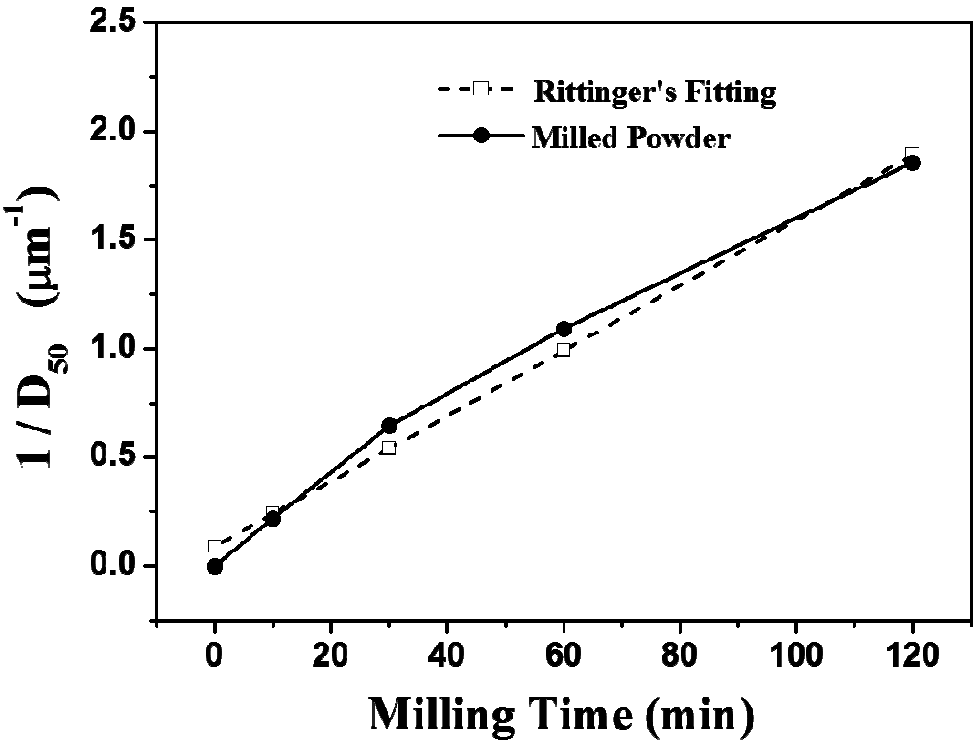

Fig. 4-16 Rittinger's Law correlation fitting curve of milled $Ba_5Nb_4O_{15}$ powders

doi:10.6342/NTU201702760

4.4.2 Microstructure vs. Composition

To verify the microstructure anisotropic growth may be caused by precipitated $BaCO_3$ which never left out of specimen, an analogical experiment proposed as flow chart in Fig. 4-17. The purpose of experiment confirms anisotropic growth on the preferred orientation plane possibly. Due to $BaCO_3$ precipitate around the milled powders, it could be not homogenously in the powders when water evaporated at drying process. The fine needle shape $BaCO_3$ aggregates to cause composition variation. There is a difference on microstructure of the rich $BaCO_3$ site compared with others. A simple method designed to create the $BaCO_3$ composition gradient on green pellet of un-milled $Ba_5Nb_4O_{15}$. Small amount of $BaCO_3$ powders put on surface of $Ba_5Nb_4O_{15}$ then co-firing at 1435ºC. It is an interface of BaO-$Ba_5Nb_4O_{15}$ as to be none equilibrium mass transport happened from top of disc. The reference one is green pellet without extra $BaCO_3$ on surface as usual.

Microstructure of the cross section of sintered specimens express grain shape and size are distinct near to the free surface. Fig 4-18 (a)&(b). The grain growth may adopt a preferred direction along with composition gradient. On the top of free surface complies with rich $BaCO_3$ powder like as source of barium rich ingredient. The depth of diffusion path will be decided by composition gradient. When barium rich like as precipitated source from milling process, the sintered specimen feature has the tendency to be high aspect ratio. The elongated grains change aspect ratio from high to low beneath 100um depth. Although, this method roughly described the grain shape and direction may be relevant to preferred orientation property. Leaching barium ions will reentry into lattice site but inhomogeneous composition plays the role of anisotropic growth. The macroscopic investigation still let the proof of preferred orientation grain growth is believable.

doi:10.6342/NTU201702760

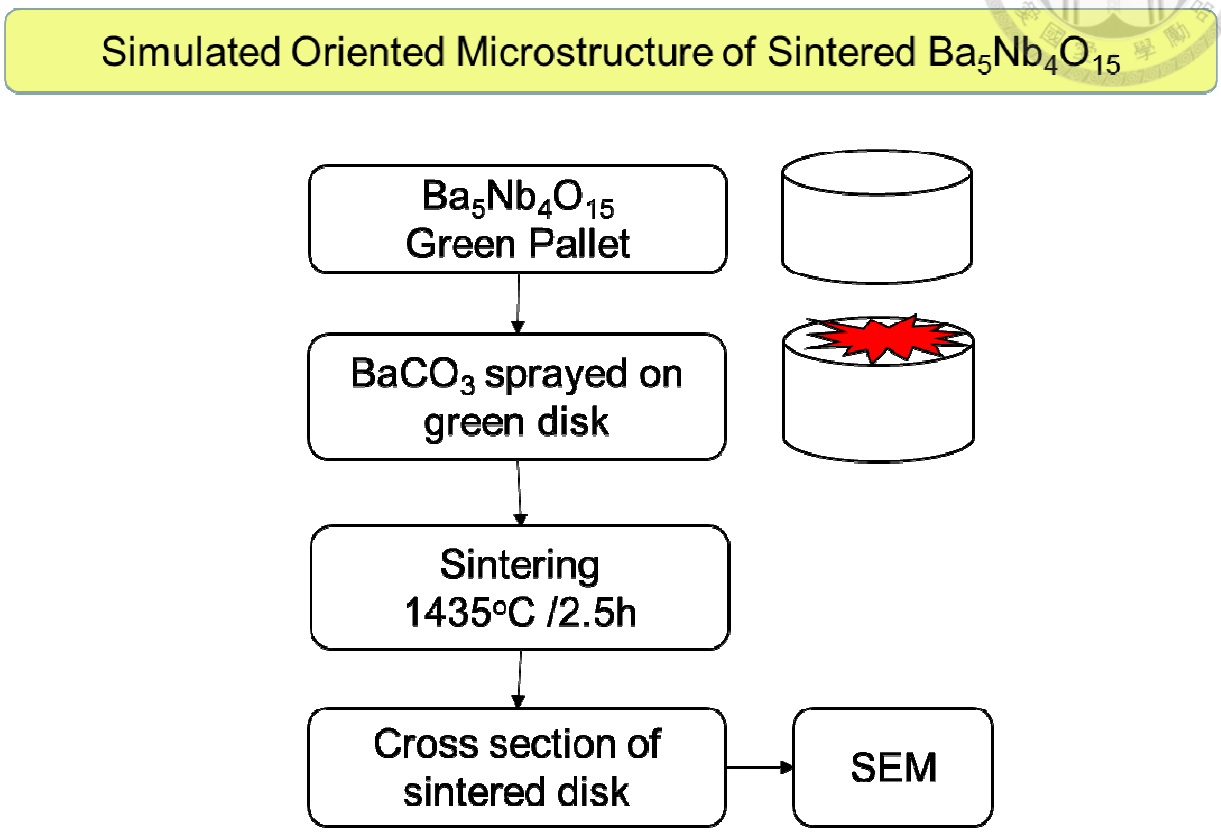

Fig. 4-17 Simulated anisotropic growth by composition variation

doi:10.6342/NTU201702760

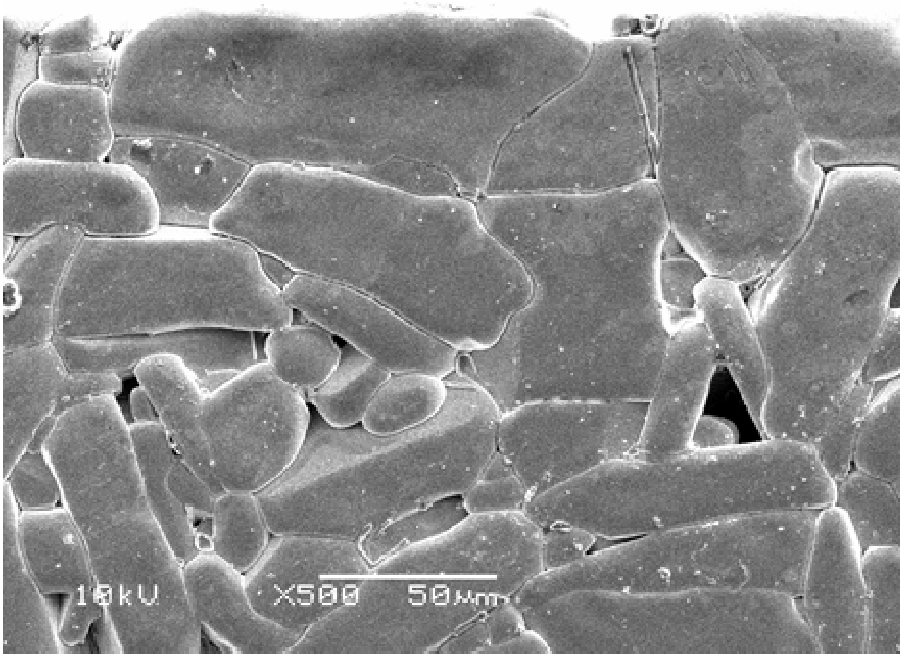

Fig. 4-18 (a) SEM micrographs for the $Ba_5Nb_4O_{15}$ sintered at 1435 °C. The cross section from the top of sintered surface reveal specific growing plane without excess $BaCO_3$

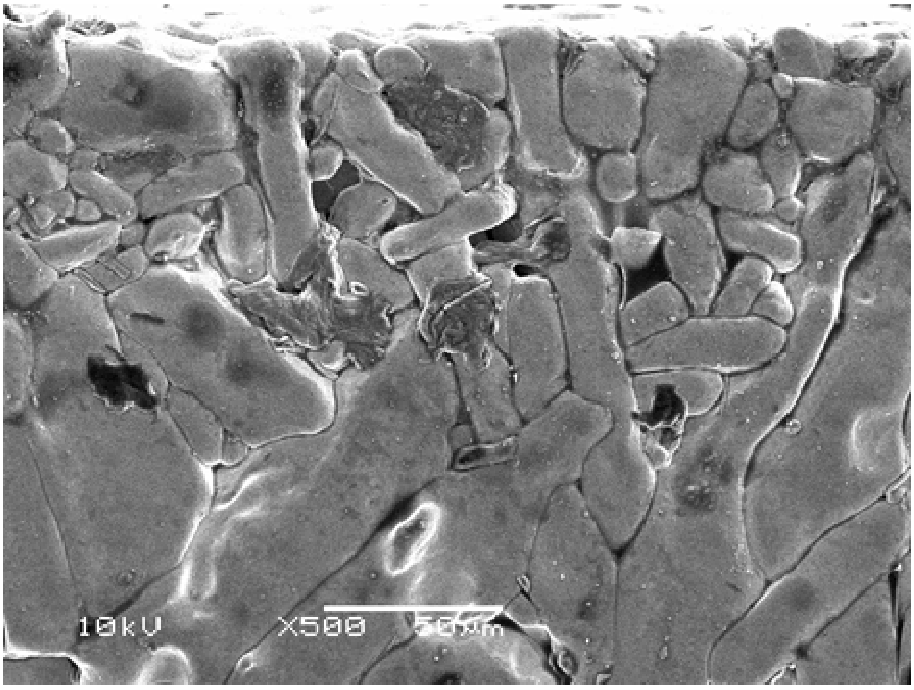

Fig. 4-18 (b) SEM micrographs for the $Ba_5Nb_4O_{15}$ sintered at 1435 °C. The cross section from the top of sintered surface reveal specific growing plane with excess $BaCO_3$

doi:10.6342/NTU201702760

4.4.3 Preferred orientation plane by XRD pole figure identification

In addition, the study on anisotropic grain growth of $Ba_5Nb_4O_{15}$ reveal to microstructure varied with milling time. The elongated grains present the orientation was always observed in-plane direction. Not only it is derived from the presence of liquid phase assisting coarsening but also the precipitated substance engaged the preferred orientation growth. Firstly, the aspect ratio of $Ba_5Nb_4O_{15}$ grain is enhanced by milling energy. Intensive milling time appears to enlarge aspect ratio of grains. More milling time induces the excess surface energy and leaching barium ions assist the lattice diffusion on a certain plane. Tanaka's[88] theoretically investigated on the basis of free energy for material transport proved higher rate of shape change for elongated grains. The derived rate equations are worked on considering lattice diffusion mechanism. It can be carried out the shape change from precipitated $BaCO_3$ with the milled $Ba_5Nb_4O_{15}$ powders as the starting none equilibrium system. The rate of shape change is proportion to the surface energy generated from milled $Ba_5Nb_4O_{15}$ and inverse proportion to the particle size.

Before the pole figure analysis on specimens, the Laue's XRD back reflection pattern gives the textural structure information on both samples show disconnected spots at each diffracted ring pattern. Fig 4-19 (a). An interested pattern comparison on 38.3° and 42.7° reversed deviation of intensity after milling treatment. Another approach on this particular 2θ angle 38.3° by phi rocking scan with two dimensional HR-XRD Fig. 4-19 (b), milled specimen has the appearance of intensity spectrum to be preferred orientation plane. Finally, selected planes of (1 0 3) (1 1 0) (0 0 5) (2 0 3) were fully scanned by 2D measurement to be an information of stereographic projection. Fig. 4-19 (c) express the variation of diffracted intensity with respect to the direction of planes. The multipole random distribution reveals its probability of density for each plane, (0 0 5) provides the preferred orientation plane message on pole figures comparison.

doi:10.6342/NTU201702760

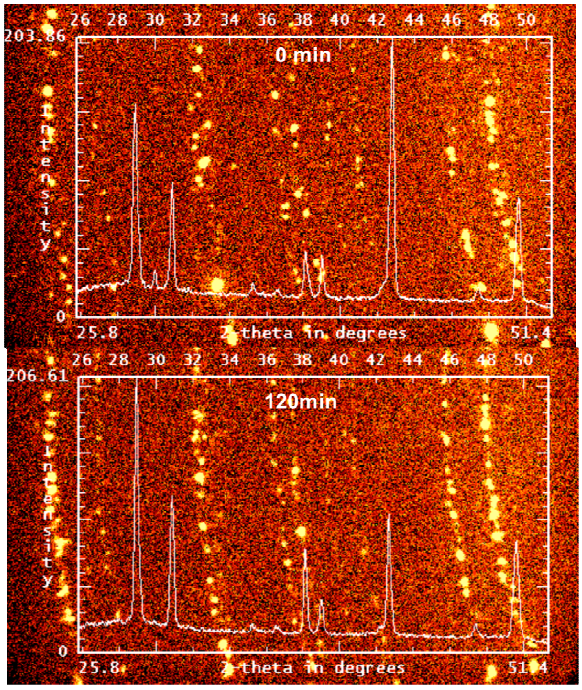

Fig. 4-19 (a) Comparison of Laue's diffraction patterns of sintered specimen milled 120min

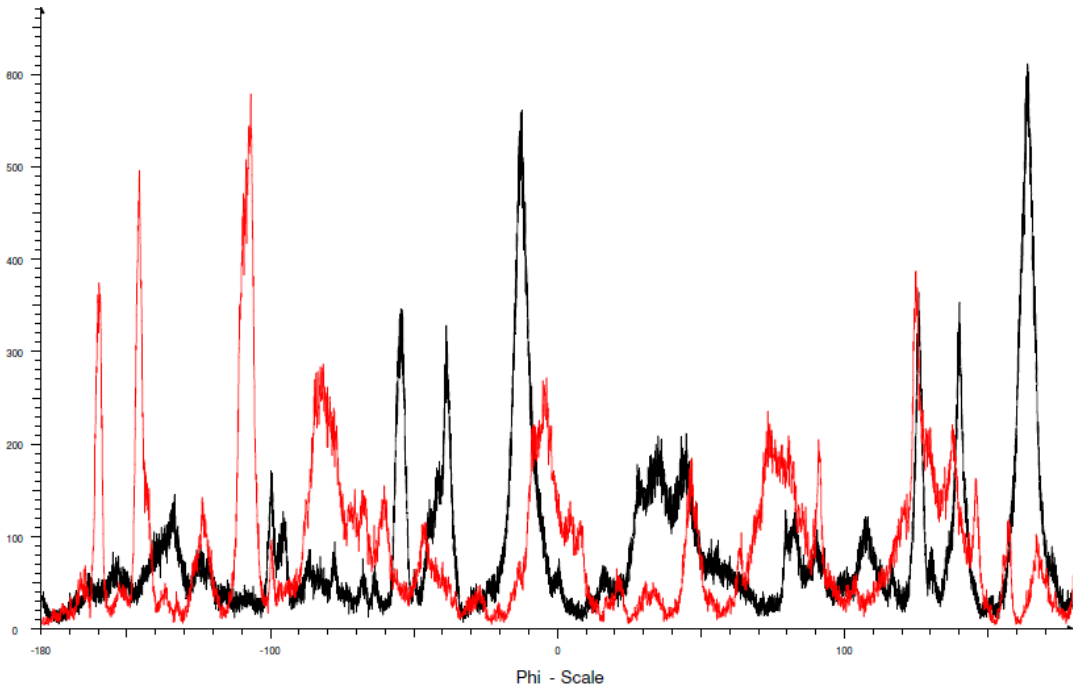

Fig. 4-19 (b) Comparison of sintered specimen at 1435°C line scans at 2θ angle at 38.15° (red: un-milled black: milling 120min)

doi:10.6342/NTU201702760

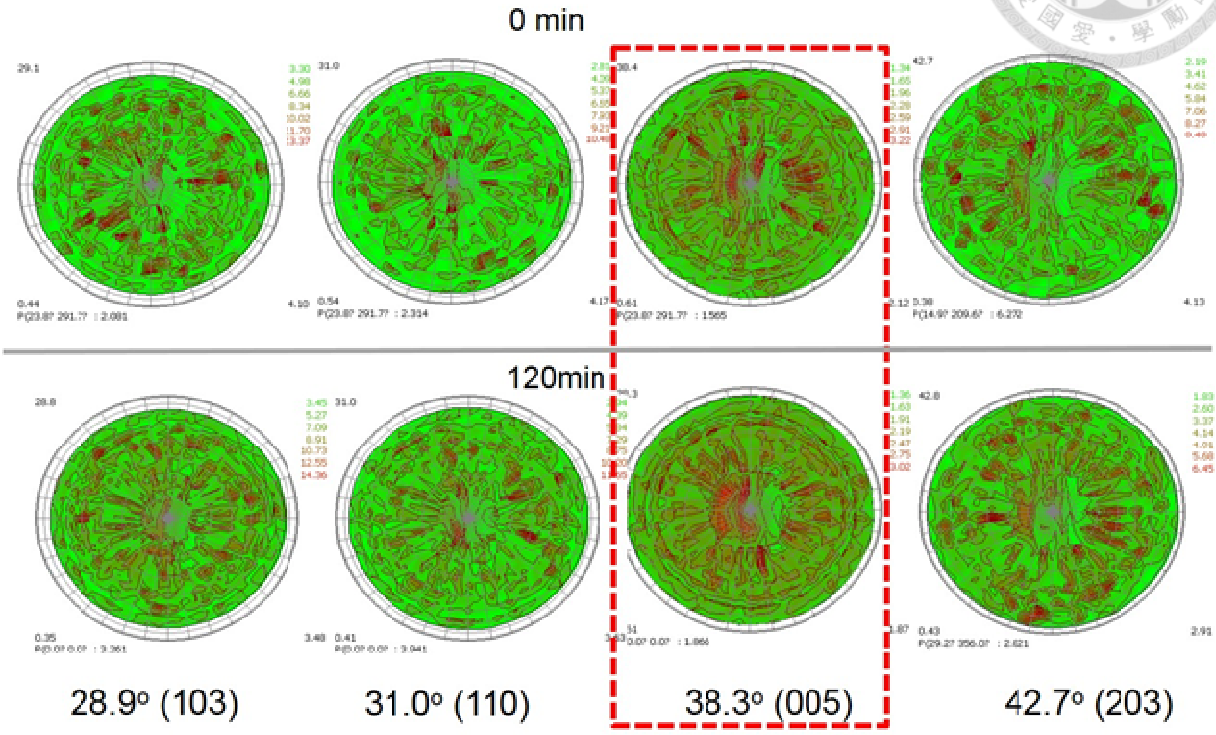

Fig. 4-19 (c) Pole figure of mill and unmill $Ba_5Nb_4O_{15}$ with sintering at 1435°C

doi:10.6342/NTU201702760

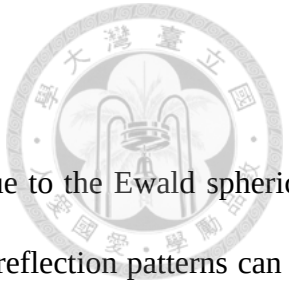

4.4.4 TEM lattice plane identification

There is a main difference between X-ray and electron diffraction due to the Ewald spherical radius that is related to wavelength of incident wave. Which means more reflection patterns can be observed by electron diffraction. The interaction by Coulomb force between electron and matter is much stronger than X-ray. This indication of scattering wave can shorter the exposure time to get high intensity. Even though the structure determination is not reliable than XRD data, but tilting the specimen along a direction to investigate the crystallographic orientation can be achieved by Selected Area Electron Diffraction SAED and/or Convergent Beam Electron Diffraction CBED in nm-region area.

Fig. 4-20 Bright field image of un-milled $Ba_5Nb_4O_{15}$ specimen at elevated temperature 1350°C The orientation plane is parallel with grain boundary investigated by bright field image of high resolution TEM. The SAED pattern for this region proved the plane index meet the reciprocal distance of (0 0 1) and unit cell of lattice constant in c-axis is 1.181nm. The orthogonal plane meets to (1 0 0) has 0.592nm lattice constant in axis. Another specimen at elevated temperature 1435°C can be found the same orientated plane parallel with grain boundary Fig 4-21. SAED pattern proved the plane direction is perpendicular to grain boundary and growing direction is [1 0 0]. Lattice constant of (0 0 1) is 1.191nm measured from reciprocal distance of SAED pattern. It is little large one according as lattice parameter increase with sintering temperature rule. Fig. 4-22. High resolution image with high magnification illustrates the 5 layers stacking lattice sequentially from observing at zone axis [1 1 0] direction. Fast Fourier Transform obtained the same information on the selected area as SAED pattern. SAED pattern also reveals the 5 spoty intensity repeating the shift type packing status such as sequence of $[ACABC]_n$ or $(hhccc)_n$ in crystallographic structure[89].

The milled $Ba_5Nb_4O_{15}$ sample with preferred planes was confirmed the grain by FIB tool. SEM

doi:10.6342/NTU201702760

pictures in Fig 4-23 state the selected area and trapped pores as same as previous study on de-sintering behaviour at high sintering temperature. No doubt, the preferred orientation plane along the grain boundary is (0 0 1) verified by SAED and bright field high resolution image. The two selected sites on one grain show the same orientation plane guide to top surface of specimen. The growth direction on plane (0 0 1) is [1 0 0] which can be imaged to the corner of lattice site. Leaching barium is split out from the weakest bond at the niobium deficient layer. The vacancy mobility is much fast than lattice site. From macroscopic point of view, composition gradient of barium also enhances the anisotropic growth. The new lattice distance derived from SAED pattern of milled specimen. The d spacing of orientated plane is 1.201nm and axis distance is 0.5915nm which is obviously larger than un-milled specimen. The c-axis is enlarged around 0.8% compared to un-milled one. The lattice distorted by FIB ion higher bombarding energy[90].

doi:10.6342/NTU201702760

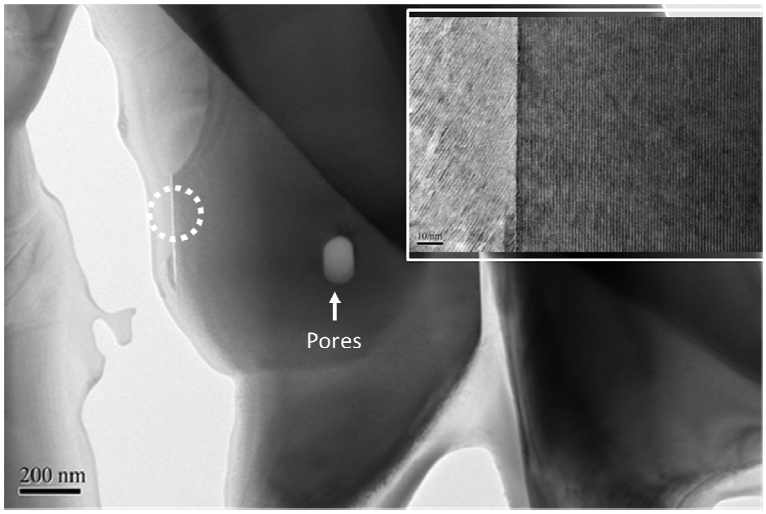

Fig. 4-20 (a) Bright field image of un-milled specimen at 1350°C

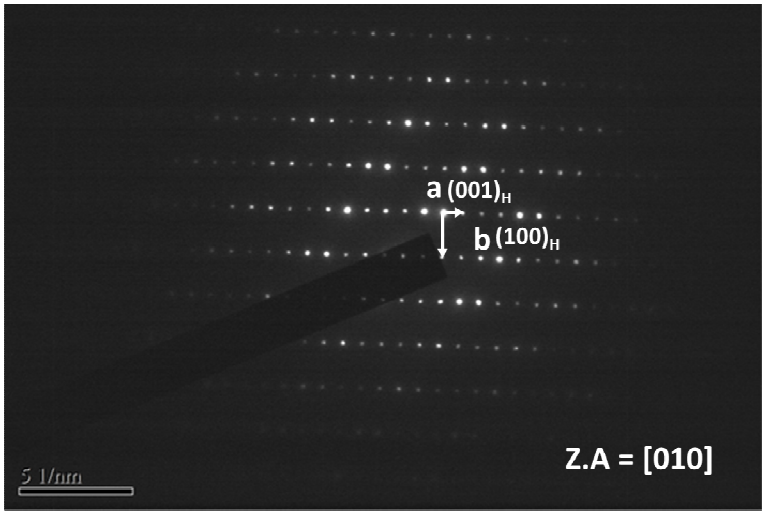

Fig. 4-20 (b) SAED pattern of un-milled specimen at 1350°C

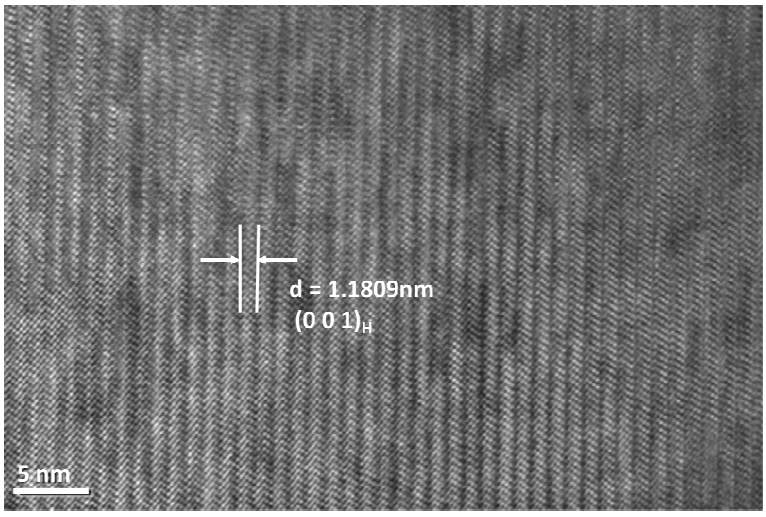

Fig. 4-20 (c) HRTEM Bright field image of un-milled specimen at 1350°C

doi:10.6342/NTU201702760

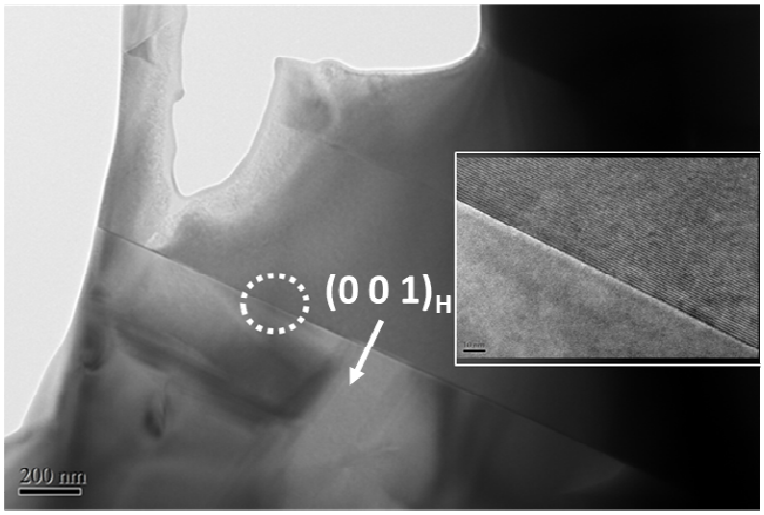

Fig. 4-21 (a) Bright field image of un-milled specimen at 1435°C

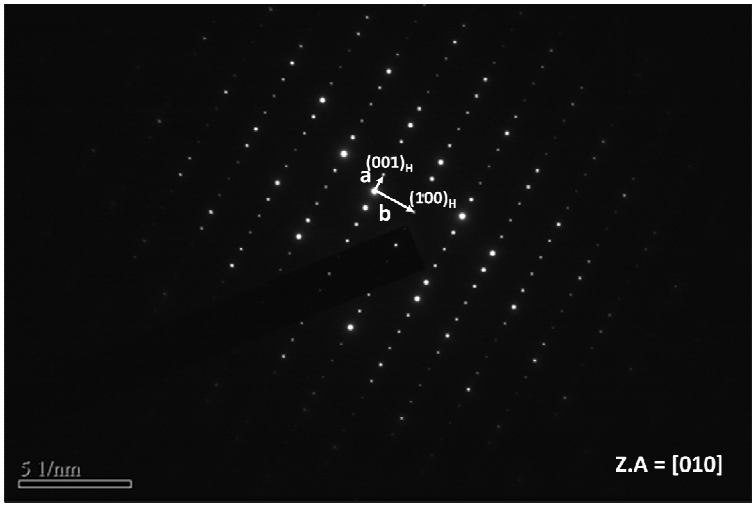

Fig. 4-21 (b) SAED pattern of un-milled specimen at 1435°C

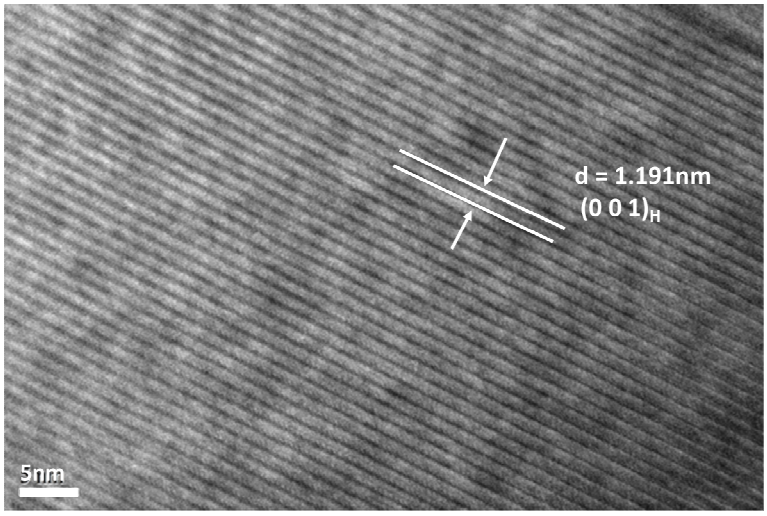

Fig. 4-21 (c) HRTEM Bright field image of un-milled specimen at 1435°C

doi:10.6342/NTU201702760

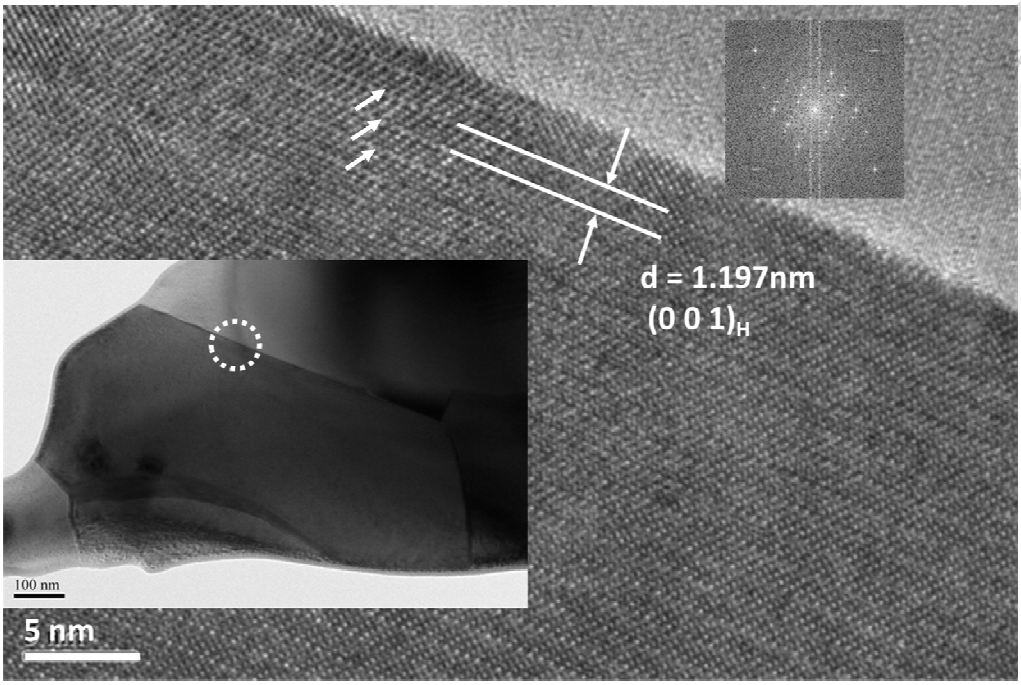

Fig. 4-22 (a) Bright field image of ion milled specimen at 1435°C

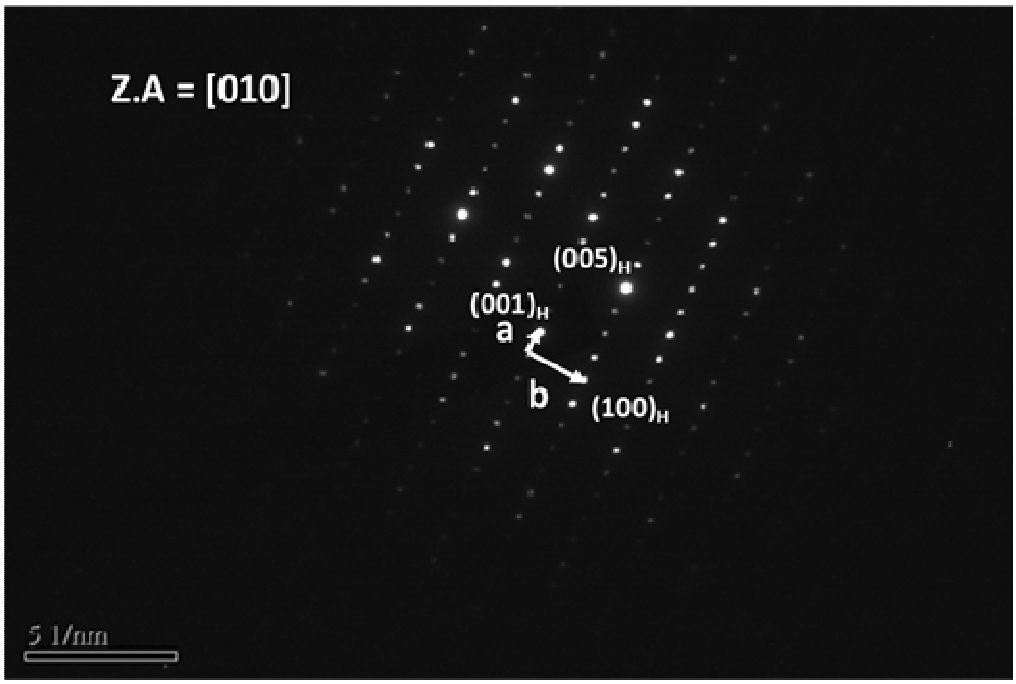

Fig. 4-22 (b) SAED pattern of ion milled specimen at 1435°C

doi:10.6342/NTU201702760

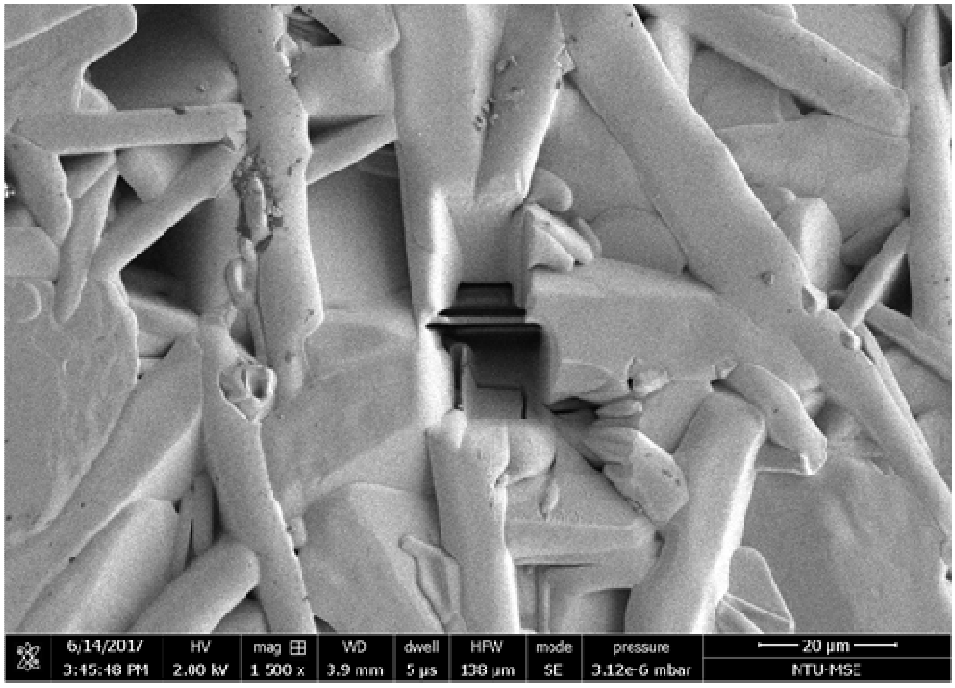

Fig. 4-23 (a) FIB preparation for milled 120min specimen at 1435°C

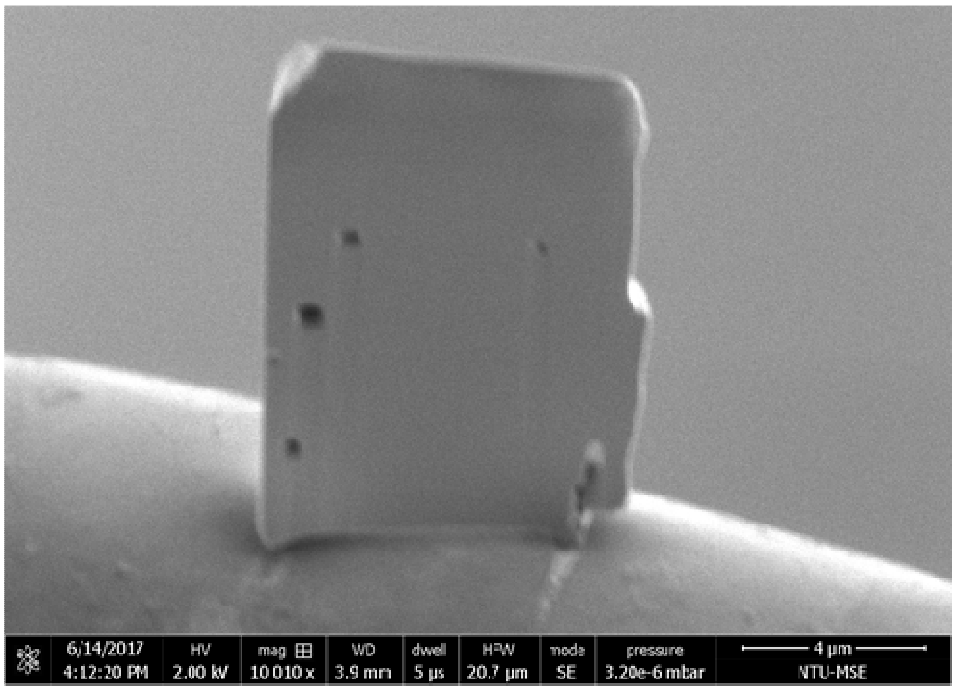

Fig. 4-23 (b) FIB preparation for milled 120min specimen at 1435°C

doi:10.6342/NTU201702760

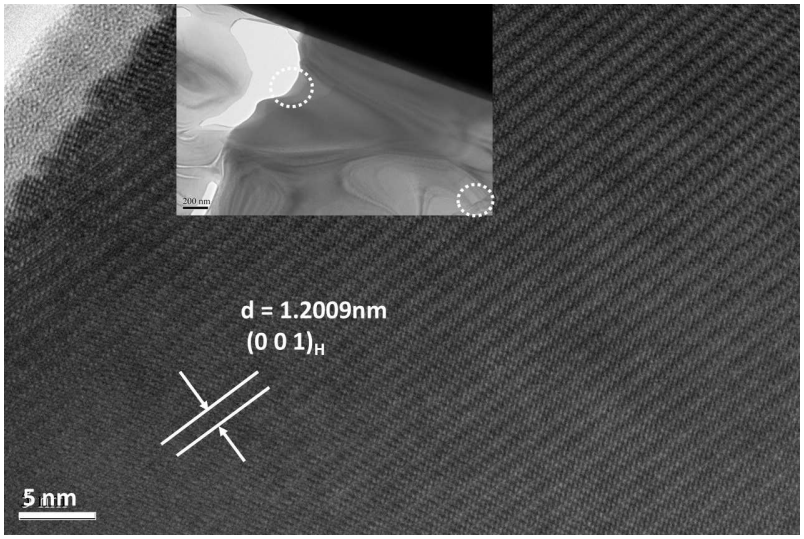

Fig. 4-24 (a) Bright field image of specimen is milling for 2h and sintered at 1435°C

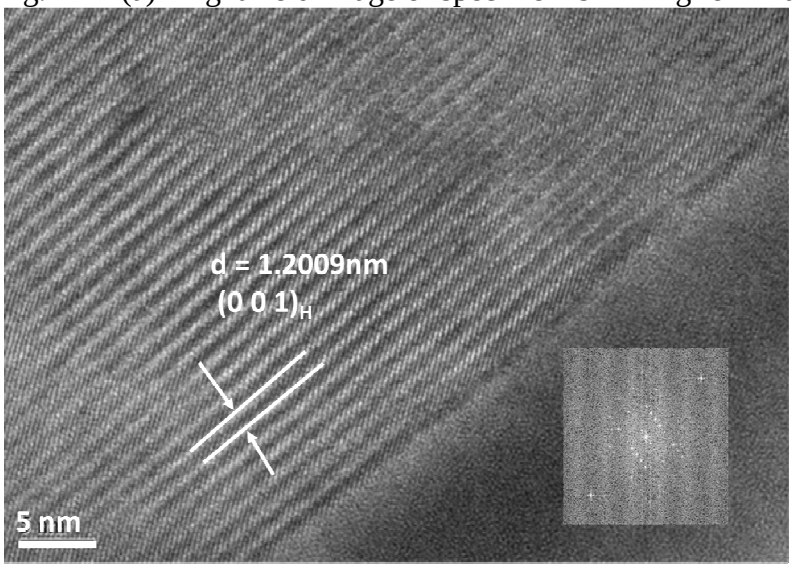

Fig. 4-24 (b) HRTEM Bright field image of specimen is milling for 2 h and sintered at 1435°C

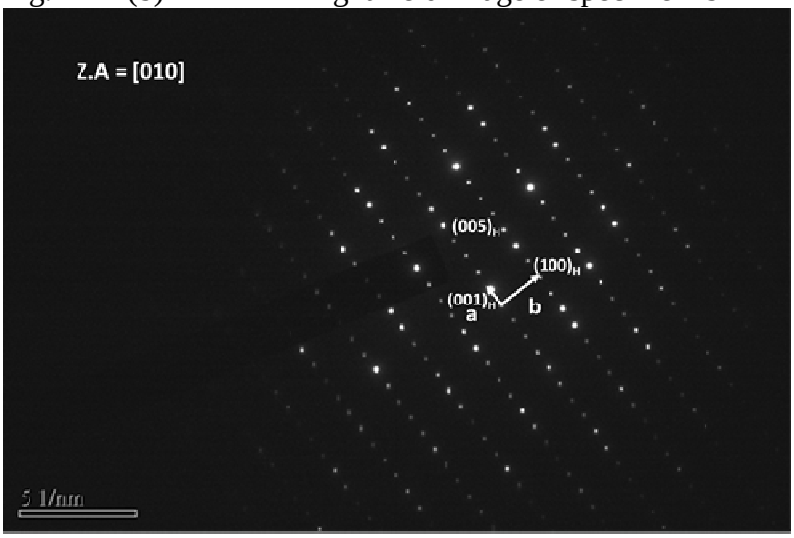

Fig. 4-24 (c) SAED pattern of specimen is milling for 2 h and sintered at 1435°C

doi:10.6342/NTU201702760

4.4.5 Preferred orientation plane by EBSD identification

EBSD is a very sensitive to crystal orientation tool to identify the preferred orientation plane for most materials. On the other hands, the grain size, boundary misorientation, phase identification and texture structure may be analyzed[91-92]. The analysis area was selected 200μmX300μm under SEM microscopic observation Fig 4-25. The band contrast map Fig 4-26 derived from Hough transform proved the specimen supporting the image quality factor in the EBSP. A digitized contrast of the Kikuchi band intensity is available for images show the microstructure in a qualitative simulation.

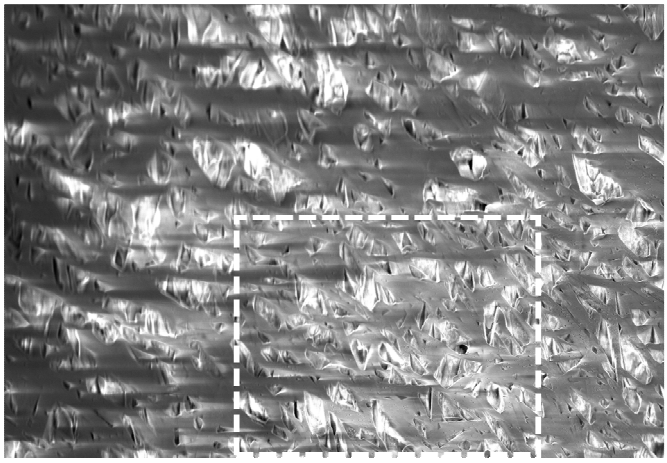

Fig. 4-25 High tilt angle at 70º for EBSD analysis

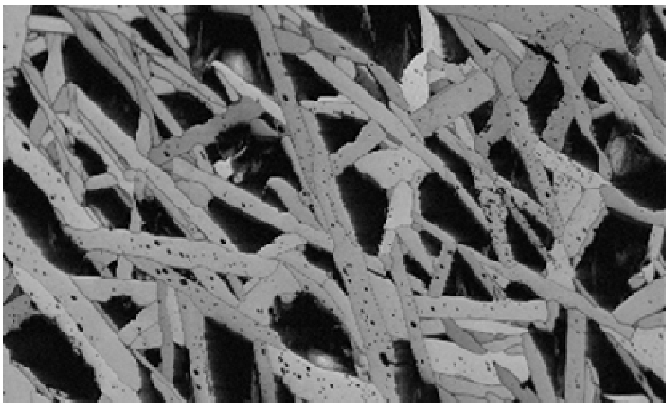

Fig. 4-26 Band contrast of selected area 300μmX200μm

doi:10.6342/NTU201702760

Data acquiring from HKL software processing to simulate the grain shape and orientation. The inverse pole figure Fig.4-27 based on the band contract configuration verify the plane direction by colour mapping. There is a plane direction in <0 0 1> has possibility density high than others. A well said on the textural orientation direction is from the triangle IPF at Y direction.

Euler map can describe the sample orientation relative to its specific orientation crystal. The contour pole figure in Fig 4-28 shows strongly textural component on {0 0 1} plane.[93]

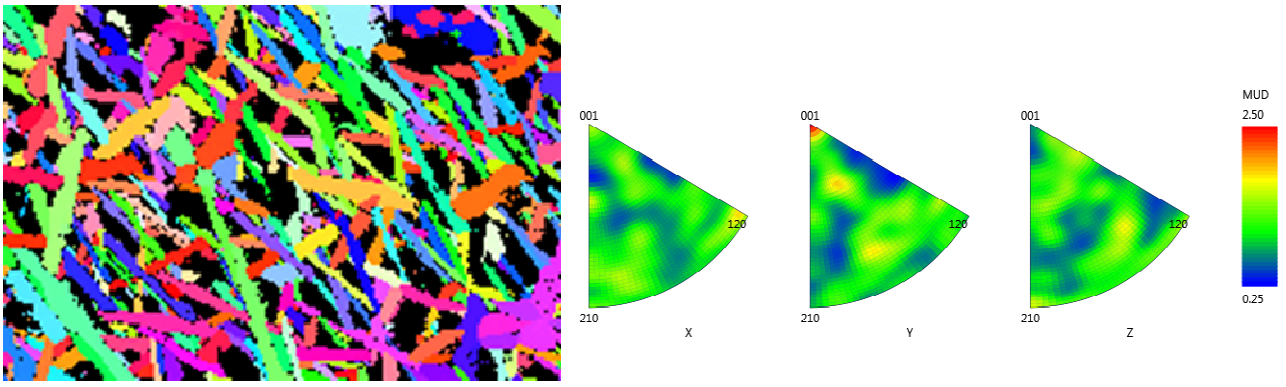

Fig. 4-27 IPF mapping of milled specimen

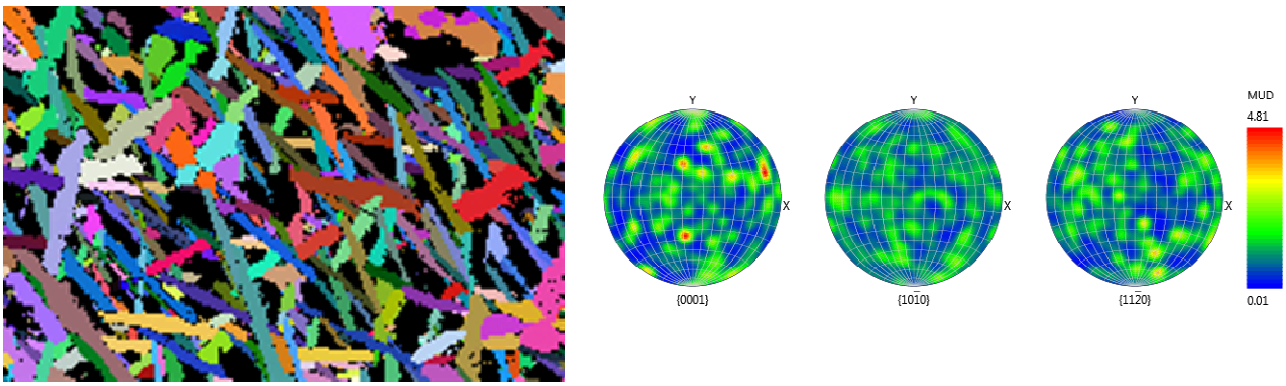

Fig. 4-28 Euler Mapping of milled specimen

doi:10.6342/NTU201702760

4.4.6 Microwave characteristic of milled $Ba_5Nb_4O_{15}$

The mechanochemical behavior of a cation-deficient perovskite, $Ba_5Nb_4O_{15}$, is investigated in the present study. The maximum quality factor can be achieved without mechanical treatment is higher than 40,000. After milling, the precipitated $BaCO_3$ from water base slurry affect the ceramic to a density decrease, quality factor degradation at a sintering temperature 1435°C. Such excess substance is formed by the leaching of barium ion and reduction with carbonic ion. Through high angle X-ray diffraction verify the degree of ordering structure, (0 1 13) plane of $Ba_5Nb_4O_{15}$ crystal structure declined. The quality factor shows a strong dependence on the mechanical treatment in the hexagonal perovskite structure.

In general, the majority variation factors on the permittivity are affected by internal pores or second phase of ceramic extrinsically. More porosity of $Ba_5Nb_4O_{15}$ ceramic is produced via exhausting CO_2 from precipitated $BaCO_3$. The segregated composition tends to Ba-rich free energy reduce diffusivity at high temperature. The more gradient composition from precipitated $BaCO_3$ effects sintering density. And the presence of sintered density decreased as increasing milling time. Finally, sintered density determined the fluctuant permittivity of $Ba_5Nb_4O_{15}$. It can be comprehended the permittivity value of milled specimens declined from 35 to 30. Less impurity came from milling media zirconia oxide did not affect the composition and temperature coefficient of resonated frequency still kept the same level. Table 4-3.

However, the variation study on quality factor of microwave ceramic strongly depend specific crystalline planes[94], especially on the high Miller indices planes which are arranged within short range ordering structure. The Q×*f* quality factor sustains at highest value over 40,000 without mechanical treatment applied on $Ba_5Nb_4O_{15}$. More mechanical treatment time transmits to shear stress decrease the crystal size significantly as remaining strain to the powders. Meanwhile, free

doi:10.6342/NTU201702760

barium ions leave out the lattice site splitting H_2O catalyzed by mechanical energy. The specific plane of $Ba_5Nb_4O_{15}$ is hard to fully recover from the same thermal energy at sintering temperature 1435°C. It means the intrinsic defect energy and residual strain energy will reduce the ordering structure. The quality factor declined dramatically one and half of initial value and said lack of the (0 1 13) plane at 119.3° achieve to ordering structure.

High indices plane is always the trace plane to verify the quality factor performance of $Ba_5Nb_4O_{15}$ ceramic. It can be achieved to high ordering structure via extreme driving force from temperature、time and pressure. Through mechanical treatment on it, the sintering energy limits the presence of specific ordering plane. The barium ions exit from collapse of (0 0 c) plane and create defect energy. The new interface of $BaCO_3$-$Ba_5Nb_4O_{15}$ provides a higher surface energy. Finally, the sintering profile can't manipulate fully ordering plane as primary degree.

Table 4.3 Temperature coefficient of resonated frequency at different milling time

Milling time / min	Relative Density (%)	Permittivity	τf (ppm/K)
0	86.8±0.3	35.0±0.1	49.9
10	80.2±0.5	32.1±0.2	50.8
30	79.2±0.9	31.7±0.3	56.8
60	74.8±3.1	30.3±0.8	62.3
120	75.5±1.1	30.6±0.5	48.0

doi:10.6342/NTU201702760

4.5 Conclusion

The present study demonstrates that the chemical interaction during milling plays an important role on the performance of ceramic products. The mechanical forces applied by the milling media (ZrO_2 balls) generate a lot of fresh surface. More barium ion can then be released due to the increase of surface area. Precipitated $BaCO_3$ is formed from the reaction with carbonic acid in water. The orientated microstructure indicates the preferred plane is $(0\ 0\ 1)_H$ which coincides to anisotropic growth direction. Excessive milling time may bring more barium ions leave out the lattice sites and exhibit the orientated growth. The microwave properties of $Ba_5Nb_4O_{15}$ perovskite depend strongly on its density and crystalline structure. Measured permittivity can be predicted by volume ratio between pores and dielectric. The intensity of $(0\ 1\ 13)_H$ plane indicates the quality factor performance.

To avoid excessive milling time may benefit its microwave performance. Several implications can be drawn from the present study.

1. Chemical interaction during milling plays an important role on the performance of ceramic products. Though the solubility of ceramic in water is usually low, the release of a minute amount of ions during milling may affect the performance significantly.
2. Many barium-containing perovskites are widely used as microwave dielectrics, such as barium titanate, barium strontium titanate, etc. The cation ratio for these dielectrics affects their performance significantly. These barium-containing perovskites many also release barium ion during milling. It is worth noting such chemical aspect of the milling process

doi:10.6342/NTU201702760

Chapter 5: Liquid Phase Sintering of $Ba_5Nb_4O_{15}$

5.1 Introduction

For the applications of LTCC technology[95-96], the candidate material $Ba_5Nb_4O_{15}$ is a hexagonal perovskite compound ceramic. It has been commercialized with additives (Table 5-1). Many studies on $Ba_5Nb_4O_{15}$ material system focused on glass additives to reduce its sintering temperature through the assistance of liquid phase. The co-firing of dielectric and conductive metal was investigated commercialization before action. It was acknowledged that $Ba_5Nb_4O_{15}$ was to be sintered at lower temperature by adding a small amount of B_2O_3, CuO or other kinds of additives[97-98]. The sintering temperature was dramatically reduced by 400^oC by adding liquid phase sintering aids. Low firing $Ba_5Nb_4O_{15}$ material can be used to cofire with silver electrode. To verify the silver migration and the degradation on electrical property, the amount of liquid phase is limited[99].

doi:10.6342/NTU201702760

Table 5-1 List of LTCC high permittivity microwave dielectric materials for LTCC

Material	Sintering	ε_r	Q*f (GHz)	f (GHz)	Tcf (ppm/
$Ba_5Nb_4O_{15}$	1380	39.0	23700	4.73	78
$Ba_5Nb_4O_{15}$ +3 wt%B_2O_3	925/2h	39.0	18700		0
$Ca[(Li_{1/3}Nb_{2/3})_{0.8}Ti_{0.2}]O_{3-d}$	920	40.0	20500	8	4.7
$Ca[(Li_{1/3}Nb_{2/3})_{0.8}Ti_{0.2}]O_{3-d}$ + 12 wt% B_2O_3-ZnO-SiO_2-PbO frit glass	900	40.0	12500		-8
$BiNb_{0.6}Sb_{.4}O_4$	920	40.7	9500		-31
$(Tl_{.8}Sn_{.2})Te_3O_8$	700/5h	41.0	22000	4	
0.9$BiNbO_4$-0.12$ZnNb_2O_6$+1.2wt% CuV_2O_6	850	41.0	28120		4
$BiNbO_4$	875	43.0	15700	4.3	38
$BiNbO_4$ +0.5wt%CuO	900	43.3	13000	6.3	15
$Bi_{0.99}La_{0.01}NbO_4$	920	43.4	10600	7	-2

doi:10.6342/NTU201702760

5.2 Experimental method

5.2.1 Raw material preparation

The synthesized $Ba_5Nb_4O_{15}$ powder with stoichiometric mole ratio 5.0:2.0 was used to prepare. For CuO 0.5~1.5wt% and/or B_2O_3 with purity higher than 99.9% are used. The media were 2mm yttrium stabilized zirconia balls. All ingredients mixed with distill water were pulverized by 220rpm planetary mill for 30min. The formulated powders were treated 0.75um.

To investigate co-firing with metal silver, the multilayered samples were prepared by the lab-scaled facilities, including casting machine, printing machine, cold isostatic pressure and cutting machine. A slurry was prepared by mixing with ceramic powders, PVB binder and toluene/alcohol solvent vehicles. The thickness of the green tape was 30um. Pure Ag paste were printed on ceramic foil, then stacked 3 layers in dimension of 3.6 mm length and 1.8 mm width.

5.2.2 Experimental flow chart and procedure

The formulated powders were measured by laser diffraction type particle size analyzer (LA-920, Horiba Co., Japan). After drying, all milled powders granulated with 4wt% PVA binder were formed 10mm diameter cylinder type samples. They were sintered at elevated temperature 900°C with soaking time 4.0h. Sintering density of specimens were measured by Archimedes method. To measure the permittivity and dissipated factor, the top and bottom of sintered body were metallized by silver paste and curing at 800^{o}C with 10min. All dielectric properties at 1MHz low frequency were analyzed by L.C.R meter (HP-4285B, Agilent Co., U.S.A). Permittivity value and

doi:10.6342/NTU201702760

quality factor of each $Ba_5Nb_4O_{15}$ ceramic specimen at high frequency were measured by Krupka's cavity resonated method. The apparatus was constructed with a network analyzer (HP-8720ET, Agilent Co., USA) to measure $TE_{01\delta}$ resonant mode of cylindrical samples.

To observe the multilayer samples which was co-cofired with silver paste, the sintered chip was mounted into epoxy resin, sectioned and polished. The area near to inner electrode was measured silver content to identify migration depth quantitively by EPMA (JAMP 9510F, JEOL Co., Japan). Meanwhile the microstructure of low temperature sintered $Ba_5Nb_4O_{15}$ specimen was observed on free surface and fracture surface conducted with scanning electron microscopy (JSM-6360, JEOL Co., Japan).

In this study, milling effect from mechanochemical interaction of low firing $Ba_5Nb_4O_{15}$ were also verified. Precipitated $BaCO_3$ can be identified and decarbonated temperature were verified by TGA (TG-DTA2000, MAC Science Co., Japan). The thermal mechanical properties of sintered $Ba_5Nb_4O_{15}$ was analyzed by TMA (DL2000, MAC Science Co., Japan). All the experimental procedure is illustrated in Fig. 5-1.

doi:10.6342/NTU201702760

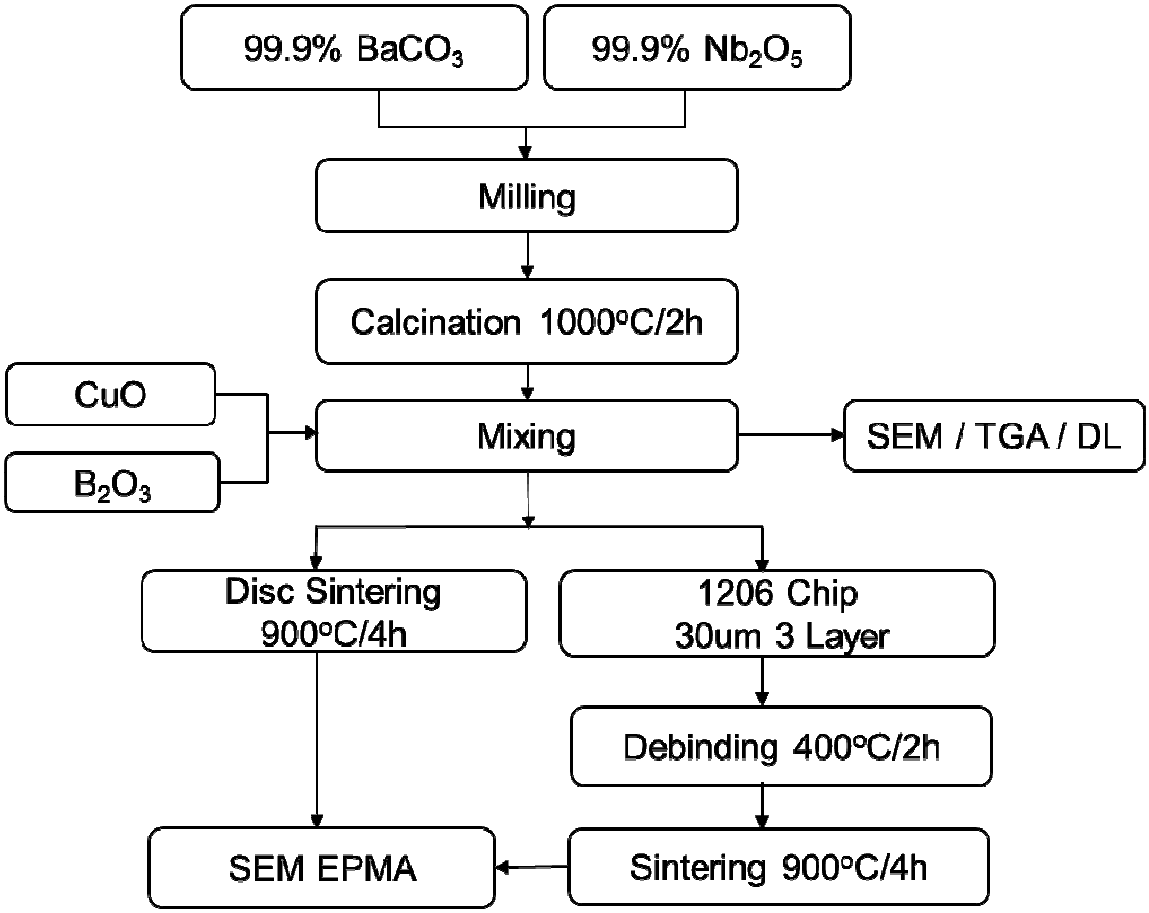

Fig. 5-1 Experimental Flow Chart

doi:10.6342/NTU201702760

5.3 Result and Discussion

5.3.1 CuO and B_2O_3 sintering additives

Fig. 5-2 shows the density as a function of milling time. The $Ba_5Nb_4O_{15}$ with a small amount of CuO and B_2O_3 can be sintered under 900°C/4h condition. The relative density reaches 93% and sintered ceramic exhibits a dense microstructure. It is similar to D.W Kim's research on low firing additives for $Ba_5Nb_4O_{15}$.[100] The small amount of B_2O_3 and CuO enabled to reduce the sintering temperature by 400°C to lower than 900°C. This dramatical energy reduction was contributed by chemical gradient that interfacial free energy of CuO and B_2O_3 can form liquid phase to densify under low temperature driving force. Meanwhile, the wet milling procession still be observed to degradation of $Ba_5Nb_4O_{15}$ at low sintering temperature. It is one kind of de-sintering behavior by mechanochemical treatment. Though the density degradation compared to previous study is not severe so much, the de-sintering phenomena still happened at low temperature was observed from microstructure analysis.

Thermal mechanical analysis result proved the difference of densification curves between with/without additives in the sintering profile. Fig. 5-6 (a). The maximum slope over temperature curve (a) was 1180°C and curve (b) was 870°C. The mechanical milling in curve (c) to reduce densification temperature contributed around 15°C only.

doi:10.6342/NTU201702760

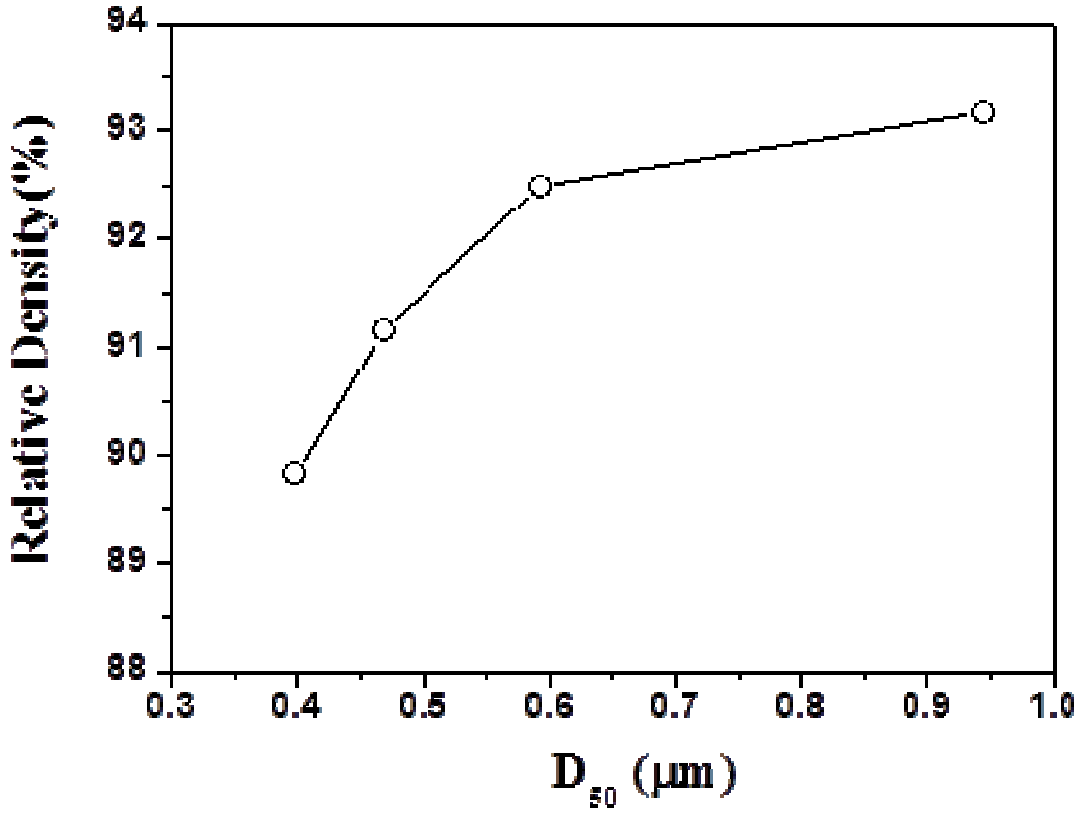

Fig. 5-2 Milling effect on the sintering density of low firing $Ba_5Nb_4O_{15}$

doi:10.6342/NTU201702760

5.3.2 Influence of milling process

As demonstrated in the previous chapter, small amounts of frits added in $Ba_5Nb_4O_{15}$ powder may interact with water during mechanical pulverization. The mechanical energy produces excess free surface of $Ba_5Nb_4O_{15}$ and induces to weaken Ba chemical bond at the cation deficient layer then dissolved into water. The precipitated $BaCO_3$ is found in powder from the reactant of barium hydroxide and carbonic acid. Fig 5-3 (a)~(c) show the morphology of milled powders which are separated by diluted slurry. Needle like precipitated substance marked B in Fig. 5-3 (c) as confirmed by EDX is $BaCO_3$. The carbon content is introduced from atmosphere. Table 5.2. XRD patterns of (1 1 1) plane for $BaCO_3$ give the evidence of increasing $BaCO_3$ content with milling time in Fig 5-4 (a).

Low firing $Ba_5Nb_4O_{15}$ material also has mechanochemical behavior by influence of milling process. The precipitated $BaCO_3$ decarbonate under 900^oC is observed by weight loss measurement. There is strongly relative property between weight loss and milling time. Fig. 5-5. A clear weight change from 540 to 680^oC is similar to Fig. 3-3 that represents the reaction of $BaCO_3$ and Nb_2O_5 at calcination process. It is decarbonation of $BaCO_3$ only.

doi:10.6342/NTU201702760

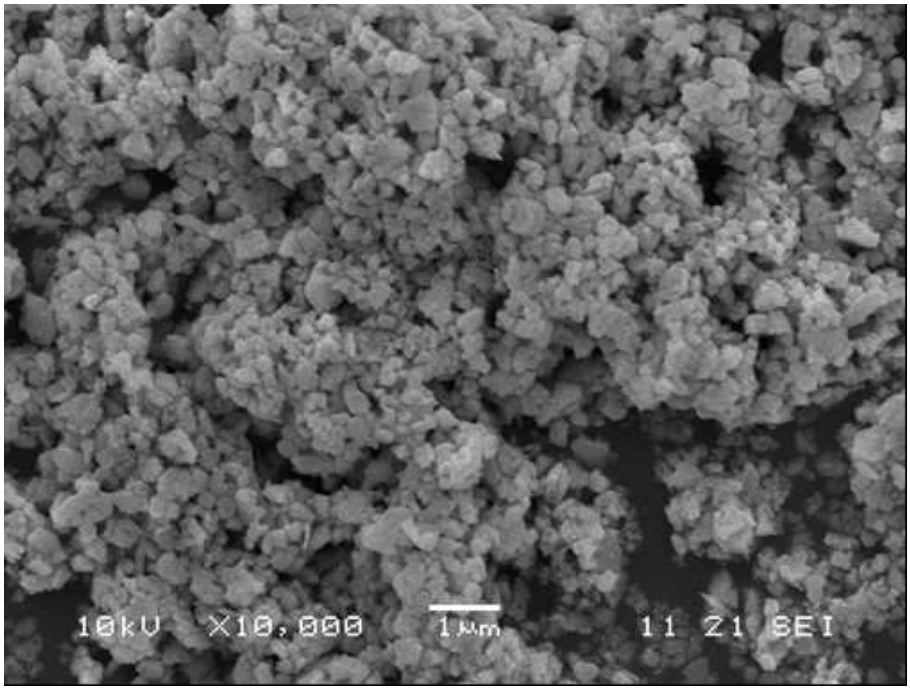

Fig. 5-3 (a) Milling 30min of Low firing $Ba_5Nb_4O_{15}$

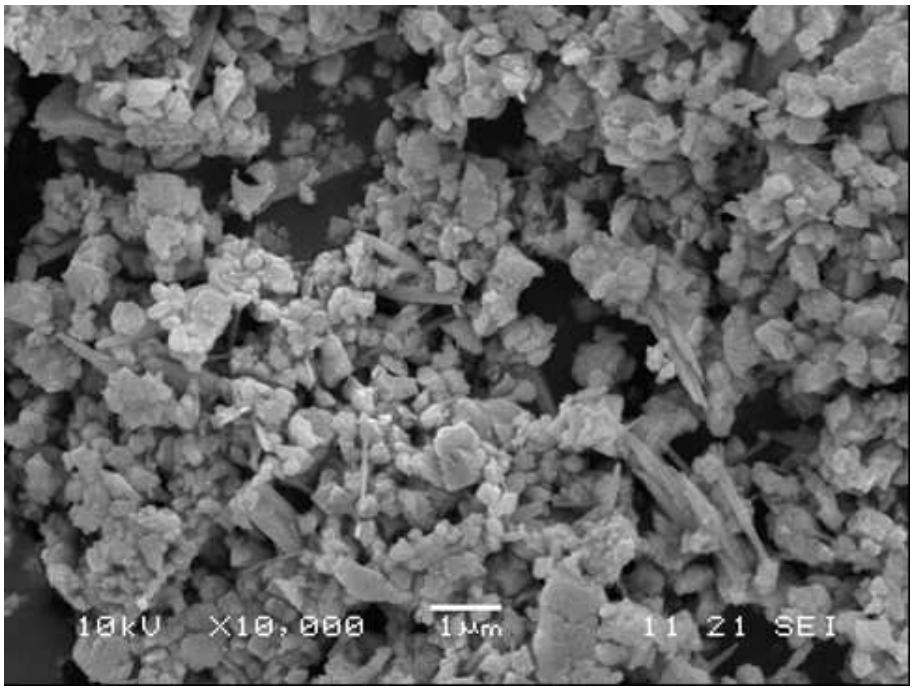

Fig. 5-3 (b) Milling 60min of Low firing $Ba_5Nb_4O_{15}$

doi:10.6342/NTU201702760

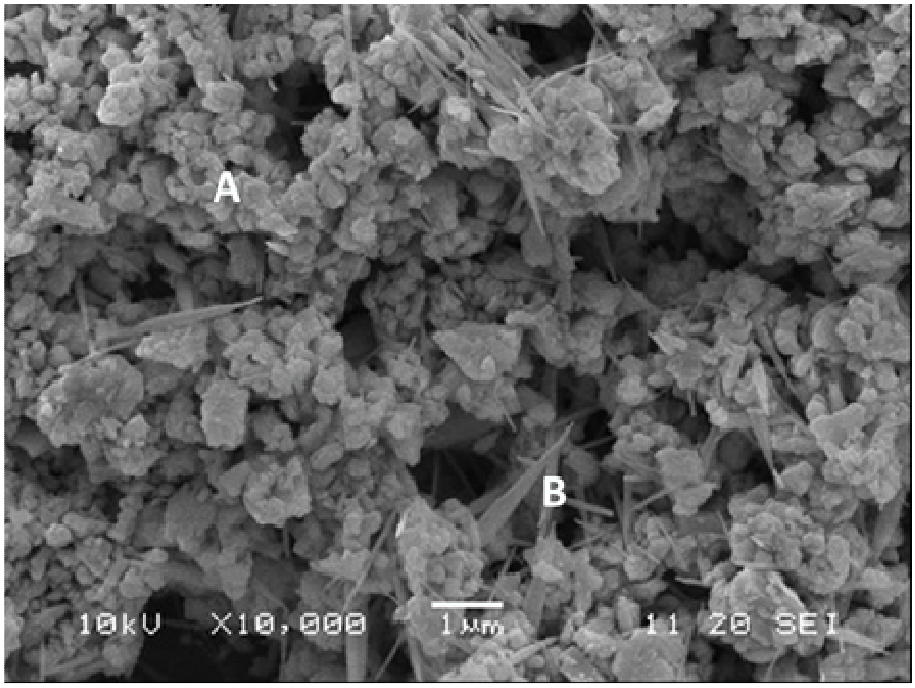

Fig. 5-3 (c) Milling 120min of Low firing $Ba_5Nb_4O_{15}$

Table 5-2 EDX Analysis of A & B Site

Element	Weight%		Atomic%	
	A	B	A	B
C K	0.0	22.3	0.0	39.0
O K	44.9	41.4	84.4	54.3
Nb L	34.0	16.1	11.0	3.6
Ba L	21.1	20.2	4.6	3.1

doi:10.6342/NTU201702760

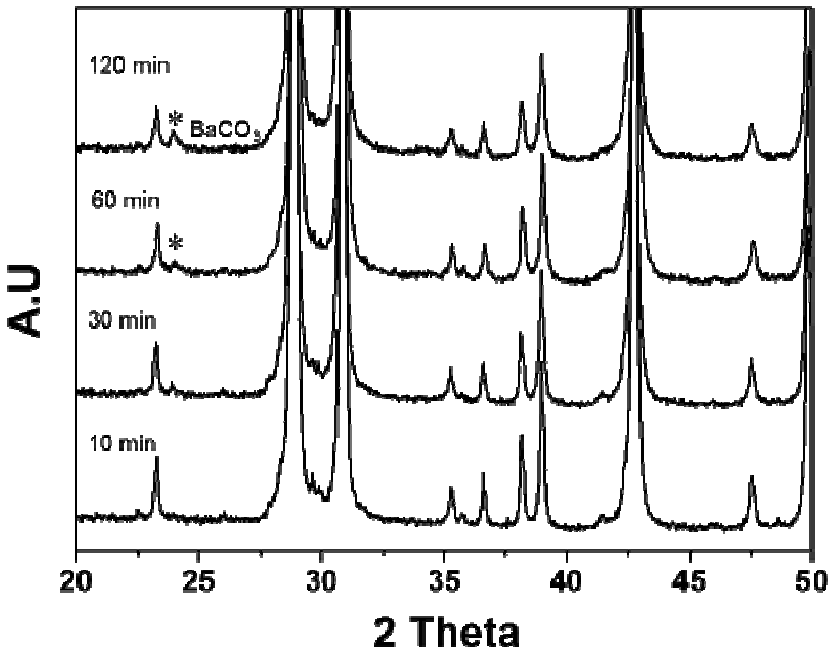

Fig. 5-4 Milling effect on $BaCO_3$ leaching of low firing $Ba_5Nb_4O_{15}$

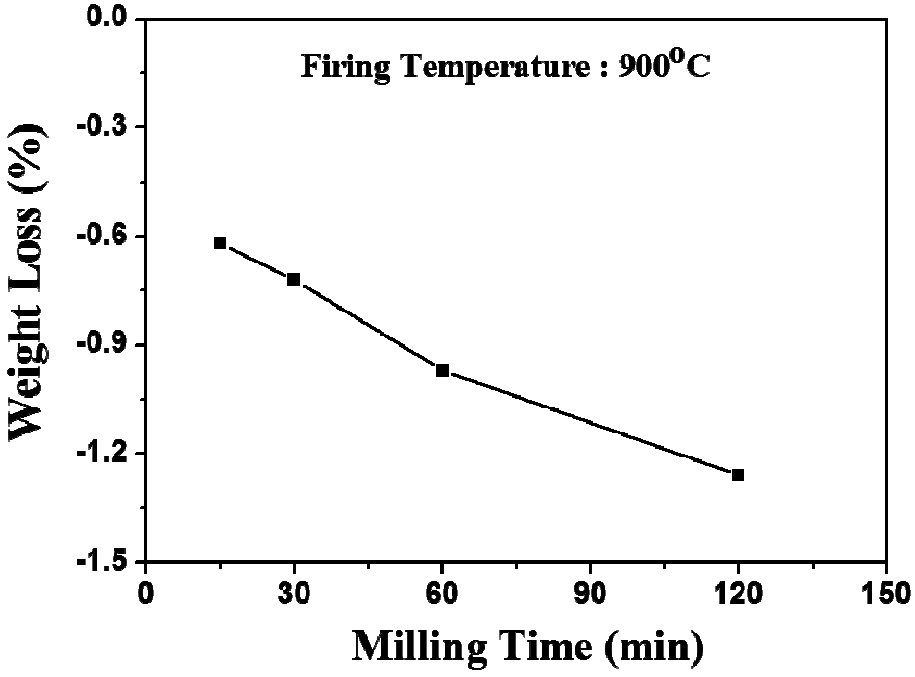

Fig. 5-5 Weight loss vs. milling time at 900°C

doi:10.6342/NTU201702760

5.3.3 Co-firing with silver metal and microstructure

The microstructure for low firing $Ba_5Nb_4O_{15}$ is different from that for high temperature sintering body. Less pores were trapped inside of sintered grain. Fig. 5-6 (a)~(d) shows inner side of sintered disc from fractured $Ba_5Nb_4O_{15}$. Longer milling time on the low firing $Ba_5Nb_4O_{15}$ powder induces the formation of non-spherical pores. It may indicate that gas evaporation from body. The microstructure in Fig. 5-6 shows connection with milling particle size, it suggests that the grains grow faster along certain orientation. It leads to elongated shapes. It may be derived from the presence of liquid phase assisting coarsening[101]. The aspect ratio of $Ba_5Nb_4O_{15}$ grain varied with milling time. More mechanical energy induces the excess free surface of $Ba_5Nb_4O_{15}$ and it induces the dissolution of Ba ion dissolved into water. The precipitated $BaCO_3$ can play a role of material transport at interface of $Ba_5Nb_4O_{15}$ powders. The shape change is belonged to reaction-controlled growth that high aspect ratio of grain exhibits a specific plane for anisotropic growth[102].

The excess $BaCO_3$ appears to induce the anisotropic grain growth at sintering temperature 900^{o}C. Figures 5-6 shows the sintered grains on the free surface vary shape under different milling time. Another appearance from fracture surface of long milling time specimens, the crack cleaves in the disc body randomly Fig. 5-6 (c) & (d). The crack may be formed by decarbonated gas of $BaCO_3$ under 900^{o}C. The CO_2 gas trapped inside of sintered body during the stage of densification. Thermal gravity analysis of milling 120 min powders gives the evidence of precipitated $BaCO_3$ decarbonation temperature. Fig. 5-7 (b). The weight loss is 1.56% at 680^{o}C. It closes to intermediate stage of low firing densification which leads to neck formation and isolated pores. The high content CO_2 gas are difficult to leave out and trapped inside of sintered body. The pressure of gas phase is going to higher when temperature increases. Finally, the trapped gas explodes into crack during the liquid phase densification stage. The decarbonation of milled $Ba_5Nb_4O_{15}$ is also caused to density

doi:10.6342/NTU201702760

degradation. It is similar to de-sintering behavior degrades the low firing $Ba_5Nb_4O_{15}$ density but not obviously.

In addition, the cross section of multilayer chip gives an evidence of acceptable co-firing temperature. The interface of dielectric and metal electrode layer is well matching without any delamination or crack to build the multilayer structure. Silver will migrate into dielectric layer under melting temperature even some ingredients enhance the reaction. The CuO / B_2O_3 additives can be used to lower $Ba_5Nb_4O_{15}$ sintering temperature and to reduce the reaction with silver metal. EPMA analysis result Fig. 5-9 shows the silver content near the interface of electrode is about zero, which means no migration. It is controversial to the copper, which well known for its diffusion easily with silver[103].

There is no mismatching crack or delamination between dielectric and metal layers, Fig. 5-8. The co-firing with different materials may involve mismatch of thermal expansion coefficients, which cause sintering strain. To measure the shrinkage curve of low firing $Ba_5Nb_4O_{15}$ and silver by dilatometer, the smaller gap between two curves is necessary. In other words, the temperature at high shrinkage rate of sintering induce the strain during densification. The heterogeneous shrinkage rate causes to mismatch at the interface. To control the silver metal powder size and morphology can modify the shrinkage curve due to the surface energy dominate the initial stage of sintering. The optimized cofiring condition for both heterogeneous materials was verified empirically.

doi:10.6342/NTU201702760

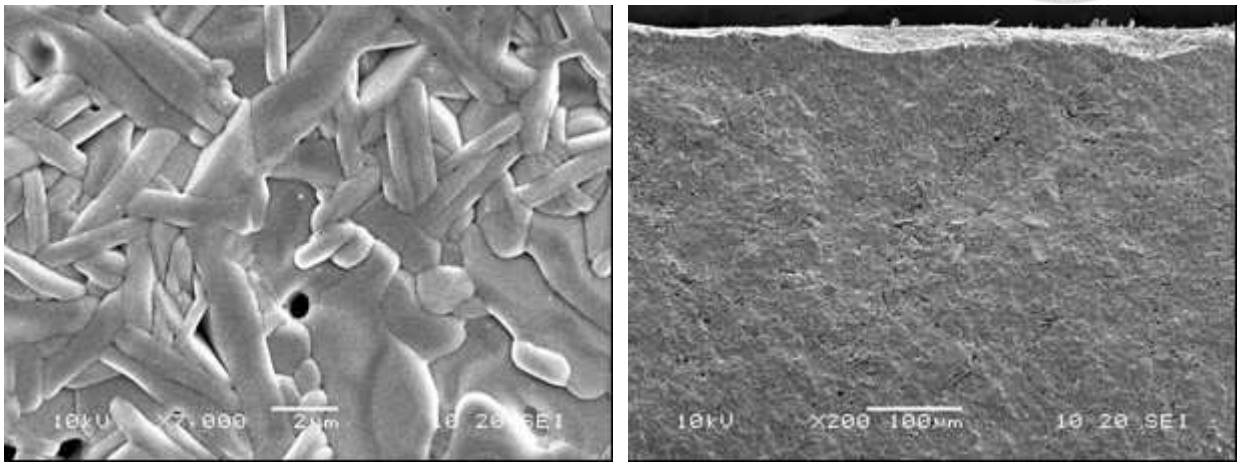

(a) (b)

Fig. 5-6 (a) 900°C sintering of $Ba_5Nb_4O_{15}$ at D_{50}=0.95um (a) free surface (b) fracture surface

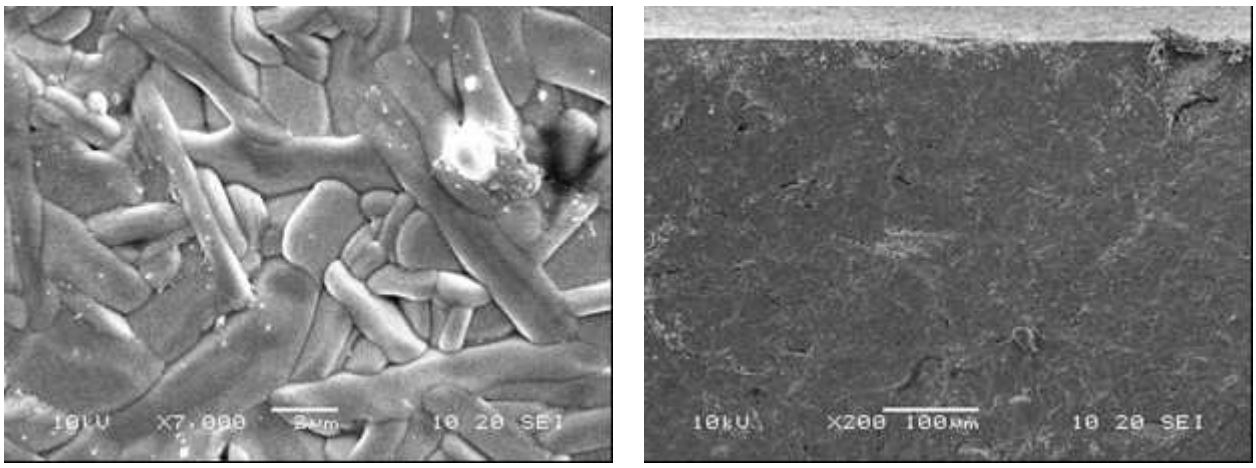

(a) (b)

Fig. 5-6 (b) 900°C sintering of $Ba_5Nb_4O_{15}$ at D_{50}=0.59um (a) free surface (b) fracture surface

doi:10.6342/NTU201702760

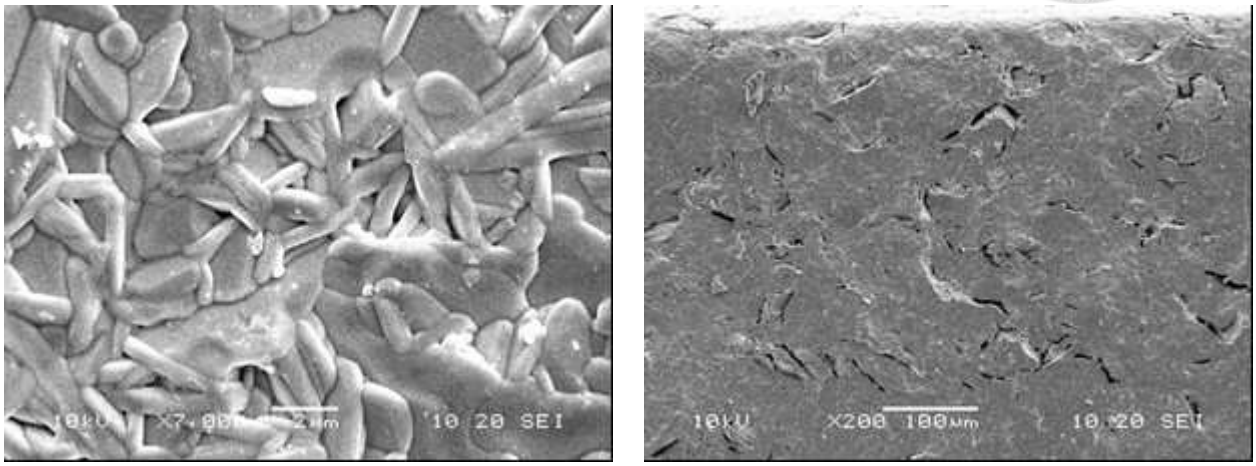

(a) (b)

Fig. 5-6 (c) 900°C sintering of $Ba_5Nb_4O_{15}$ at D_{50}=0.47um (a) free surface (b) fracture surface

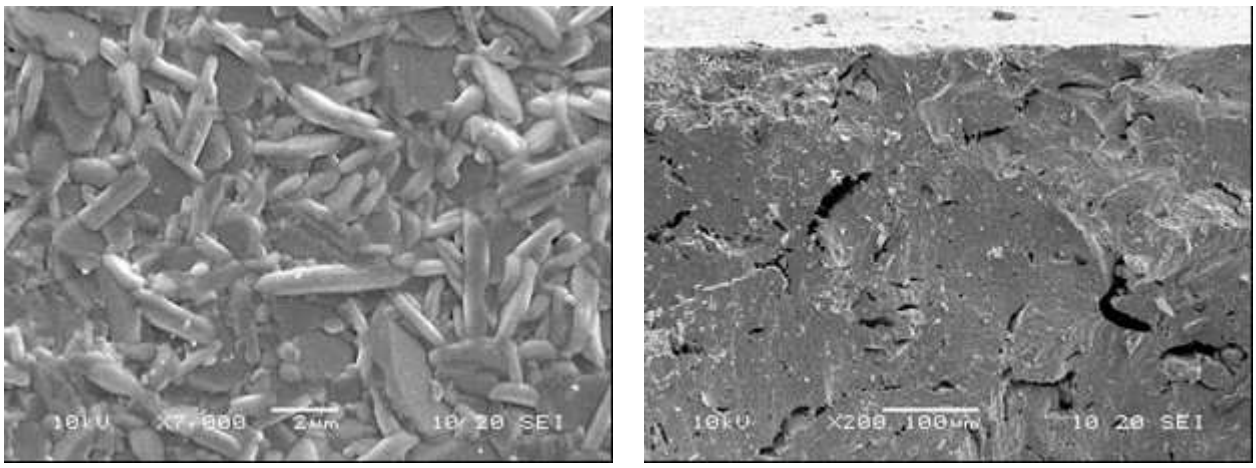

(a) (b)

Fig. 5-6 (d) 900°C sintering of $Ba_5Nb_4O_{15}$ at D_{50}=0.40um (a) free surface (b) fracture surface

doi:10.6342/NTU201702760

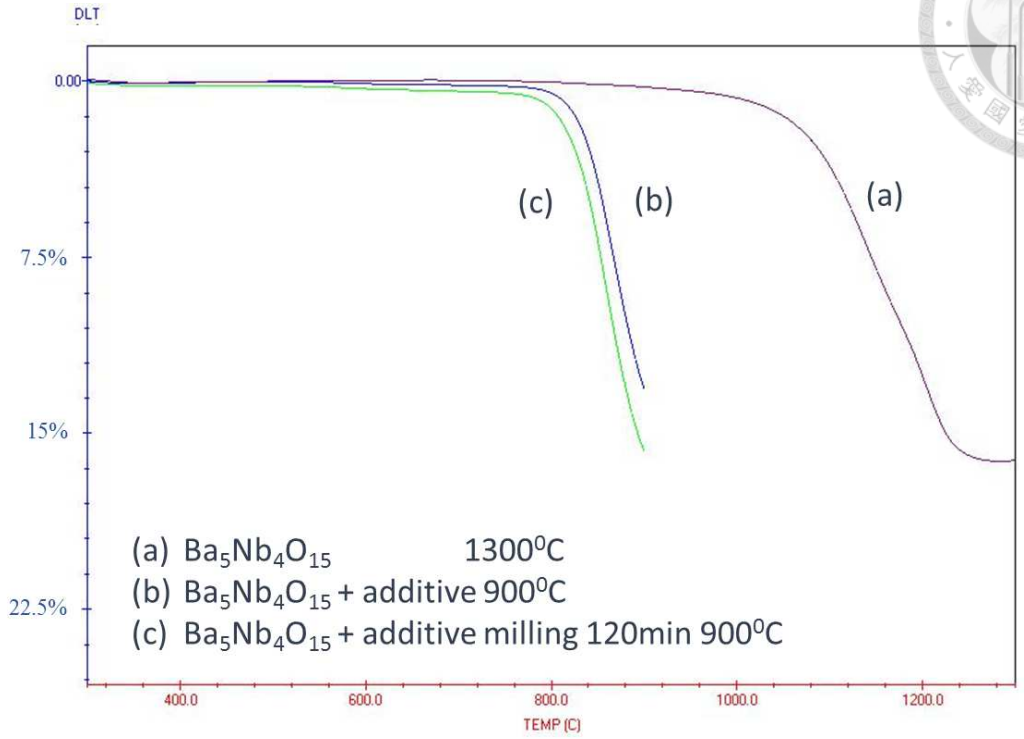

Fig. 5-7 (a) TMA experiment compare to low firing and high firing of $Ba_5Nb_4O_{15}$

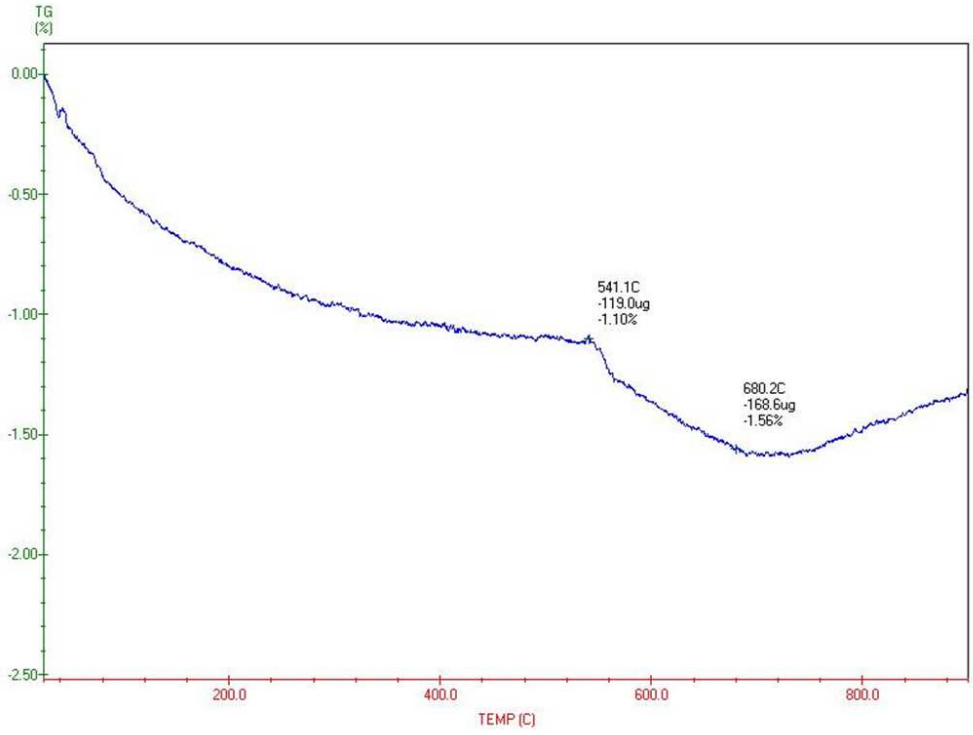

Fig. 5-7 (b) TGA experiment of milling 120 min powder

doi:10.6342/NTU201702760

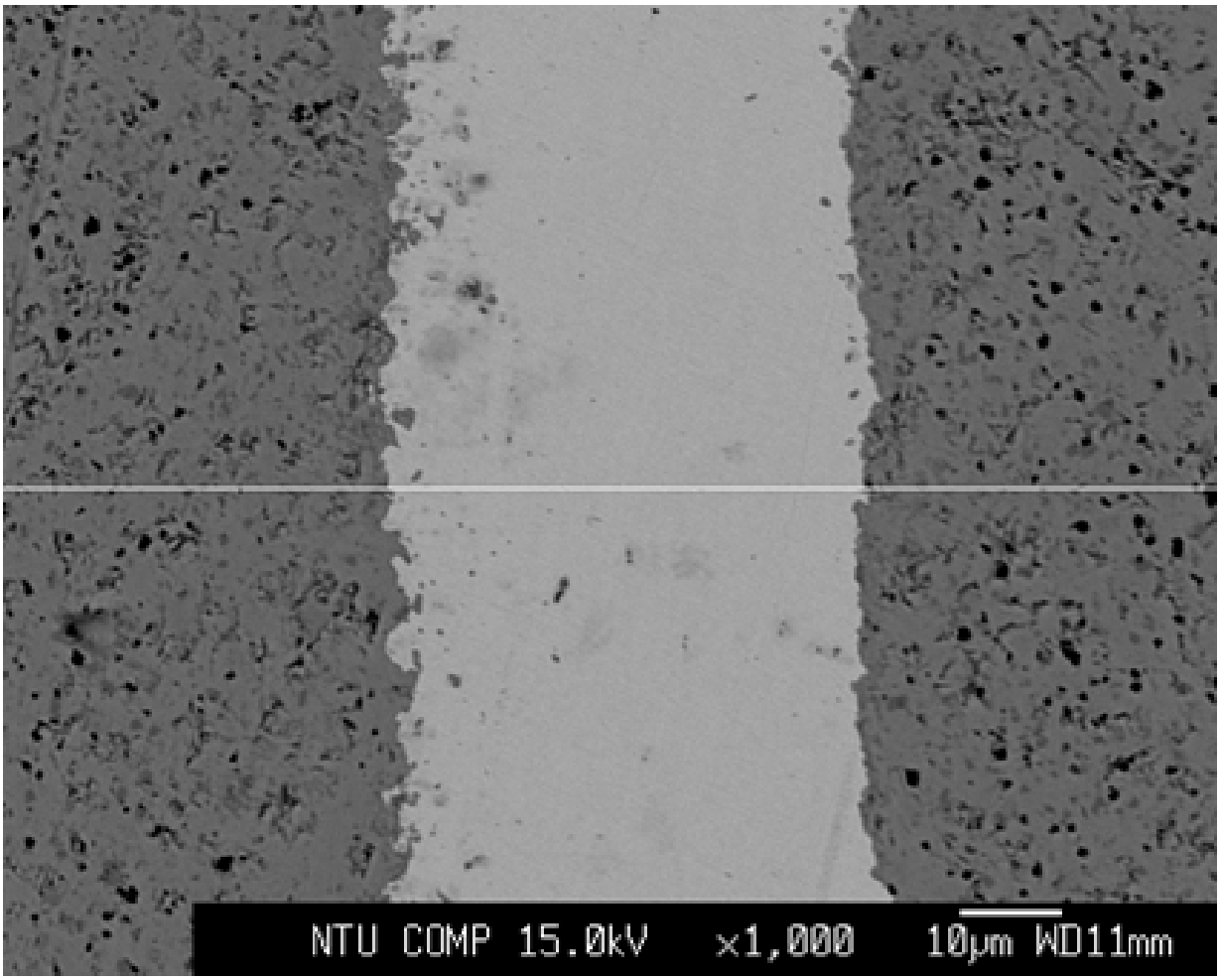

Fig. 5-8 $Ba_5Nb_4O_{15}$ and silver cofiring cross section

doi:10.6342/NTU201702760

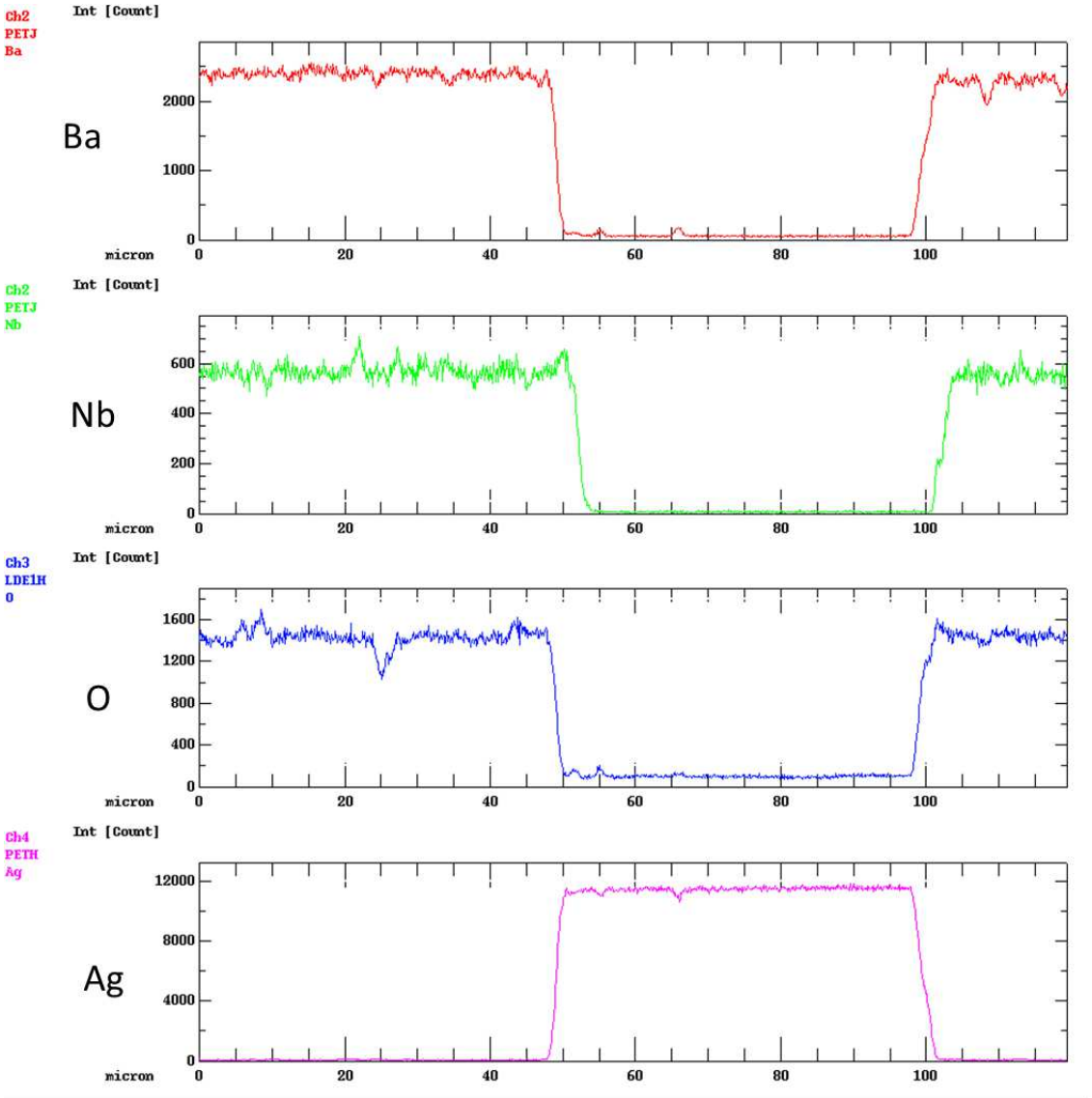

Fig. 5-9 EPMA of $Ba_5Nb_4O_{15}$ and silver cofiring cross section

doi:10.6342/NTU201702760

5.3.4 Electrical properties of low firing $Ba_5Nb_4O_{15}$

Table 5.2 shows the electrical properties of low firing $Ba_5Nb_4O_{15}$ is measured at two range of radio frequencies. This composition reveals the polarization of $Ba_5Nb_4O_{15}$ material is similar to the specimen sintered at high temperature. The permittivity is strongly related to the sintering density. When it reaches 94% relative density, the permittivity of low firing $Ba_5Nb_4O_{15}$ can approach 39. Fig. 5-10. The linear relationship between density and permittivity can be a standard rule to verify the sintering characteristics of material. Not even high firing but also low firing temperature of $Ba_5Nb_4O_{15}$ material, the permittivity can be derived from the volume ratio of porosity and ceramic mathematically.

The indication of 0.02% low dissipated factor at 1MHz proved the use of liquid phase sintering enhance densification. Generally, more open pores along grain boundary affect the space charge polarization. They are hard to be polarized if porosity is high and charges in the domain space recover like heat dissipation. In other words, the space charge polarization dominates at low frequency. High porosity of dielectric material will be high dissipated factor. Meanwhile, the effect of porosity is not distinguishable by cavity resonant method. Dipolar polarization under microwave frequency exhibits dielectric dispersion that no longer follow the oscillation of electric field. The dissipated factor or quality factor was deduced from resonated electromagnetic field energy. In this study, the Qx*f* value keeps the same level about 20,000. It seems to immune to milling process under low firing temperature.

doi:10.6342/NTU201702760

Table 5-2. Milled low sintering temperature of $Ba_5Nb_4O_{15}$

Milling time / min	Mean particle size / μm	Sintered density / g/cm^3	Permittivity K	D.F 1MHz (%)	Quality F. Qxf	
15	0.945	5.87	38.8	0.02	13,350	
30	0.593	5.83	38.4	0.02	19,980	900℃
60	0.469	5.74	37.9	0.02	20,000	4h
120	0.399	5.66	37.2	0.02	19,780	

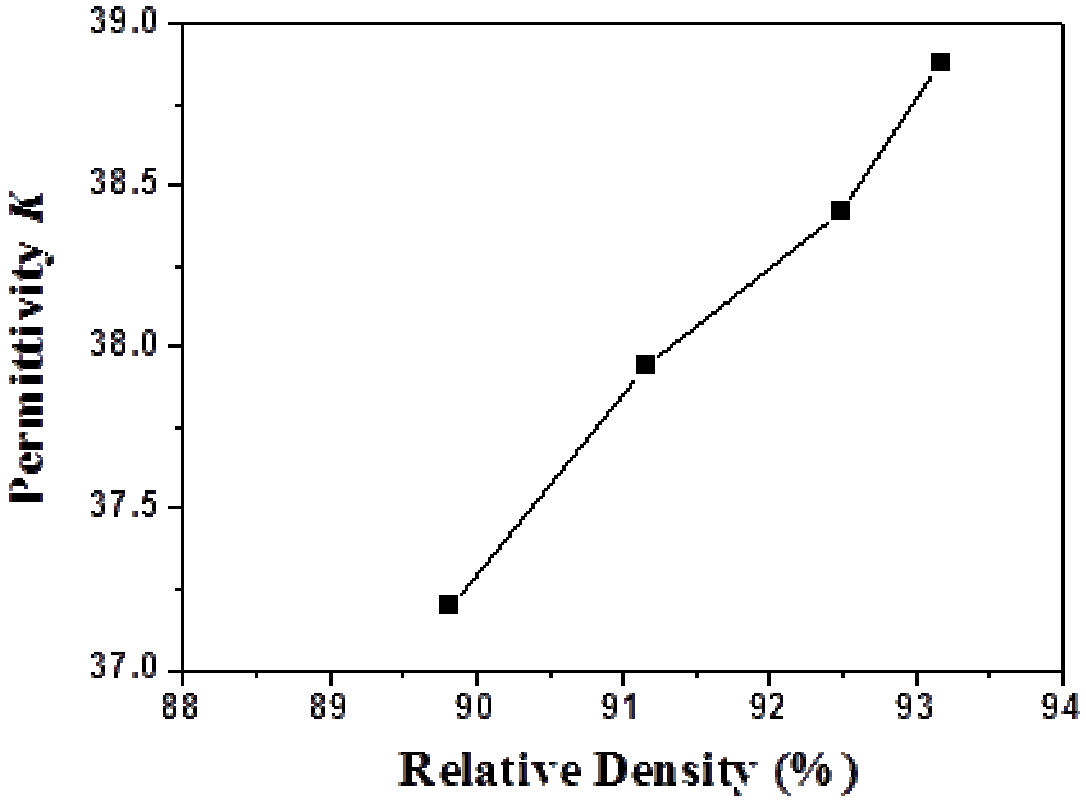

Fig. 5-10 Permittivity vs. Sintering Density of low firing $Ba_5Nb_4O_{15}$

doi:10.6342/NTU201702760

5.4 Conclusion

The anisotropic grain growth derived by chemical interaction during milling exhibits the same role on low sintering temperature. The grain grows faster along certain orientation may be derived from liquid phase. Meanwhile, the precipitated barium carbonate from intensive mechanical chemical interaction can play a role of material transport on the interfacial surface of $Ba_5Nb_4O_{15}$ powders. A slight density degradation is generated by decarbonated $BaCO_3$ under low sintering temperature. It can be overcome if choose proper sintering profile.

Excessive milling time may not bring severe drawbacks to its microwave performance. Permittivity property of low temperature sintered $Ba_5Nb_4O_{15}$ depends strongly on its density. For engineering point of view, high accuracy of permittivity is welcomed for RF component design. The milling of low firing Ba_5Nb4O_{15} is a key step to control densification. Another quality factor 20,000 reveals to the same level compared to others studies. Low sintering temperature assisted by liquid phase can reduce milling process sensitivity.

doi:10.6342/NTU201702760

Chapter 6: Conclusions

There is a limiting density for the preparation of $Ba_5Nb_4O_{15}$ specimen through the use of liquid phase sintering. Such density limit is mainly resulted from the anisotropic grain growth. Both at the high firing and low firing temperature, the density is only 93%, further increase of density is not possible. The increase in the sintering temperature results in the reduction of Nb^{+5} ions at a temperature above 1400°C, the density is further reduced. The increase of porosity and grain size reduces the permittivity of $Ba_5Nb_4O_{15}$ specimen. However, the order of cations in $Ba_5Nb_4O_{15}$ perovskite is improved with the increase of sintering temperature; the quality factor is therefore enhanced. It concludes a certain lattice plane $(0\ 1\ 13)_H$ ordering degree is the indication of higher quality factor. The quality factor of $Ba_5Nb_4O_{15}$ can be improved with the increase of soaking time also. But it is enhanced a bit.

In this study, many experiments determine the importance of mechanical treatment on microwave ceramic property. A typical mechanochemical behavior of $Ba_5Nb_4O_{15}$ can be carried out at solid state process. There is a degrading densification for preparing $Ba_5Nb_4O_{15}$ specimen through reducing particle size. The degradation mechanism mainly is resulted from the precipitate of $BaCO_3$. That is leaching of barium ions, which react with carbonic ions in water. The excess $BaCO_3$ affect the formation of preferred orientation at a sintering temperature 1435°C. At the temperature, the relative density reaches only 85% and further decrease of density when increasing the milling time. The orientated grains of sintered $Ba_5Nb_4O_{15}$ reveals the anisotropic growth at $(0\ 0\ 1)_H$ plane. Microwave properties of $Ba_5Nb_4O_{15}$ is influenced by milling process extremely. Both permittivity and quality factor descend along with increasing milling time.

It is obviously, intensive milling enhances anisotropic grain growth at low temperature sintered $Ba_5Nb_4O_{15}$. Due to the liquid phase assist densification, the relative density can reach 93%. The

doi:10.6342/NTU201702760

microwave properties are less sensitive on milling process. The decarbonated $BaCO_3$ is unavoidable during liquid phase sintering temperature. Modify the sintering profile accordance with decarbonated temperature is reasonable method to get high accuracy permittivity in application.

The full mechanism of precipitated $BaCO_3$ from $Ba_5Nb_4O_{15}$ with water environment is explained as below one. Fig. 6-1.

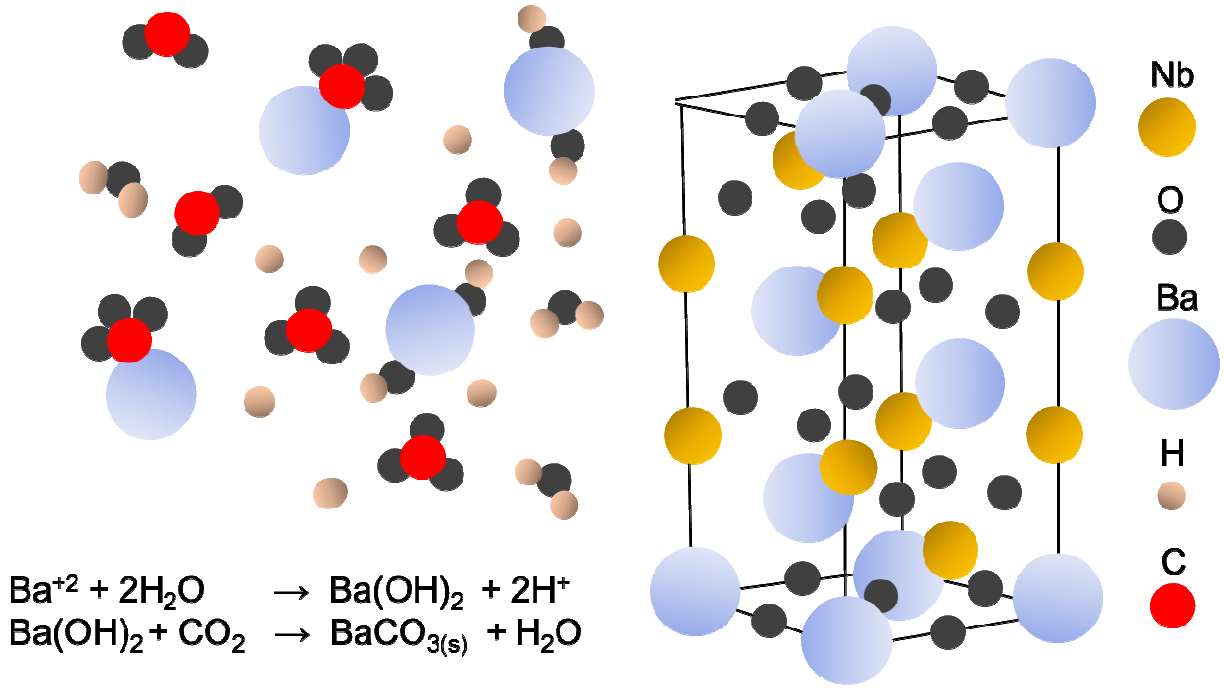

Fig 6-1 Mechanochemical mechanism of barium ion dissolving in water and $BaCO_3$ precipitation

doi:10.6342/NTU201702760

Chapter 7: Future Work

1. To obtain high quality factor is a challenging task for $Ba_5Nb_4O_{15}$ material. The future works will develop innovated process to guarantee a higher quality factor.

2. Due to mechanochemical property of $Ba_5Nb_4O_{15}$ caused by water vehicle, the attrition route without H_2O will be an interesting alternation.

3. Ordering lattice site on (0 1 13) plane has been confirmed as an indication of quality factor. How to characterize the orientation by HRTEM is interesting.

doi:10.6342/NTU201702760

Appendix

At the final stage of sintering, air may be trapped within the pores, as the case for the present study. For a spherical pore with the size of V_1, in order to achieve a balance between the pressure (P) within the pore of the surface energy (γ), the following equation can be used to estimate the size of the pores,[26]

$$P = \frac{n_1 RT}{V} = \frac{2\gamma}{r} \quad \text{(A1)}$$

In the above equation, n_1 is the number of gas atoms, r_1 the radius of the pore, R the Boltzmann constant, T the absolute temperature. Assuming the pore is a spherical one, r_1 can be expressed in the following

$$r_1 = \left(\frac{n_1 RT}{\frac{8}{3}\pi\gamma}\right)^{0.5} \quad \text{(A2)}$$

As two pores with the same volume of V_1, each with radius of r_1 and gas atoms of n_1, collapsed together to form one larger pore with the size of V_2; based on the requirement of mass conservation, the volume of r_2 can be expressed as following

$$r_1 = \left(\frac{2n_1 RT}{\frac{8}{3}\pi\gamma}\right)^{0.5} \quad \text{(A3)}$$

then,

$$V_2 = \frac{4}{3}\pi r_2^{\,3} = 2\sqrt{2}\,\frac{4}{3}\pi r_1^{\,3} = \sqrt{2}(2V_1) > 2V_1 \quad \text{(A4)}$$

The above equation suggests that V_2 is larger than $2V_1$. A density decrease is thus accompanied with the coarsening of pores.

doi:10.6342/NTU201702760

Reference:

1. K. Wakino, “Recent development of dielectric resonator materials and filters in Japan” *Ferroelectrics.*, **91**,69-86 (1989).
2. Y. Higuchi, H. Tamura, “Recent progress on the dielectric properties of dielectric resonator materials with their applications from microwave to optical frequencies” *J. Eur. Ceram. Soc*., **23** 2683-88 (2003).
3. I.M. Reaney, D. Iddles, “Microwave dielectric ceramics for resonators and filters in mobile phone networks” *J. Am. Ceram. Soc.*, **89** [7] 2063–2072 (2006).
4. A.M. Srivastava and J.F. Ackerman, “On the Luminescence of $Ba_5M_4O_{15}$ ($M=Ta^{+5}$, Nb^{+5})” *J. Solid State Chem.*, **134** [1] 187–91 (1997).
5. D.W. Kim, J.R. Kim, S.H. Yoon, K.S. Hong, “Microwave dielectric properties of low-fired $Ba_5Nb_4O_{15}$” *J. Am. Ceram. Soc.*, **85** [11] 2759-62 (2002).
6. C.Y. Tsao, W.H. Tuan, K.C. Feng, “De-sintering of $Ba_5Nb_4O_{15}$ ceramic and its influence on microwave characteristics” *J. Eur. Ceram. Soc.*, **37**,1517–1521 (2017).
7. R. J. Cava, “Dielectric materials for applications in microwave communications” *J. Mater. Chem.*, **11**, 54-62 (2001).
8. M. Weiden, A. Grauel, J. Norwig, S. Horn, F. Steglich, “Crystalline structure of the strontium niobates $Sr_4Nb_2O_9$ and $Sr_5Nb_4O_{15}$” *J. Alloys and Comp.*, **218**,13-16 (1995).
9. F. Galasso and L. Katz, “Preparation and structure of $Ba_5Ta_4O_{15}$ and related compounds” *Acta Cryst*., **14**, 647-650 (1961).
10. Z. Li, M. Yang, J.S. Park, S.H. Wei, J.J. Berry and K. Zhu, “Stabilizing perovskite structures by tuning tolerance factor: Formation of formamidinium and cesium lead iodide solid-state alloys” *Chem. Mater*., **28**, 284−292 (2016).

doi:10.6342/NTU201702760

11. S. Kamba, J. Petzelt, E. Buixaderas, D. Haubrich, P. Vane, P. Kuzˇel, I. N. Jawahar, M.T. Sebastian and P. Mohanan, “High frequency dielectric properties of $A_5B_4O_{15}$ microwave ceramics”, *J. Appl. Phys*., **89**[7] 3900-3906 (2001)
12. H. Sreemoolanadhan, J. Isaac, S. Solomon, M.T Sebastian, K.A Jose and P. Mohanan, “Dielectric properties of $Ba_5Nb_4O_{15}$ ceramics. *Phys. Stat. Sol*., **143**, K45-48 (1994).
13. D.W Kim, H.J Youn, K.S Hong, C.K Kim, “Microwave dielectric properties of (1-x)$Ba_5Nb_4O_{15}$-x$BaNb_2O_6$ mixtures” *Jpn. J. Appl. Phys.* **41**,3812-3816 (2002).
14. D.W Kim, B.K Kim, H.J Je, and J.G Park, “Degradation mechanism of dielectric loss in barium niobate under a reducing atmosphere” *J. Am. Ceram. Soc*., **89** [10] 3302–3304 (2006).
15. Richard C. Ropp, “Encyclopedia of the Alkaline Earth Compounds”, P753, 2013
16. D.W Kim, K.S Hong, C.S. Yoon, C.K Kim, “Low-temperature sintering and microwave dielectric properties of $Ba_5Nb_4O_{15}$–$B_aNb_2O_6$ mixtures for LTCC applications” *J. Eur. Ceram. Soc*., **23**, 2597–2601 (2003).
17. G.H Chen, B. Qi, “Barium niobate formation from mechanically activated $BaCO_3$-Nb_2O_5 mixtures” *J. Alloys Compd.*, **425**, 395-398 (2006).
18. C.A Kumar, D. Pamu, S. Josephine, “Impedance spectroscopy, broadband, and microwave dielectric properties of mechanically alloyed $Ba_5Nb_4O_{15}$ ceramics” *Int. J. Appl. Ceram. Technol.*, **13** [3], 554-563 (2016).
19. Suk-Joong L. Kang “Sintering: densification, grain growth, and microstructure” Elsevier Ltd. (2005) ISBN 978-0-7506-6385-4.
20. W. D. Kingery, “Densification during sintering in the presence of a liquid phase. I. Theory” *J. Appl. Phys.*, **30** [3] 301-306 (1959)
21. R.M German, P. Suri and S.J Park, “Review: liquid phase sintering” *J. Mater. Sci*., **44**, 1–39 (2009).

doi:10.6342/NTU201702760

22. J. Svoboda, H. Riedel and R. Gaebel, “A model for liquid phase sintering” *Acta mater.*, **44** [8] 3215-3226 (1996).
23. M. Kahlweit, “Ostwald ripening of precipitated” *Adv. Colloid Interface Sci*., **5**, 1-35 (1975).
24. I. M. Lifshitz and V. V. Slyozov, “The kinetics of precipitation from supersaturated solid solutions” *J. Phys. Chem. Solids*, **19** [1/2] 35-50 (1961).
25. M. Hillert, O. Hunderi, N. Ryum and T.O. Satre, “A comment on the Lifshitz-Slyozov-Wagner (L-S-W) theory of particle coarsening” *Scripta Metallurgica.*, **23**, 1979-1982 (1989).
26. H. Zhuang, Z.X Yue, F. Zhao and L.T Li, “Low-Temperature sintering and microwave dielectric properties of $Ba_5Nb_4O_{15}$–$BaWO_4$ composite ceramics for LTCC applications” *J. Am. Ceram. Soc.*, **91** [1] 1–5 (2008).
27. H. Zhou, H. Wang, M.H Zhang and H.B Yang, “Microwave dielectric properties and compatibility with silver of low-fired $Ba_5Nb_4O_{15}$ ceramics by $BaCu(B_2O_5)$ addition” *J. Mater. Res.*, **25** [9] 1793-1798 (2010).
28. C.A Kumar and D. Pamu, “Microwave dielectric properties of low temperature fired $Ba_5Nb_4O_{15}$ - $BaWO_4$ ceramics supplemented with their own nanoparticles for LTCC applications” *Int. J Appl. Ceram. Technol.*, **14**, 191–199 (2017).
29. M.M. Seabaugh, I.H. Kerscht and G.L. Messing, “Texture development by templated grain growth in liquid-phase-sintered α-Alumina” *J. Am. Ceram. Soc.*, **80** [5] 1181–88 (1997).
30. E. A. Holm, G. N. Hassold and M. A. Miodownik, “On misorientation distribution evolution during anisotropic grain growth” *Acta mater*., **49**, 2981–2991 (20010).
31. L.F Chen, V.V. Varadan, C.K. Ong and C.P Neo, "Microwave theory and techniques for materials characterization". *Microwave electronics.* Wiley. (2004) ISBN 0-470-84492-2.
32. L.Z Cao and D.M Cao, “A modified formula for microwave measurement of dielectric loss using a closed cylindrical cavity dielectric resonator” *Progress in Electromagnetics Research Letters*, **49**, 39–44 (2014).

doi:10.6342/NTU201702760

33. Y. Kobayashi and M. Katoh, “Microwave measurement of dielectric properties of low-loss materials by the dielectric rod resonator method” *IEEE Tran Microwave Theory Tech.* **MTT-33,** 586-592 (1985).
34. Y. Kobayashi and S. Tanaka, “Resonant modes of a dielectric rod resonator short-circuited at both ends by parallel conducting plates” *IEEE Tran Microwave Theory Tech.* **MTT-28**, 1077-1085 (1980).
35. B.W. Hakki and P.D. Coleman, “A dielectric resonator method of measuring inductive capacities in the millimeter range” *IRE Tran Microwave Theory Tech.*, **MTT-8**, 403-410 (1960).
36. J. Sheen, “Comparisons of microwave dielectric property measurements by transmission /reflection techniques and resonance techniques” *Meas. Sci. Technol.,* **20**, 042001-12 (2009).
37. 小林禧夫 銅張りプリント配線基板のマイクロ波／ミリ波特性と実測例，ＲＦワーヅレド No.12, 57-69.
38. JIS R1627:1996 “Testing method for dielectric properties of fine ceramics at microwave frequency”
39. IEC 61338-1-3:1999 “Waveguide type dielectric resonators - Part 1-3: General information and test conditions - Measurement method of complex relative permittivity for dielectric resonator materials at microwave frequency”
40. J. Krupka, “Frequency domain complex permittivity measurements at microwave frequencies” *Meas. Sci. Technol.* **17**, R55–R70 (2006).
41. H. Tamura, K. Konoike, Y. Sakabe and K. Wakino, “Improved high-Q dielectric resonator with complex perovskite structure” *Communication Am. Ceram. Soc.*, **67** [4] C59-61 (1984).
42. M.W. Lufaso and P.M. Woodward, “Jahn-Teller distortions, cation ordering and octahedral tilting in perovskites” *Acta Cryst*., **B60**, 10-20 (2006).
43. P.M. Woodward, “Octahedral tilting in perovskites. I. Geometrical considerations” *Acta Cryst.*,

doi:10.6342/NTU201702760

B53, 32-43 (1997).

44. P.M. Woodward, "Octahedral tilting in perovskites. II. Structure stabilizing forces" *Acta Cryst.*, **B53**, 44-46 (1997).
45. A.M. Glazer, "The Classification of tilted octahedra in perovskites" *Acta Cryst*., **B28**, 3384 -3392 (1972).
46. R. J. Cernik, M. Barwick, F. Azough and R. Freer, "A synchrotron X-ray study of structural ordering in the microwave dielectric ceramic system: Ba(Ni1/3Nb2/3)O3–Ba(Zn1/3Nb2/3)O3" *J. Appl. Cryst*., **40**, 749–755 (2007).
47. J.L. Hutchison, A.J. Jacobson, "Electron microscopy of the perovskite-related phases 4H $Ba_{0.1}Sr_{0.9}MnO_{2.96}$ 5H $Ba_5Nb_4O_{15}$ and 6H $BaFeO_{2.79}$" *J. Solid State Chem.*, **20**, 417-422 (1977).
48. G. Trolliard, N. Teneze, Ph. Boullay, M. Manier and D. Mercurio, "HRTEM study of cation-deficient perovskite-related $A_nB_{n-\delta}O_{3n}$ ($n>=4\delta$) microphases in the $Ba_5Nb_4O_{15}$–$BaTiO_3$ system" *J. Solid State Chem.*, **173**, 91-100 (2003).
49. M. Grundner, J. Halbritter, "XPS and AES studies on oxide growth and oxide coatings on niobium" *J. App. Phys.*, **51**, 397-405 (1981).
50. P.P Ma, H. Gu and X.M Chen, "Determination of 1:2 ordered domain boundaries in Ba[(Co, Zn, $Mg)_{1/3}Nb_{2/3}]O_3$ dielectric ceramics" *J. Am. Ceram. Soc.,* **99** [4] 1299-1304 (2016).
51. P.K. Davies and J.Z Tong, "Effect of ordering-Induced domain boundaries on low-loss $Ba(Zn_{1/3}Ta_{2/3})O_3$-$BaZrO_3$ perovskite microwave dielectrics" *J. Am. Ceram. Soc.*, **80** [7] 1727-1740 (1997).
52. F. Azough, R. Freer, D. Iddles, T. Shimada, B. Schafferd, "The effect of cation ordering and domain boundaries on low loss $Ba(B^{I}_{1/3}B^{II}_{2/3})O_3$ perovskite dielectrics revealed by high-angle annular dark-field scanning transmission electron microscopy (HAADF STEM)" *J. Eur. Ceram. Soc.*, **34**, 2285–2297 (2014).

doi:10.6342/NTU201702760

53. Qi. Ma, P. Ryan, J. W. Freeland and R. A. Rosenberg, “Thermal effect on the oxides on Nb (100) studied by synchrotron-radiation x-ray photoelectron spectroscopy” *J. Appl. Phys.*, **96**[12] 7675-7680 (2004).

54. B.A. Sexton, A.E. Hughes and K. Foger, “XPS investigation of strong metal-support interactions on group Illa-Va oxides” *J. Catal*., **77**, 85-93 (1982).

55. S. Kimura, “Phase equilibria in the system NbO_2-Nb_2O_5 : Phase relations at 1300 and 1400°C and related thermodynamic treatment” *J. Sol. Stat. Chem*., **6**, 438-449 (1973).

56. C.T Lee, C.C Ou, Y.C Lin, C.Y Huang, C.Y Su, “Structure and microwave dielectric property relations in $(Ba_{1-x}Sr_x)_5Nb_4O_{15}$ system” *J. Eur. Ceram. Soc*., **27**, 2273–2280 (2007).

57. Y.C Liou, W.H Shiu, C.Y Shih, “Microwave ceramics $Ba_5Nb_4O_{15}$ and $Sr_5Nb_4O_{15}$ prepared by a reaction-sintering process” *Mater. Sci. Eng*., **B131**, 142–146 (2006).

58. W.D. Kingery, H.K. Bowen, D.R. Uhlmann, “Introduction of ceramics - 2nd edition” Wiley Co., ISBN: 978-0-471-47860-7

59. S.C. Hansen and D.S. Phillips, “Grain boundary microstructures in a liquid-phase sintered alumina (α-Al_2O_3)” *Philos. Mag.*, **A47** [2] 209-234 (1983).

60. S. Stemmer, G. Roebben and O. van der Biest, “Evolution of grain boundary films in liquid phase sintered silicon nitride during high-temperature testing” *Acta mater*., **46**[15] 5599-5606 (1998).

61. W. Rheinheimer and M.J. Hoffmann, “Grain growth in perovskites: What is the impact of boundary transitions?” *Curr. Opin. Solid State Mater. Sci*., **20**, 286–298 (2016).

62. E.Z. Kurmaev, A. Moewes, O.G. Bureev, I.A. Nekrasov, V.M. Cherkashenko, M.A. Korotin, D.L. Edererd, “Electronic structure of niobium oxides” *J. Alloys and Comp.*, **347**, 213–218 (2002).

63. C. Vineis, P.K Davies, T. Negas, S. Bell, “Microwave dielectric of hexagonal perovskites” *Mater. Res. Bull.*, **131**[5] 431-37 (1996).

doi:10.6342/NTU201702760

64. I.N Jawahar, M.T Sebastian, P. Mohanan, "Microwave dielectric properties of $Ba_{5-x}Sr_xTa_4O_{15}$, $Ba_5Nb_xTa_{4-x}O_{15}$ and $Sr_5Nb_xTa_{4-x}O_{15}$ ceramics" *Mater. Sci. Eng.*, **B106**, 207–212 (2006).

65. I.T Kim, Y.H Kim, S.J Chung, "Order-disorder transition and microwave dielectric properties of $Ba(Ni_{1/3}Nb_{2/3})O_3$ ceramics" *Jpn. J. Appl. Phys*., **34**[8] 4096-4103 (1995).

66. C.T Lee, Y.C Lin and C.Y Huang, "Cation ordering and dielectric characteristics in barium zinc niobate" *J. Am. Ceram. Soc*., **90** [2] 483–489 (2007).

67. S. Kawashima, M. Nishida, I. Ueda, H. Ouchi, "$Ba(Zn_{1/3}Ta_{2/3})O_3$ ceramics with low dielectric loss at microwave frequencies" *J. Am. Ceram. Soc*., **66**[6] 421-423 (1983).

68. E. Koga, Y. Yamagishi, H. Moriwake, K. Kakimoto, H. Ohsato, "Order-disorder transition and its effect on microwave quality factor Q in $Ba(Zn_{1/3}Nb_{2/3})O_3$ system" *J. Electroceram*., **17**, 375–379 (2006).

69. R. J. Cernik, M. Barwick, F. Azough and R. Freer, "A synchrotron X-ray study of structural ordering in the microwave dielectric ceramic system: $Ba(Ni_{1/3}Nb_{2/3})O_3$–$Ba(Zn_{1/3}Nb_{2/3})O_3$" *J. Appl. Cryst.*, **40**, 749–755 (2007).

70. D. Grebennikov,O. Ovchar, A. Belous and P. Mascher, "Application of positron annihilation and Raman spectroscopies to the study of perovskite structure" *J. Appl. Phys.*, **108**, 114109 (2010).

71. G. Trolliard, N. Te´ne`ze, Ph. Boullay, and D. Mercurio, "TEM study of cation-deficient-perovskite related $A_nB_{n-1}O_{3n}$ compounds: the twin-shift option" *J. Solid State Chem.*, **177**, 1188–1196 (2004).

72. R. Freer, F. Azough, "Microstructural engineering of microwave dielectric ceramics" *J. Eur. Ceram. Soc*., **28**, 1433–1441 (2008).

73. I.N Jawahar, P. Mohanan and M.T Sebastian, "$A_5B_4O_{15}$ (A=Ba,Sr,Mg,Ca,Zn; B=Nb,Ta) microwave dielectric ceramics" *Mater. Lett.* **57**, 4043-4048 (2003).

doi:10.6342/NTU201702760

74. P. Ferrer, M. Alguer´o and A. Castro, “Influence of the mechanochemical conditions on the processing of $Bi_4SrTi_4O_{15}$ ceramics from submicronic powdered precursors” *J. Alloys and Comp.*, **464**, 252–258 (2008).

75. B. Itaalit, M. Mouyanen, J. Bernard, J.M Reboul and D. Houivet, “Improvement of microwave dielectric properties of $Ba(Co_{0.7}Zn_{0.3})_{1/3}Nb_{2/3}O_3$ ceramics prepared by solid-state reaction” *Ceram. Int.*, **41**, 1937–1942 (2015).

76. T. Wang, X.D Fang, W.W Dong, R.H Tao, Z.H Deng, D.L Li, Y.P Zhao, G. Meng, S. Zhou, X.B Zhu, “Mechanochemical effects on microstructure and transport properties of nanocrystalline $La_{0.8}Na_{0.2}MnO_3$ ceramics” *J. Alloys and Comp.*, **458**, 248–252 (2008).

77. M. Senna, T. Kinoshita, Y. Abe, H. Kishi, C. Ando, Y. Doshida, B. Stojanovic, “Smart soft-mechanochemical syntheses of well-crystallized pure phase fine particulates of mixed oxides for electroceramics” *J. Eur. Ceram. Soc.*, **27**, 4301–4306 (2007).

78. B. Psiuk, J. Szade, R. Wrzalik, M. Osadnik, T. Wala, “Milling-induced phenomena in $SrTiO_3$” *Ceram. Int.*, 40, 6957–6961 (2014).

79. S.Y Noh, M.J Yoo, S. Nahm, C.H Choi, H.M Park and H.J Lee, “Effect of structural changes on the microwave dielectric properties of $Ba(Zn_{1/3}Nb_{2/3})O_3$ ceramics” *Jpn. J. Appl. Phys.*, **41**[5] 2978–2981 (2002).

80. B.D. Stojanovic, “Mechanochemical synthesis of ceramic powders with perovskite structure” *J. Mater. Process. Technol.*, **143-144**, 78–81(2003).

81. G. Chen, J. Chen, L.J Liu, C. Srinivasakannan and J.H Peng, “Synthesis and Characterization of $BaCO_3$ nanoparticles with different morphologies by microwave homogenous precipitation” *High Temp. Mater. Proc.*, **32**[1] 47–50 (2013).

82. L.C Tien, C.C Chou and D.S Tsai, “Ordered structure and dielectric properties of lanthanum-substituted $Ba(Mg_{1/3}Ta_{2/3})O_3$” *J. Am. Ceram. Soc.*, **83**[8] 2074–2078 (2000).

doi:10.6342/NTU201702760

83. F. Lichtenberg , A. Herrnberger and K. Wiedenmann, “Synthesis, structural, magnetic and transport properties of layered perovskite-related titanates, niobates and tantalates of the type $A_nB_nO_{3n+2}$,$A'A_{k-1}B_kO_{3k+1}$ and $A_mB_{m-1}O_{3m}$” *Prog. Solid State Chem.*, **36**, 253-387 (2008).

84. M.A. Akbas and P.K. Davies, “Ordering-induced microstructures and microwave dielectric properties of the $Ba(Mg_{1/3}Nb_{2/3})O_3$–$BaZrO_3$ system” *J. Am. Ceram. Soc.*, **81**[3] 670–76 (1998).

85. L.G. Austin, “A commentary on the Kick, Bond and Rittinger laws of grinding” *Powder Technol.*, **7**, 315-317 (1973).

86. E.T. Stamboliadis, “The energy distribution theory of comminution specific surface energy, mill efficiency and distribution mode” *Miner. Eng.*, **20**, 140–145 (2007).

87. José M.F. Ferreira, S.M. Olhero, A. Kaushal, “Is the ubiquitous presence of barium carbonate responsible for the poor aqueous processing ability of barium titanate?” *J. Eur. Ceram. Soc.*, **33**, 2509-2517 (2013).

88. H. Tanaka, “Shape changes of spheroidal and rectangular grains driven by excess free energy” *J. Eur. Ceram. Soc.*, **24**, 2763-2768 (2004).

89. P. Boullay, N. Te´ne`ze, G. Trolliard, D. Mercurio and J.M. Perez-Mato, “Superspace description of the hexagonal perovskites in the system $Ba_5Nb_4O_{15}$–$BaTiO_3$ as modulated layered structures” *J. Solid State Chem.*, **174**, 209–220 (2003).

90. F. Hofmann et. al., “3D lattice distortions and defect structures in ion-implanted nano-crystals” *Scientific Reports*., 7:45993 (2017).

91. T.Lowe, F. Azough, R. Freer, “ The microstructure and microwave dielectric properties of ceramics in the system $CaTiO_3$-$Li_{0.5}Nd_{0.5}TiO_3$” *J. Kor. Ceram. Soc.*, **40**[4] 328-332 (2003).

92. E. Guilmeau, C. Henrist, T.S. Suzuki, Y. Sakka, D. Chateigne, D. Grossin and B. Ouladdiaf, “Texture of alumina by neutron diffraction and SEM-EBSD” *Mater. Sci. Forum*, **495-497**, 1395-1400 (2005).

93. W.L Tzeng, H.W Yen, W.C Lin, S.J Shih, “Grain boundary engineering for improving

doi:10.6342/NTU201702760

conductivity of polycrystalline SrTiO3" *Ceram. Int.*, **43**, 2361–2367 (2017).

94. T.V. Kolodiazhnyi, A. Petric, G.P. Johari, A.G. Belous, "Effect of preparation conditions on cation ordering and dielectric properties of $Ba(Mg_{1/3}Ta_{2/3})O_3$ ceramics" *J. Eur. Ceram. Soc.*, **22** 2013–2021 (2002).
95. M.T. Sebastian and H. Jantunen, "Low loss dielectric materials for LTCC applications: a review" *Int. Mater. Rev.*, **53**, 57-90 (2008).
96. S. Sakamoto, H. Adachi, K. Kaneko, Y. Sugimoto and T. Takada, "Novel Low Temperature co-fired ceramic material system composed of dielectrics with different dielectric constants" *Jpn. J. Appl. Phys.*, **52**, 09KH03 (2013).
97. T. Takada, S. Nakao, M. Kojima and Y. Higuchi, "Development, analysis, and application of a glass–alumina-based self-constrained sintering low-temperature cofired ceramic" *Int. J. Appl. Ceram. Technol.*, **4** [5] 398–405 (2007).
98. J.R Kim, D.W Kim, H.S Jung, K.S Hong, "Low-temperature sintering and microwave dielectric properties of Ba5Nb4O15 with ZnB2O4 glass" *J. Eur. Ceram. Soc.*, **26**, 2105–2109 (2006).
99. N. Wang, C.L Liu, Y.B Wang, J.Z Cheng, J.Z Gong, H.F Zhou., "Microwave dielectric properties and compatibility with silver electrode of novel low-fired $Ba_4CuTi_{11}O_{27}$ ceramic" *Ceram. Int.*, 42, 15855–15860 (2016).
100. R.L Jia, H. Su, X.L Tang and Y.L Jing, "Effects of $BaCu(B_2O_5)$ addition on sintering temperature and microwave dielectric properties of $Ba_5Nb_4O_{15}$–$BaWO_4$ ceramics" *Chin. Phys.*, **B23**[4] 047801 (2014).
101. H. Ravash, L. Vanherpe, J. Vleugels, N. Moelans, "Three-dimensional phase-field study of grain coarsening and grain shape accommodation in the final stage of liquid-phase sintering" *J. Eur. Ceram. Soc.*, **37**, 2265–2275 (2017).
102. A. Kazaryan, B.R. Patton, S.A. Dregia, Y. Wang "On the theory of grain growth in systems with anisotropic boundary mobility" *Acta Materialia.*, 50, 499–510 (2002).

doi:10.6342/NTU201702760

103. X. Cui ,B. Li, J.H Shen, Y.H Wang and J. Zhou, “The co-fired behaviors between Ag and glass–ceramics materials in LTCC” *J. Electroceram.*, 21, 541–544 (2008).

doi:10.6342/NTU201702760